

Universität Bayreuth

Forschungsstelle für Atmosphärische Chemie

**Experimental Studies of the Heterogeneous Kinetics of OH Radicals
with Terbutylazine, Adsorbed on Self- Synthesized SiO₂ Particles,
in a Temperature Controlled Aerosol Smog Chamber**

Dissertationsschrift von

M. Sc. Lei Han

Vorgelegt der Fakultät für Biologie, Chemie und Geowissenschaften,

Universität Bayreuth

This doctoral thesis was prepared at the Atmospheric Chemistry Research Lab at the University of Bayreuth from 11/2009 until 11/2013 and was supervised by Prof. Dr. Cornelius Zetzsch.

This is a full reprint of the dissertation submitted to obtain the academic degree of Doctor of Natural Sciences (Dr. rer. nat.) and approved by the Faculty of Biology, Chemistry and Geosciences of the University of Bayreuth.

Date of submission: 09.08.2013

Date of defence: 29.11.2013

Acting dean: Prof. Dr. Rhett Kempe

Doctoral committee:

Prof. Dr. Cornelius Zetzsch	(1 st reviewer)
Prof. Dr. Thomas Foken	(2 nd reviewer)
Prof. Dr. Andreas Held	(chairman)
Prof. Dr. Britta Planer-Friedrich	
Prof. Dr. Carlo Unverzagt	

Abstract

Atmospheric lifetimes of pesticides are limited by reactions with OH, which have been studied for a long time. Most studies were focused on the gas phase and only very few experiments on semivolatile pesticides investigated their OH reactions with aerosol-borne compounds. In this work, the reaction of gas-phase OH radicals with aerosol-borne terbuthylazine (TBA) has been investigated in the low temperature aerosol simulation chamber (LOTASC) at three temperatures. Self-synthesized, monodisperse SiO₂ particles (diameter around 160 nm) were used as carrier particles in order to avoid any influence of agglomeration. The experimental results of second order rate constants showed a lower value than previous work on Aerosil 200 particles (Palm et al., 1997). However, results from this work correspond to the Langmuir-Hinshelwood mechanism, revealing the process of a reversible adsorption of OH on particle surfaces before chemical reaction. This is the first time to apply the Langmuir-Hinshelwood mechanism on the heterogeneous reaction of gas-phase OH radicals with aerosol-borne compounds. In this work, the Langmuir-Hinshelwood expression $k_{\text{obs}}^{\text{I}} = (8.6 \pm 1.2) \times 10^{-12} C_{\text{OH}} / (1 + (9.4 \pm 1.6) \times 10^{-8} C_{\text{OH}})$ was obtained at 25 °C, where the limiting slope for $C_{\text{OH}} \rightarrow 0$ according to an Eley-Rideal mechanism leads to $k_{(\text{OH})\text{Eley-Rideal}} = (8.6 \pm 1.2) \times 10^{-12} \text{ cm}^3 \text{ s}^{-1}$ (which is similar to the current views of structure/reactivity relations for gas-phase reactions).

Chamber experiments were also performed at 6.5 °C and -10 °C. The experimental Langmuir-Hinshelwood expressions are $k_{\text{obs}}^{\text{I}} = (8.5 \pm 1.6) \times 10^{-12} C_{\text{OH}} / (1 + (1.07 \pm 0.24) \times 10^{-7} C_{\text{OH}})$ and $k_{\text{obs}}^{\text{I}} = (6.08 \pm 0.97) \times 10^{-12} C_{\text{OH}} / (1 + (1.40 \pm 0.26) \times 10^{-7} C_{\text{OH}})$, respectively. Based on the kinetic parameters, the atmospheric half-lives at different temperatures have been calculated. The results show that at 25°C and 6.5°C, the half-life of terbuthylazine is less than 2 days on plain mineral dust.

Zusammenfassung

Die atmosphärische Lebensdauer von Pestiziden wird durch ihre Reaktion mit OH-Radikalen begrenzt, die seit langem Gegenstand der Forschung ist. Die meisten Arbeiten über semivolatile Pestizide konzentrieren sich ausschließlich auf die Gasphasen-Reaktionen, und nur sehr wenige Experimente untersuchen die OH-Reaktion mit aerosolgetragenen Stoffen.

In dieser Arbeit wurde die Reaktion von OH-Radikalen in der Gasphase mit aerosolgetragendem Terbutylazin (TBA) bei drei unterschiedlichen Temperaturen in einer temperierbaren Aerosol-Smogkammer (LOTASC) untersucht. Um eine Beeinflussung durch Agglomeration zu vermeiden, wurden hierfür monodisperse SiO₂-Partikel (Durchmesser ca. 160 nm) selbst synthetisiert und als Trägersaerosol verwendet. Aus der Auswertung der Experimente ergaben sich Geschwindigkeitskonstanten zweiter Ordnung, die kleiner waren als in einer früheren Arbeit mit Aerosil-200-Partikeln (Palm et al., 1997). Ein weiteres Ergebnis dieser Arbeit war, dass die Reaktion dem Langmuir-Hinshelwood Mechanismus folgt, der eine reversible Adsorption von OH auf der Partikeloberfläche vor der chemischen Reaktion annimmt. Dies ist das erste Mal, dass der Langmuir-Hinshelwood-Mechanismus auf die heterogene Reaktion von OH-Radikalen in der Gasphase mit aerosolgetragenen Stoffen angewendet wird. Es ergibt sich für T = 25 °C eine Gleichung nach Langmuir-Hinshelwood von $k_{\text{obs}}^{\text{I}} = (8.6 \pm 1.2) \times 10^{-12} C_{\text{OH}} / (1 + (9.4 \pm 1.6) \times 10^{-8} C_{\text{OH}})$ und ein Grenzwert für $C_{\text{OH}} \Rightarrow 0$ nach dem Eley-Rideal Mechanismus von $k_{(\text{OH})\text{Eley-Rideal}} = (8.6 \pm 1.2) \times 10^{-12} \text{ cm}^3 \text{ s}^{-1}$ (vergleichbar mit aus Struktur / Reaktivitäts Beziehungen in der Gasphase abschätzbaren Werten).

Weitere Smogammer-Experimente wurden bei 6.5 °C und -10 °C durchgeführt. Die daraus resultierenden Langmuir-Hinshelwood Gleichungen waren $k_{\text{obs}}^{\text{I}} = (8.5 \pm 1.6) \times 10^{-12} C_{\text{OH}} / (1 + (1.07 \pm 0.24) \times 10^{-7} C_{\text{OH}})$, beziehungsweise $k_{\text{obs}}^{\text{I}} = (6.08 \pm 0.97) \times 10^{-12} C_{\text{OH}} / (1 + (1.40 \pm 0.26) \times 10^{-7} C_{\text{OH}})$. Basierend auf den kinetischen Parametern wurden die atmosphärischen Halbwertszeiten bei unterschiedlichen Temperaturen berechnet.

Die Berechnungen ergaben für $T = 25\text{ °C}$ und 6.5 °C eine Halbwertszeit von Terbutylazin von weniger als 2 Tagen für rein mineralische Stäube.

Acknowledgement

I would like to thank Prof. Dr. Cornelius Zetzsch for the supervision of my PhD work and for the discussions that made me look into detail about scientific questions.

I want to thank our previous technician Heinz-Ulrich Krüger (†) for his enormous technical support. Without his help this work would not come to final results. Also I want to thank Agnes Bednorz for her careful coordination in the lab.

I would like to thank Dr. Sergej Bleicher for his support for sensor installation to the LOTASC chamber and his help for data analysis advices. I want to thank Dr. Frank Siekmann for his introduction coaching at the beginning of my PhD work and thank Dr. Natalja Balzer for her kind cooperation for chamber experiment arrangements.

Thanks for the help from Dr. Evelyn Volkmann (Kommunale Wasserwerke Leipzig) for the MS analysis of the reaction products. Many thanks go to Stefan Gonser (Nino) and Paulo Alarcon for their friendly help when I met the problem of language obstacle.

I would like to thank the European Union for financing the Eurochamp 2 project.

Last but not least I would like to thank my family, they gave me great support when I did my experiments and encouraged me to finish my work.

Content

Abstract.....	I
Zusammenfassung	III
Acknowledgement	V
1. Introduction.....	1
1.1 Motivation.....	1
1.2 Pesticides in the atmosphere	3
1.2.1 Gas/particle distribution.....	3
1.2.2 Transport in the atmosphere.....	5
1.2.3 Removal processes: deposition in the atmosphere.....	5
1.2.4 Photochemical reactions	6
1.2.5 Atmospheric lifetime and long range transportation.....	13
1.2.6 Introduction of terbuthylazine	13
1.3 Research objectives	14
2. Experimental Description	17
2.1 LOW Temperature Aerosol Simulation Chamber (LOTASC).....	17
2.2 Measurement instruments connected with the chamber	19
2.2.1 Instruments	19
2.2.2 Solar simulator	21
2.2.3 Temperature and relative humidity sensor	22
2.3 Aerosol coating, generation and sampling	23
2.3.1 Synthesis of the silicon dioxide particles.....	23
2.3.2 Coating of the particles with terbuthylazine	24
2.3.3 Structure analysis of the carrier particles.....	25
2.3.4 Calculation of the coverage ratio of terbuthylazine on SiO ₂ particles	28
2.3.5 Generating aerosols in the chamber.....	30
2.3.6 Sampling of particles	31
2.4 Reagents in the experiments	32
2.4.1 Chemicals and materials	32
2.4.2 Synthesis of methyl nitrite	32
3. Kinetics of heterogeneous reactions	35
3.1 Langmuir-Hinshelwood mechanism.....	35
3.2 Eley-Rideal mechanism	39
4. Production of OH radicals in the chamber.....	41
4.1 Sources of OH radicals	41
4.2 OH radical production	44
4.3 Determination of the OH radical concentration in the chamber	45
5. Calculation of the apparent rate constant of the heterogeneous reaction of terbuthylazine with OH radicals	46
5.1 Calculation of the OH radical concentration from hydrocarbons	46
5.2 Calculation of the rate constant of terbuthylazine with OH radical.....	47
6. Analysis of the compounds in the smog chamber.....	48
6.1 Analysis of the gas phase compounds.....	48

6.1.1 Introduction of the hydrocarbons into smog chamber	48
6.1.2 Sampling and analysis of the hydrocarbons from the chamber	51
6.2 Analysis of the particle-borne compounds.....	51
6.2.1 Aerosol injection into the chamber	51
6.2.2 Characterization of aerosol mass, size distribution and residence time.....	52
6.3 Sampling and extraction of the aerosol samples.....	53
7. Results and discussion	55
7.1 Monitoring of temperature and relative humidity in the smog chamber.....	55
7.1.1 Results of the temperature and relative humidity measurement at 25 °C	56
7.1.2 Results of the temperature and relative humidity measurement at 6.5 °C and -10°C.....	59
7.2 Measurements of the concentrations of ozone and nitrogen oxides in the smog chamber	60
7.2.1 Results of NO _x and ozone measurement in the experiment at 25°C.....	61
7.2.2 Results of NO _x and ozone measurement in the experiment at 6.5 °C.....	62
7.2.3 Results of NO _x and ozone measurement in the experiment at -10 °C	63
7.3 Coating efficiency during the aerosol coating process	65
7.4 Summary of experiments in the smog chamber.....	65
7.5 Heterogeneous degradation of terbuthylazine on SiO ₂ at 25 °C.....	68
7.5.1 Calculation of the OH concentration	68
7.5.2 Calculation of the TBA concentration adsorbed on aerosol.....	70
7.5.3 Determination of the OH rate constant of terbuthylazine	72
7.5.4 Application of the Langmuir-Hinshelwood and Eley-Rideal mechanisms on the experimental data at 25°C.....	73
7.5.5 Comparison with experiments of the OH radical reaction of terbuthylazine adsorbed on Aerosil 200 particles	76
7.5.6 Result of an experiment at higher OH level.....	80
7.6 Experimental results of the heterogeneous reaction of OH radicals with terbuthylazine adsorbed on SiO ₂ particles at different temperatures.....	86
7.6.1 Experiments at 6.5°C for the reaction of OH radical with terbuthylazine on SiO ₂ particles	86
7.6.2 Comparison with previous experiments on the reaction of OH radicals with TBA adsorbed on filters at 6.5°C.....	88
7.6.3 Experiments at -10°C for the reaction of OH radical with terbuthylazine on SiO ₂ particles	91
7.7 Temperature dependence of the heterogeneous reaction on self-synthesized SiO ₂ particles....	93
7.8 Product analysis	96
7.9 Possible reaction pathway analysis.....	100
7.10 Atmospheric implications	101
8. Conclusions.....	103
References	105
Appendix 1	115
Appendix 2	119

1. Introduction

1.1 Motivation

The atmospheric degradation of pesticides plays an important role in the environmental fate. Their behavior in the atmosphere could be evaluated based on the kinetic data from the reactions of pesticides with oxidants in the atmosphere, such as photolysis, heterogeneous reaction with OH radical, ozone, NO_x and other oxidants (Finlayson-Pitts and Pitts Jr., 2000). However, most of the research has been focused on the homogeneous gas-phase reactions (Atkinson et al., 1999). Considering the low volatility of the majority of the pesticides (Bidleman, 1999), the heterogeneous chemical reactions which contribute to the atmospheric degradation pathways (reactions with OH, NO₃ radicals and ozone, or photolysis) of semi-volatile organic compounds (SVOCs) (normally adsorbed on particle surfaces) should attract more attention since such studies are rare. This leads to the result that currently most of the atmospheric lifetimes of pesticides are calculated from the gaseous-phase chemical reactivity using structure–reactivity relationships (known as SAR, now the U. S. Environmental Protection Agency provides similar estimation software as EPIWIN). This methodology has been established for oxygenated compounds and volatile hydrocarbons (Kwok and Atkinson, 1995). However, due to the lack of consideration of heterogeneous reactions in the atmosphere, the lifetimes which were derived by such calculation seemed to be different from the actual measurement results.

During the 1980s, the smog-chamber technique has been developed to study the aerosol-borne reaction of SVOCs in the atmosphere. Jeffries et al. (1976) constructed an outdoor chamber at the University of North Carolina for atmospheric chemistry study; Behnke et al. (1986, 1997) built up an indoor glass chamber at Hannover for homogeneous and heterogeneous studies; at the University of California at Riverside (UCR), a “UCR-EPA” chamber has been constructed to address emphasis mainly on

mechanism evaluation of atmospheric chemistry (<http://www.engr.ucr.edu/~carter/epacham/>); until recently, more attention has been paid to the simulation experiments in the atmospheric chemistry and more chambers has been built all around Europe (<http://www.eurochamp.org/chambers/>). Besides, there are other photochemical techniques, such as rotating bulb/drum (Yang et al., 2010, Pflieger et al., 2011), and flow reactor (Cox et al., 2005), which have been developed to understand how the chemical kinetics takes place in the real atmosphere. Those results are crucial for overall atmospheric evaluation of SVOCs.

Following previous work which was conducted on the heterogeneous reactivity of OH radicals with aerosol-borne terbuthylazine (Palm et al., 1997), this work set out to explore how different characteristics of carrier particles impact their reaction kinetics during the experiments in the aerosol simulation chamber. The preliminary results suggested that the surface characteristics of SiO₂ particles could have an impact to the heterogeneous reactions of aerosol-borne terbuthylazine with OH radicals. The reaction happened with a faster rate on porous SiO₂ particle agglomerates, in comparison to non-porous SiO₂ spheres. Within a certain concentration range of OH radicals, the heterogeneous rate constant decreased slightly when the OH concentration increased. In this case, the Langmuir-Hinshelwood and Eley-Rideal mechanisms are used to explain the relations between the concentration of OH radicals and the reaction rate constant. Those mechanisms could also explain the discrepancy of recent results from Pflieger et al. (2013) with previous work (Palm et al., 1997, Palm et al., 1998).

In this research effort the author has striven to work with chamber experiments to study the atmospheric heterogeneous reaction of gas phase OH radicals with aerosol-borne terbuthylazine. Since the LOW Temperature Aerosol Simulation Chamber (LOTASC) is temperature controlled (from 25 °C down to -25 °C), experiments were performed at different temperatures and the temperature dependence of the chemical kinetics is obtained.

1.2 Pesticides in the atmosphere

Application of pesticides was considered to be beneficial alone until the late 1960s and early 1970s, when DDT residues were detected in the polar region (Sladen et al., 1966, Tatton and Ruzicka, 1967, Peterle, 1969, Bowes and Jonkel, 1975). Even in remote areas like Mt. Everest, the existence of organochlorine pesticides has been recognized (Li et al., 2006). As the pesticides can not be distributed so far away through the food chain, or attributed to surface water movement, the effect of atmospheric deposition is regarded as a dominant source in remote areas.

Pesticides are released into the atmosphere through many processes such as an application drift during spraying (Payne and Thompson, 1992, van den Berg et al., 1999), post-application volatilization and wind erosion of soil (Glotfelty et al., 1989, Nash and Gish, 1989, Klöppel and Kördel, 1997, Cherif and Wortham, 1997). For a proper evaluation of the final fate of pesticide in the atmosphere, it is important to understand the physical chemical characteristics of chosen compounds.

1.2.1 Gas/particle distribution

Many pesticides have vapour pressures (p) roughly between 10^{-4} and 10^{-11} atm at ambient temperatures and are therefore defined as semi-volatile organic compounds (SVOCs). Pesticides with higher volatility could be found in the atmospheric gas phase, while others which have low vapour pressures ($p < 10^{-4}$ Pa at 20°C) will be adsorbed on atmospheric aerosol particles (Bossan et al., 1995). Most of the pesticides will be distributed between the gas phase and the particulate phase (Bidleman, 1988). The distribution equilibrium between gas and particles is defined by the following equation:

$$K_p = (F / TSP) / A \quad 1.1$$

Here K_p ($\text{m}^3 \mu\text{g}^{-1}$) is the gas/particle partitioning coefficient, F (ng m^{-3}) and A (ng m^{-3}) are the mass concentrations of the SVOCs in gas phase and particulate phase, respectively, and TSP ($\mu\text{g m}^{-3}$) is the total concentration of suspended particles

(Finlayson-Pitts and Pitts Jr., 2000).

The distribution of pesticides between gas phase and particulate phases can be estimated by the well-known Junge-Pankow equation (Junge, 1977, Pankow, 1987). The partitioning in the equation is a function of the available aerosol surface and liquid-phase vapour pressure of the pesticide. Although it started with the BET (Brunauer, Emmett and Teller) isotherm, Pankow (1987) showed that the methodology of Junge (1977) finally followed a linear Langmuir isotherm. The theoretical Junge-Pankow model considered that the partitioning equilibrium between the gaseous phase and the suspended particles was reached rapidly in the atmosphere. The empirical Langmuir isotherm model was developed by Yamasaki et al. (1982). The gas/particle distribution is consistent with Langmuir adsorption of the SVOCs on the surface of the particles.

In the real measurements, the relative humidity (RH) is a more realistic parameter which could have an impact to the gas/particle partitioning. However, the models are unable to take into account the relative humidity (RH) in the calculation. Some studies have suggested it to be influential in the gas/particle distribution of atmospheric organic pollutants (Pankow et al., 1993, Sanusi et al., 1999, Sauret et al., 2008). The function of relative humidity is not yet clear. Pankow et al. (1993) reported a negative correlation of the gas/particle partition coefficient with increased relative humidity, while Sanusi et al. (1999) observed an increase of polar pesticides in the gas phase with enhanced RH. One possible explanation is the competition for adsorption sites on particles of polar water molecules and polar pesticides, which are in favour of water when the humidity increases, however, more research is needed to evaluate the detailed mechanism. On the other hand, models, as well as measurements, can not represent the true value of the gas/particle partitioning coefficient. Artifacts always exist during filter sampling (Sanusi et al., 1999, van Pul et al., 1999) and deviation occurs frequently between the modeling result and the measured values (Bidleman and Harner, 2000). Furthermore, very little information is available on the characteristics and size distributions of particles loaded with pesticides. There is an

assumption that the compounds are adsorbed mainly on small aerosols because of the large available aerosol surface (van Pul et al., 1999).

1.2.2 Transport in the atmosphere

After entering the atmosphere, pesticides are dispersed by air turbulence and transported by the wind flow. Pesticides can be carried to remote regions by air movement in a relatively short time. It has been regarded that the atmospheric transport of pesticides is the most important way of contamination of non-target remote areas (Guicherit et al., 1999). There have been numerous reports about the evidence of long-range transport of persistence organic pollutants (POPs) (Hargrave et al., 1988, Norstrom et al., 1988, Gregor and Gummer, 1989, Iwata et al., 1993, Oehme et al., 1996, Wania and Mackay, 1996, Harner et al., 1999, Hung et al., 2005, Li et al., 2006).

In addition to organochlorine compounds as traditional POPs, a number of modern pesticides (e.g. acetanilides, alachlor, carbofuran, dicofol, diuron, malathion, metolachlor, phosalone, trifluralin) have been found to be able to be transported to remote areas (Welch et al., 1991, Chernyak et al., 1996, Boyd-Boland et al., 1996, Rice and Chernyak, 1997, Majewski et al., 1998, Sanusi et al., 2000, Hoferkamp et al., 2010). Pesticides which are considered to be of low persistence in temperate climate are apt to be much more resistant to breakdown in cold regions. Those currently used pesticides were considered to be less persistent than before. However, their environmental behavior needs further evaluation.

1.2.3 Removal processes: deposition in the atmosphere

The residence time of a pesticide in the atmosphere depends on how rapidly the removal process takes place. Neglecting the exchange with the free troposphere, the removal process can be classified into two categories: one is the atmospheric deposition, which involves the wet deposition and the dry deposition (Bidleman, 1988); the other is the photochemical reactions, which play an important role to evaluate the atmospheric lifetime of pesticides.

Wet deposition

In wet deposition, the pesticides are scavenged by atmospheric hydrometeors (rain drops or snow). Wet deposition consists of deposition by washout and in-cloud scavenging processes. Washout is a process by which atmospheric contaminants collide with rain droplets or snow flakes and are then removed from the atmosphere. During the in-cloud scavenging, the cloud droplets accommodate the contaminants within the cloud, and afterwards those organic contaminants leave the atmosphere as the droplets fall to the ground.

Dry deposition

Dry deposition associated with particles includes gravitational sedimentation and diffusion onto water surface, or land and vegetated surfaces, or turbulent transfer in which collision happens with the droplets. It is strongly influenced by the size of particles, and most of the sorbed pesticides may be condensed on smaller particles due to their higher surface area-to-volume ratio (Bidleman and Christensen, 1979).

1.2.4 Photochemical reactions

The photochemical reactions have been regarded as an important pathway for pesticides to be removed from the atmosphere. Considering the low vapour pressure of pesticides and the corresponding distribution between gas and particles, studies about the photochemical reactions are focused on two aspects: reactions in the gas phase and reactions in the particle phase.

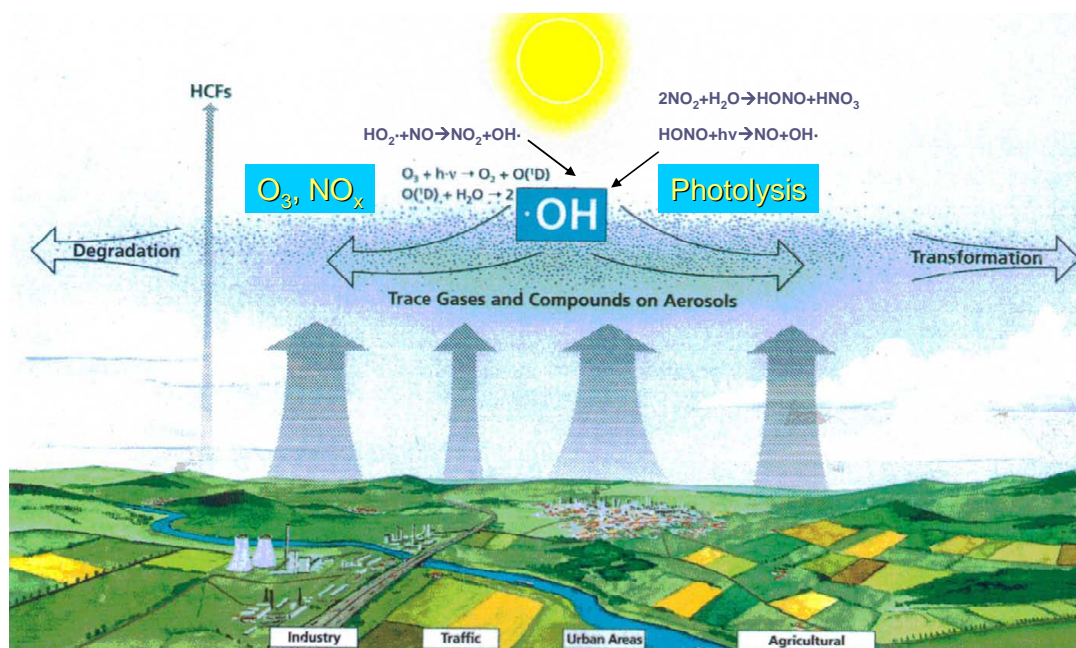


Figure 1.1 Source and degradation pathways of pesticides in the atmosphere (courtesy from Wolf-Ulrich Palm)

Gas-phase reactions

Reactions in the gas phase involve photolysis and reaction with reactive species, such as OH radicals, NO₃ radicals and O₃. Reaction with OH radicals and photolysis by direct irradiation are the major pathways of degradation for pesticides in the atmosphere (Atkinson, 1995). The nitrate radical photolyses rapidly, thus has less contribution to the daytime photochemistry (Atkinson et al., 1997a). Although reactions with ozone are also potential reaction pathways, the reaction rate is quite slow (Atkinson et al., 1999), showing less significance in the degradation process. Only until recent years, techniques for in-situ measurements (e.g. laser-induced fluorescence, high performance liquid chromatography (HPLC), chemical-ionization mass spectrometer (CIMS)) have become available, and more studies have focused on the heterogeneous ozonolysis process (Mmereki et al., 2004, Kwamena et al., 2004 and 2006, Perraudin et al., 2006, Vlasenko et al., 2008, Miet et al., 2009, Pflieger et al., 2011).

Photolysis is important only for compounds which absorb light above 290 nm (Palm et al., 1998). Many kinds of pesticides do not have chromophores to absorb light

above this wavelength, like triazines and many halogenated pesticides. Thus, the degradation process of these compounds is supposed to proceed mainly through the reaction with OH radicals (Atkinson, 1989, de Leeuw, 1993, Palm et al., 1998).

In the past few decades, a number of studies have been carried out on the degradation of pesticides during their atmospheric fate in the gas phase. Table 1.1 shows the published data for reactions of gas-phase pesticides in the atmosphere. Most of the measurements were using established absolute rate or relative rate techniques. Some pesticides have such low vapour pressure, that the measurements have to be performed at elevated temperature. The results were then extrapolated to room temperature.

Table 1.1 Published data on atmospheric reaction rate of gas-phase pesticides and selected SVOCs (reaction rate constants are in units of $\text{cm}^3 \text{molecule}^{-1} \text{s}^{-1}$ at room temperature)

Organic	k_{OH}	k_{O_3}	k_{NO_3}	$k_{\text{photo}} \text{ (s}^{-1}\text{)}$	Reference
Parathion				$\sim 6 \times 10^{-3}$	a
Trifluralin	$(1.7 \pm 0.4) \times 10^{-11}$			$\sim 6 \times 10^{-4}$	a
				$\sim 3 \times 10^{-4}$	e
				$(1.2 \pm 0.5) \times 10^{-3}$	q
Phosphine	1.5×10^{-11}				b
Biphenyl	$(8.5 \pm 0.8) \times 10^{-12}$				c
2-Chlorobiphenyl	$(2.9 \pm 0.4) \times 10^{-12}$				c
3-Chlorobiphenyl	$(5.4 \pm 0.8) \times 10^{-12}$				c
4-Chlorobiphenyl	$(3.9 \pm 0.7) \times 10^{-12}$				c
1,2-Dibromo-3-chloropropane	4.3×10^{-13}	3×10^{-20}			d
Trimethyl phosphate	7.4×10^{-12}				d
cis-1,3-Dichloropropane	8.4×10^{-12}	1.5×10^{-19}			d, f
trans-1,3-Dichloropropane	1.4×10^{-11}	6.7×10^{-19}			d, f
EPTC	3.18×10^{-11}	$< 1.3 \times 10^{-19}$	9.2×10^{-15}		g
Cycloate	3.54×10^{-11}	$< 3.0 \times 10^{-19}$	3.29×10^{-14}		g

MDTC	1.33×10^{-11}	$<4 \times 10^{-20}$	7.3×10^{-15}		g
Methyl isothiocyanate				$(6.7 \pm 1.7) \times 10^{-6}$	h
4,4'-PCB	2.0×10^{-12}				i
1-Chlorodibenzo-p-dioxin	4.7×10^{-12}				j
1,2-Dimethoxybenzene	3.5×10^{-11}				j
2,2'-PCB	2.0×10^{-12}				j
3,3'-PCB	4.1×10^{-12}				j
3,5-PCB	4.2×10^{-12}				j
Methyl bromide	2.9×10^{-14}				k
Chloropicrin				$(10.5 \pm 0.3) \times 10^{-6}$	l
Hexachlorobenzene	2.7×10^{-14}				m
α -HCH	1.4×10^{-13}				m
γ -HCH	1.9×10^{-13}				m
Phorate				$\sim 2 \times 10^{-3}$	n
Carbaryl	$(2.0 \pm 0.4) \times 10^{-11}$				o
	$(3.3 \pm 0.5) \times 10^{-11}$				o
Chlordimeform	$(3.0 \pm 0.7) \times 10^{-10}$				o
2,4-D butyl ester	$(1.5 \pm 0.2) \times 10^{-11}$				o
Dichlorvos	$(2.6 \pm 0.3) \times 10^{-11}$			$<5 \times 10^{-6}$	p

- a. (Woodrow et al., 1978)-derived from field measurement
- b. (Fritz et al., 1982)-lab measurement
- c. (Atkinson and Aschmann, 1985)-lab measurement, and extrapolation data
- d. (Tuazon et al., 1986)
- e. (Mongar and Miller, 1988)-photolysis rate In outdoor chamber
- f. (Tuazon et al., 1988)-laboratory measurement in chamber
- g. (Kwok et al., 1992)-lab measurement
- h. (Alvarez and Moore, 1994)-lab measurement
- i. (Anderson and Hites, 1995)-lab measurement, and extrapolation result
- j. (Kwok et al., 1995)-lab measurement
- k. (Atkinson et al., 1997b)
- l. (Carter et al., 1997)-lab measurement, and for overhead sun
- m. (Brubaker and Hites, 1998)-lab measurement, and extrapolation result
- n. (Hebert et al., 1998)-photolysis rate In outdoor chamber
- o. (Sun et al., 2005)-lab measurement
- p. (Feigenbrugel et al., 2006)-measurement in outdoor chamber
- q. (Le Person et al., 2007)-outdoor chamber

Particulate phase reactions

In the particle/aerosol phase, direct photolysis and reactions with O₃ and OH or NO₃ radicals are the main chemical transformation pathways of pesticides, which have been adsorbed on the surface of particles. Due to the complexity of heterogeneous gas-surface reactions, these studies have received much less attention, in comparison to the gas phase reactions.

The photocatalytic degradation of pesticides may occur on certain semiconducting metal oxides (TiO₂, ZnO, or Fe₂O₃). Behnke et al. (1987b) performed chamber experiments with di-(2-ethylhexyl)-phthalate (DEHP) on Al₂O₃, TiO₂ and Fe₂O₃ aerosols and on fly ash from a coal-fired power plant, where the results for the reaction of OH with aerosol-borne DEHP on Al₂O₃ and Fe₂O₃ showed no significant difference compared with the results on SiO₂ aerosols. On the other hand, TiO₂ showed a marked photocatalytic effect, releasing huge amounts of OH radicals to the gas phase and shortening the lifetime of DEHP to less than 30 min. Fe₂O₃ showed only a minor photocatalytic effect on the degradation of the aerosol-borne DEHP, approximately doubling the decay rate in the absence of OH. This minor photocatalytic effect of Fe₂O₃ could be suppressed by a UV cutoff filter for $\lambda < 360$ nm, but the OH-reactivity of the aerosol-borne DEHP remained unchanged. On the other hand, the reaction of OH with DEHP on fly-ash aerosol was found to be significantly lower though enhanced in the absence of OH. Since in most cases the reactions were investigated in aqueous environment alone (Borello et al., 1989, Mills and Hoffmann, 1993, Herrmann et al., 1999, Guo et al., 2001, Marinas et al., 2001, Quan et al., 2003, Anandan et al., 2007), more investigations are needed to understand the detailed photocatalytic mechanism.

Table 1.2 Summary of published data on OH radical reaction rate of pesticides in the particulate phase (reaction rate constant are in units of $\text{cm}^3 \text{molecule}^{-1} \text{s}^{-1}$, at room temperature)

Compound	Carrier Particles	k_{OH}	k_{O_3}	Reference
DEHP	SiO ₂	$(1.36 \pm 0.2) \times 10^{-11}$	$< 10^{-18}$	(Behnke et al., 1987b)
	Al ₂ O ₃	$(1.4 \pm 0.2) \times 10^{-11}$		
	Fe ₂ O ₃	$(1.28 \pm 0.3) \times 10^{-11}$		
	Fly ash	$(0.8 \pm 0.2) \times 10^{-11}$		
Lindane	SiO ₂	6.0×10^{-13}		(Behnke and Zetzsch, 1989a)
Terbuthylazine	SiO ₂	$(1.1 \pm 0.2) \times 10^{-11}$	$\leq 5 \times 10^{-19}$	(Palm et al., 1997)
Pyrifenox	SiO ₂	$(1.8 \pm 0.4) \times 10^{-11}$	$(2 \pm 1) \times 10^{-19}$	(Palm et al., 1999)
DDT/dicofol	SiO ₂	5.4×10^{-12} (6.5°C)		(Munthe and Palm, 2003)
γ -HCH	SiO ₂	3.0×10^{-12} (6.5°C)		(Munthe and Palm, 2003)
Aldrin	SiO ₂	$(3.9 \pm 0.2) \times 10^{-11}$		(Gavrilov, 2007)

During the past years, there has been an emergence of research focusing on heterogeneous O₃ processing with semi-volatile compounds on atmospheric aerosol surfaces (Pöschl et al., 2001, Kwamena et al., 2004, 2006, Miet et al., 2009, Pflieger et al., 2009, Net et al., 2010). However, only a few studies have been concentrated on the gas-surface reaction of OH radicals with adsorbed pesticide on aerosols (Behnke and Zetzsch, 1989b, Palm et al., 1997, Palm et al., 1999, Bertram et al., 2001, Pflieger et al., 2013). Considering that the reactivity of OH radicals is much higher than ozone in the atmospheric heterogeneous reactions (based on published data, see that of table 1.2), more emphasis is needed on the study of OH radical reactions on the gas-solid interface.

Table 1.3 Summary of published data on ozone equilibrium and reaction rate constants of pesticides and selected SVOCs in the particulate phase (reaction rate constant are in units of $\text{cm}^3 \text{molecule}^{-1} \text{s}^{-1}$, at room temperature)

Compound	Carrier Particles	$K_{O_3}^*$ cm ³ molecule ⁻¹	k_{max}^I [#] s ⁻¹	k_{O_3} cm ³ molecu le ⁻¹ s ⁻¹	Reference
BaP	Soot	(2.8±0.2) ×10 ⁻¹³	0.015±0.001		(Pöschl et al., 2001)
	azelaic acid	(1.2±0.4) ×10 ⁻¹⁵ (<1% RH)	(0.048±0.008) (<1% RH)		(Kwamena et al., 2004)
		(2.8±1.4) ×10 ⁻¹⁵ (72% RH)	(0.060±0.018) (72% RH)		(Kwamena et al., 2004)
	NaCl (dry)	<1.2×10 ⁻¹⁶	0.032		(Kwamena et al., 2004)
Anthracene	Pyrex glass	(2.8±0.9) ×10 ⁻¹⁵	(6.4±1.8)×10 ⁻³ (<1% RH)		(Kwamena et al., 2006)
Cypermethrin	ZnSe	(4.7±1.7) ×10 ⁻¹⁶	(7±1)×10 ⁻⁴		(Segal-Rosenheimer and Dubowski, 2007)
Pyrene	Silica particle			(3.2±0.7) ×10 ⁻¹⁶	(Miet et al., 2009)
1-Hydroxypyrene	Silica particle			(7.7±1.4) ×10 ⁻¹⁶	(Miet et al., 2009)
1-Nitropyrene	Silica particle			(2.2±0.5) ×10 ⁻¹⁷	(Miet et al., 2009)
Trifluralin	Silica particle (AEROSIL®R812)	(3.4±3.6) ×10 ⁻¹⁶	(1.1±0.9) ×10 ⁻³	(2.9±0.1) ×10 ⁻¹⁹	(Pflieger et al., 2009)
Terbutylazine	Silica particle (AEROSIL®R812)			<0.5×10 ⁻¹⁹	(Pflieger et al., 2009)
4-Phenoxyphenol	Silica particle (AEROSIL®R812)	(9±3) ×10 ⁻¹⁴	9.95×10 ⁻⁶		(Net et al., 2010)
Isoprotruron	Silica particle (AEROSIL®R812)	(14.2±3.4) ×10 ⁻¹⁶	(19.8±3.4) ×10 ⁻⁴	(2.09±0.06) ×10 ⁻¹⁸	(Pflieger et al., 2012)

* K_{O_3} : Ozone gas-surface equilibrium constant, k_{max}^I : Maximum rate coefficient

1.2.5 Atmospheric lifetime and long range transport

The atmospheric lifetime of pesticides is mainly affected by chemical reactions in the atmosphere. Due to their low volatility, pesticides are distributed into the gaseous and particulate phases. For this reason, their atmospheric fate must be considered in both phases (Bidleman, 1999). As already mentioned, currently most of the atmospheric lifetimes of pesticides are estimated from the chemical reactivity of the gaseous phase using structure–reactivity relationships (SAR) which have been established for volatile hydrocarbons and oxygenated compounds (Kwok and Atkinson, 1995).

Considering the lack of kinetic data about heterogeneous reactions, the atmospheric lifetime of SVOCs calculated from gas phase kinetic data could be different from the real atmospheric condition. Esteve et al. (2006) have discovered that the heterogeneous reactivity of PAHs with OH radicals was inhibited on the carbonaceous surface, which has led to a slower degradation of PAHs. Scheringer et al. (2004) also proved that for several organochlorine compounds, the estimated lifetimes (according to gas-phase SAR data) are likely to be inconsistent with the observed long-range transport of these compounds, probably because of a lowered reactivity on the aerosol surface. Another example is that for α - and γ -HCH, Brubaker and Hites (1998) have reported about 100 days of the measured lifetimes in air from their measured OH-rate constants and Arrhenius parameters, while Howard et al. (1991) estimated the lifetimes of about 2 days for the hexachlorocyclohexanes (in accord with the present EPIWIN software of the US-EPA (Meylan, 1999)). Those results have shown a deviation of the previous calculation of atmospheric lifetimes of SVOCs, if based only on the gas-phase reactivity. There is a need to investigate the heterogeneous reactivity of pesticides on aerosol phase and give comprehensive evaluation of their fate in the atmosphere.

1.2.6 Introduction of terbuthylazine

Terbuthylazine (TBA) is a herbicide that is part of the chloro-triazine family. It acts as an inhibitor of photosynthesis. TBA is a selective herbicide for many kinds of crops and forests. It is especially effective against annual dicotyledons. About the

ecotoxicological properties, the risk of terbuthylazine to most animals was assessed as low, except the aquatic organisms (Anonymous, 2011).

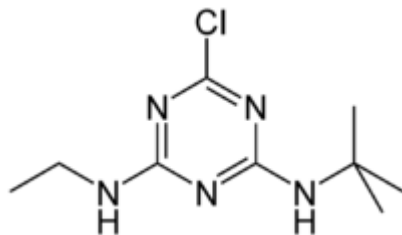


Figure 1.2 Molecular structure of terbuthylazine

Due to its low vapour pressure (1.2×10^{-4} Pa at 25°C (C.I.L., 2005)), terbuthylazine is easy to get adsorbed on particulate matter. Sauret et al. (2008) have confirmed in field measurements that in the real atmosphere, terbuthylazine was detected only in the particle phase. In this study, terbuthylazine was chosen as the objective as semi-volatile compound, which is adsorbed on aerosol surface for the present heterogeneous study. It is because of its low vapour pressure and the existing knowledge of its kinetic studies. The purpose of the experimental work is to understand whether there are differences of results from this work in comparison to previous studies or not in order to understand more about the heterogeneous processes on aerosols in the atmosphere.

1.3 Research objectives

The specific objective of this work is to understand the reaction dynamics of the reaction of OH radical with terbuthylazine which takes place on non-porous self-synthesized SiO_2 particles in aerosol simulation smog chamber.

In chapter 2, the experimental facilities are introduced. The smog chamber had been reconstructed after removal from Hannover and suited into a refrigerated laboratory in 2003. The instrumentation, the synthesis of the powder and the following coating procedure, dispersion of aerosol into the chamber and aerosol sampling technology are all explained in this chapter.

In chapter 3, the principle of how to calculate the kinetic of heterogeneous reactions is

presented. Both the Langmuir-Hinshelwood and the Eley-Rideal mechanism are introduced in this chapter. Those mechanisms are important for gas-surface kinetics studies, and have been already introduced into atmospheric studies.

In chapter 4, the method of OH radical production in the smog chamber is described. A comparison is made between different OH radical precursors. The way to introduce the OH precursor into chamber is also presented.

In chapter 5, the procedure of calculation is introduced, including an illustration how OH radical concentration was obtained, and how the apparent rate constant of heterogeneous reaction of terbuthylazine was finally achieved.

In chapter 6, the analysis of gaseous compounds and aerosols in the chamber is explained. Detailed information about aerosol characterization, and filter extraction technique is also given in this chapter.

In chapter 7, the experimental results are presented and followed by discussions. The monitoring results of temperature and NO_x and ozone concentration are shown. Results from every single experiment are summarized in tables. Those experiments were performed at different temperatures. Comparison of the results with other studies and the possible temperature independence are also discussed in this chapter. For the first time, the Langmuir-Hinshelwood and Eley-Rideal mechanism have been used to explain the heterogeneous reaction of OH radicals with aerosol-borne SVOCs. The major product has been analyzed and the possible reaction pathway is explained. The atmospheric implication is also being evaluated in this chapter.

In chapter 8, some conclusions will be given.

2. Experimental Description

In this chapter, the infrastructure used in this work will be introduced. It contains the smog chamber and all the instruments that are used for the experiments. The materials are also presented, including chemical reagents, as well as equipment used for reactions to synthesize new chemicals for this study.

2.1 LOW Temperature Aerosol Simulation Chamber (LOTASC)

The LOW Temperature Aerosol Simulation Chamber (LOTASC) was first built at the Fraunhofer-Institute of Toxicology and Experimental Medicine in Hannover in 1982 (Behnke et al., 1988). In 2003, it was moved to the University of Bayreuth (Figure 2.1).

The chamber is located in a temperature controllable room in which the temperature could be set from 25°C down to -25°C. The chamber consists of four cylinder sections made of glass (Duran, Schott, i.d. 1 m, total height 4 m), leading to a volume of 3200 L. Two FEP Teflon foils (DuPont FEP100, 200A film) are used to cover the top and bottom of chamber, in order to let the UV light penetrate into the chamber (Figure 2.2).

The chamber was originally designed for aerosol experiments. Due to the high volume, the aerosol in the chamber attains long suspension times, which are useful to simulate chemical reactions happening in the real ambient air.

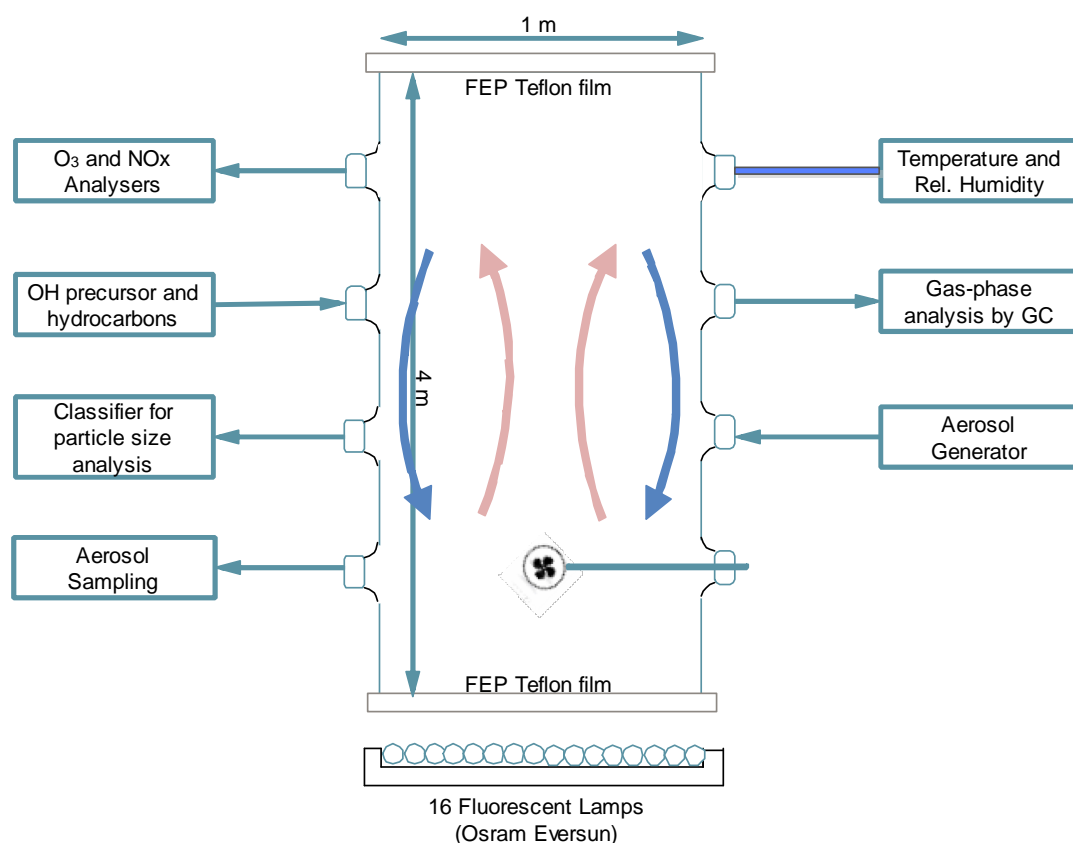


Figure 2.1 Glass chamber LOTASC (Low Temperature Aerosol Simulation Chamber)

At the bottom of the chamber, 16 fluorescent lamps (Osram Eversun) are used as light sources for the simulation experiments. Due to the heating effects caused by the lamps, a vertical temperature gradient is achieved, contributing to the well mixing of the chamber aerosols.

The chamber was typically cleaned after every 15 experiments by 0.1 mol/L NaOH solution to remove the substances sticking to the wall of chamber. The chamber is then flushed with deionized water. The Teflon foils are also changed during the cleaning process. The whole chamber is flushed with zero air until it is dry.

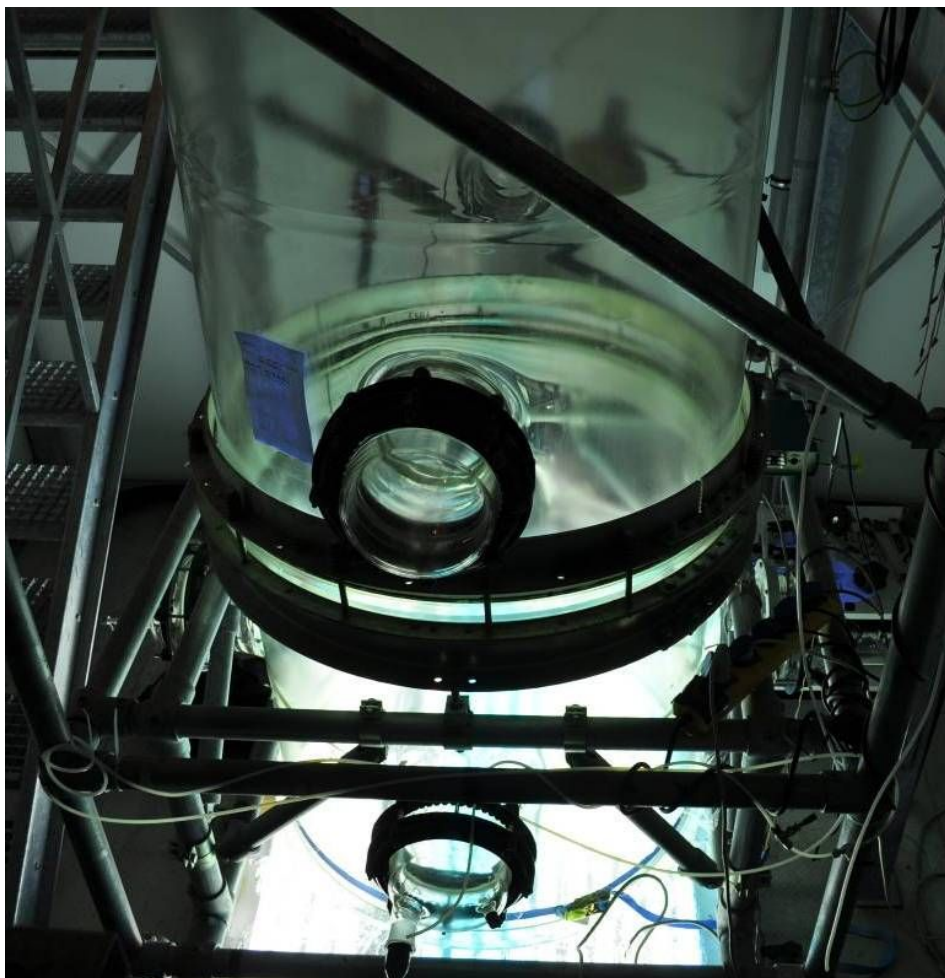


Figure 2.2 Photograph of the smog chamber with the solar simulator on

2.2 Measurement instruments connected with the chamber

2.2.1 Instruments

As shown in Figure 2.1, the chamber is being monitored by various instruments. A GC-FID (Siemens Sichromat II) with a pre-concentrator is used for gas-phase hydrocarbon analysis. Detailed parameters are listed below.

GC-FID Siemens Sichromat II:

Column: Al₂O₃-PLOT Chrompack, 50 m length; inner diameter 0.32 mm

Oven temperature: 190°C constant

Detector temperature: 230°C

Carrier gas: He 3 bar



Figure 2.3 Photograph of the GC-FID with the modified cold trap injector for hydrocarbons analysis

Pre-concentrator:

A self-designed cold trap injector is applied for monitoring the gas sample, combined with capillary chromatography. Detailed information has been described in previous papers (Behnke et al., 1987, 1988, Nolting et al., 1988). A peristaltic pump (Ismatec, VP Antrieb) took gas samples from the smog chamber through a glass-lined stainless steel tube inside the cold trap. Liquid nitrogen was used for cooling to a temperature of 148K in order to avoid condensation of air. The glass lined tube is then heated to introduce the collected hydrocarbons into the chamber.

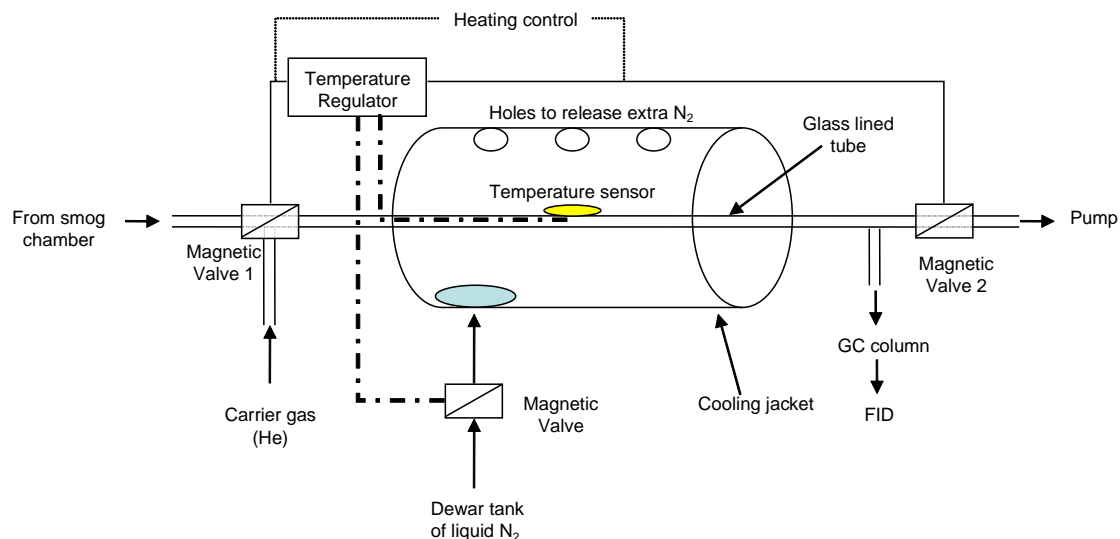


Figure 2.4 Schematic flowchart of the cold trap injector for gas chromatographic analysis of the gas phase in the smog chamber

O₃ analyzer & NO_x analyzer

O₃ analyzer: Thermo Scientific, MLU Model 49i

NO_x analyzer: ECO Physics, CLD 88P

Aerosol particle size analyzer-classifier

Electronic Classifier: TSI, Thermo-Systems Inc., Model 3071

Condensation Nucleus Counter: TSI, Thermo-Systems Inc., Model 3020

Filter extraction analysis: GC-FID Siemens Siechromat I with on-column injection

Column: CP-SIL-5CB, 1.13 μm film thickness, i.d. = 0.32 mm, column length 50 m

Detector: FID at 250 °C

Carrier gas: nitrogen at 2 bar

Temperature program: 50 °C elevated to 265 °C at 25 °C/min

Injected volume: 5 μL



Figure 2.5 Photograph of the GC-FID with on-column injector for filter sample analysis

2.2.2 Solar simulator

Fluorescent lamps were used as light source. Figure 2.6 shows the spectrum of the solar simulator (Gavrilov, 2007) in comparison with the sun spectrum in Europe (Frank and Klöpffer, 1988). In the spectrum, the usual mercury lines of the fluorescent lamps could be observed (313, 334, 366, 408 and 436 nm). Those lines serve for

calibration of the wavelength scale of the monochromator. The mercury line at 313 nm could have an impact on the photolysis of the OH precursors, especially if hydrogen peroxide is used as OH precursor.

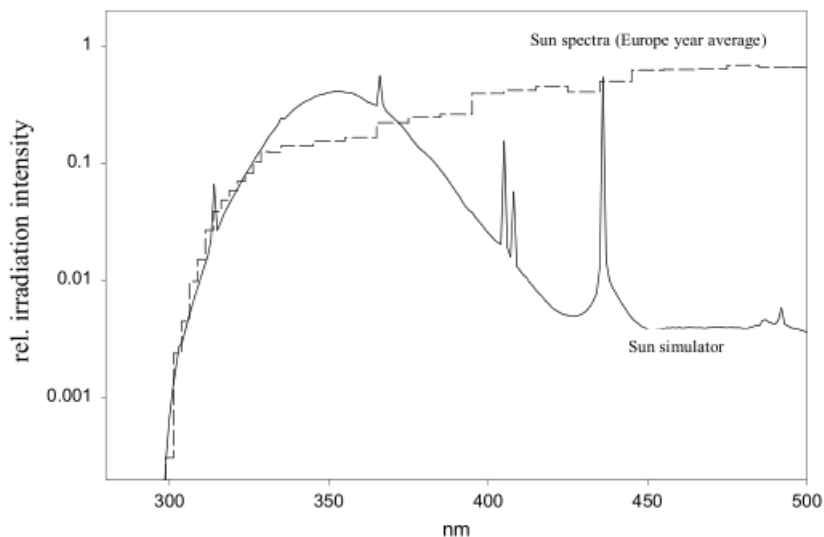


Figure 2.6 Spectrum of the solar simulator (16 fluorescence lamps Osram Eversun), in comparison with the actual sun in Europe (taken from Gavrilov 2007)

2.2.3 Temperature and relative humidity sensor

Two temperature sensors are installed onto the smog chamber in order to measure the temperatures in the middle of the chamber and close to the walls. They were placed in the middle and at the top of the chamber, respectively.

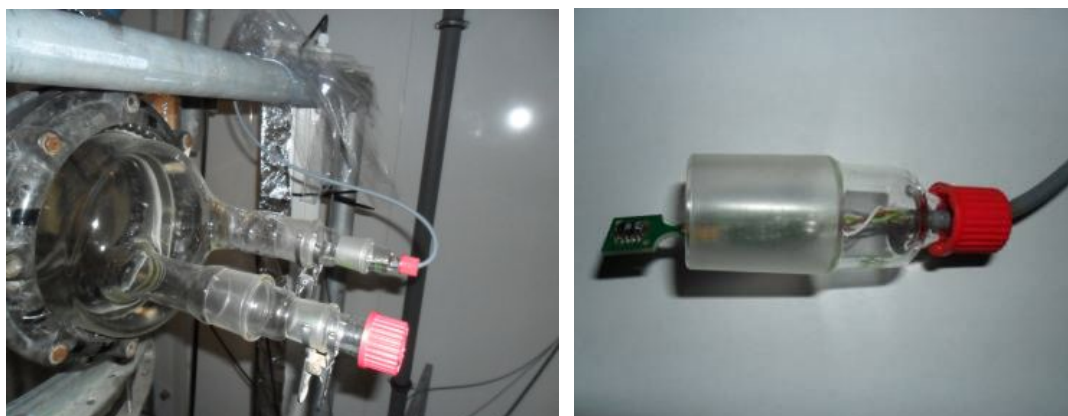


Figure 2.7 Photograph of the temperature and humidity sensor (situated at the uppermost section of the chamber (DKRF 4001-P, Driesen und Kern))

The sensor in the middle of the chamber is a thermistor (Epcos NTC 50K, thermal

time constant 3s), calibrated against a Pt100 reference resistance thermometer (Keithley 195A with probe 8693) from -40°C to +30°C.



Figure 2.8 photograph of the temperature sensor (in the middle of the chamber)

2.3 Aerosol coating, generation and sampling

2.3.1 Synthesis of the silicon dioxide particles

A system of chemical reactions has been developed which could control the growth of spherical silica particles to a uniform size (Stöber and Fink, 1968). This method employs the hydrolysis of alkyl silicates and subsequent condensation of silicic acid in alcoholic solutions. Ammonia is used as a morphological catalyst. By using this method, silica particles were synthesized with a diameter of about 160 nm with a standard deviation of 5 nm.

The method used tetraethylorthosilicate (TEOS) in the presence of a C₂H₅OH/NH₃/H₂O mixture. The ratio between the NH₃ and H₂O concentration controlled the particle size. Particles with diameter at approximately 200 nm were expected.

Reagents used for the experiments:

C₂H₅OH (Merck, ≥99.9%): 188 mL

H₂O (double-distilled and deionized water): 6 mL

NH₃/H₂O solution (Sigma-Aldrich, 28-30%): 8 mL

TEOS (Sigma-Aldrich, 99.999%): 8 mL

Those four ingredients were added one by one into a 500 mL glass flask. The mixture was then stirred by a magnetic stirrer at room temperature (magnetic stirrer set at 300 rpm). After 18 hours, the precipitated nanometer-sized silica spheres were separated from the solvent mixture by an induction drive centrifuge (Beckman, Model J2-21M).

Parameters used for the centrifuge:

Rotor speed: 5000 rpm

Centrifuge temperature: 20 °C

Centrifuge time: 60 minutes

After separation from the liquid, the obtained white powder was placed in an oven at 100 °C for 16 hours and weighed afterward. Then the powder was put back into the oven for another 4 hours and weighed again. If there was no mass loss found for the particles, it was assumed that H₂O, C₂H₅OH or NH₃ had been evaporated completely during this procedure.

The mean diameter of the silica spheres was determined by a scanning electron microscope (Zeiss LEO1530, Field Emission-SEM) to be about 160 nm (see also Appendix 2).

2.3.2 Coating of the particles with terbuthylazine

The purpose of this step is to ensure a monolayer-coating with molecules of the semi-volatile organic compound TBA on the surface of the single inert particle. The SiO₂ powder (1.0 g) was mixed with TBA powder (47 mg) in dichloromethane and then dried in a rotary evaporator (Edmund Bühler, Type RV2, Tübingen).

The mass fraction of terbuthylazine on the dried particles is approximately equal to the mass ratio and thus defined as below:

$$F_{\text{TBA}} (= \text{mass fraction of TBA}) = \frac{\text{mass TBA}}{\text{mass aerosol}}$$

That leads to a mass fraction of TBA on the aerosol of $F=0.047$, theoretically.

The SiO₂ powder was first weighed and then put into a 500 mL round bottom flask, where 50 mL CH₂Cl₂ was added. Then the flask was put into the ultrasonic bath for 30 minutes. The TBA powder was weighed on a microbalance (Sartorius, type SC02) and transferred into the flask with SiO₂ and CH₂Cl₂ inside, another 5 mL of CH₂Cl₂ was added and the flask was put into the ultrasonic bath for 10 minutes. The flask was then connected with the rotary evaporator and a water bath was put around the flask to achieve a gentle heating (30-32 °C), thus minimizing loss of TBA. The pressure in the rotary evaporator was kept at 500 Torr. After all CH₂Cl₂ was evaporated, the white powder was gently milled for about 2 minutes and then stored in a 500 mL flask. The flask was then wrapped with aluminum foil to eliminate any photolysis effect and sealed with Teflon tape. According to experimental consumptions, the coated powder is replaced after 3-6 months.



Figure 2.9 Coated powder in the rotary evaporator

2.3.3 Structure analysis of the carrier particles

In order to see the surface characteristics of those self-synthesized SiO₂ particles,

SEM (Scanning Electronic Microscopy, Zeiss LEO1530, Field Emission-SEM, column: Gemini, Detector: InlensSEM and SE2SEM) and EFTEM (Energy Filtering Electron Microscope, Zeiss CEM902, for detailed parameters see appendix) were applied in this study. Figure 2.10 and Figure 2.11 show the images under SEM and EFTEM, respectively. From those images, it can be clearly seen that the self-synthesized SiO₂ particles exist as round spheres. Figure 2.11 also shows that the surfaces of such spheres are very smooth. Both images indicate that the self-synthesized SiO₂ particles have uniform size.

The information on particle size could also be measured and labeled in the images. The average diameter of the self-synthesized particles is 159.8 ± 5.0 nm (see appendix 2).

Based on the measurement result of the diameter of the self-synthesized SiO₂ particles, the mass specific surface area (SA) could be estimated, according to the following calculation:

$$SA = \frac{\pi \cdot D^2}{m} = \frac{\pi \cdot D^2}{\rho \cdot V} = \frac{\pi \cdot D^2}{\rho \cdot \frac{4}{3} \cdot \pi \cdot \left(\frac{D}{2}\right)^3} = \frac{6}{D \cdot \rho} \quad 2.1$$

where ρ is the particle density (for fused silica, $\rho=2.2 \text{ g cm}^{-3}$) and D is the diameter of a particle. The surface area is then calculated as

$$SA = 6 / (160 \times 10^{-9} \text{ m} \times 2.2 \times 10^6 \text{ g m}^{-3}) = 17.05 \text{ m}^2 \text{ g}^{-1}$$

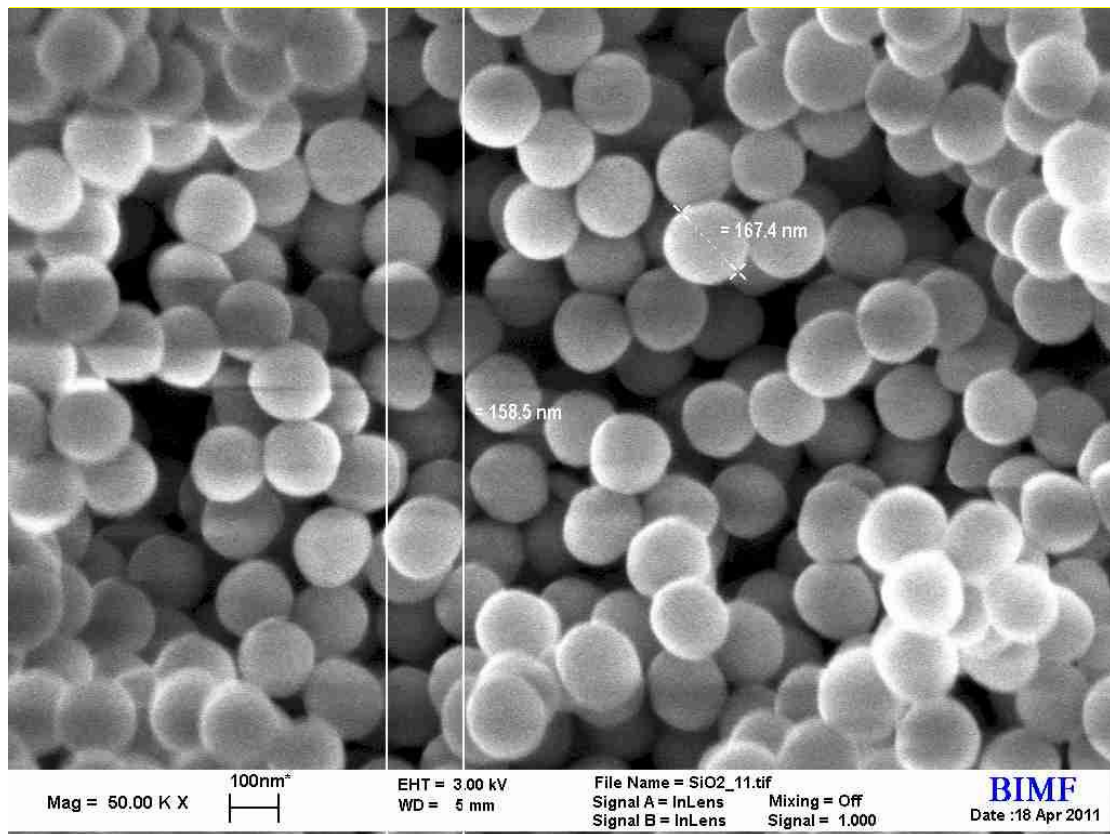


Figure 2.10 SEM image of the self-synthesized SiO₂ particles

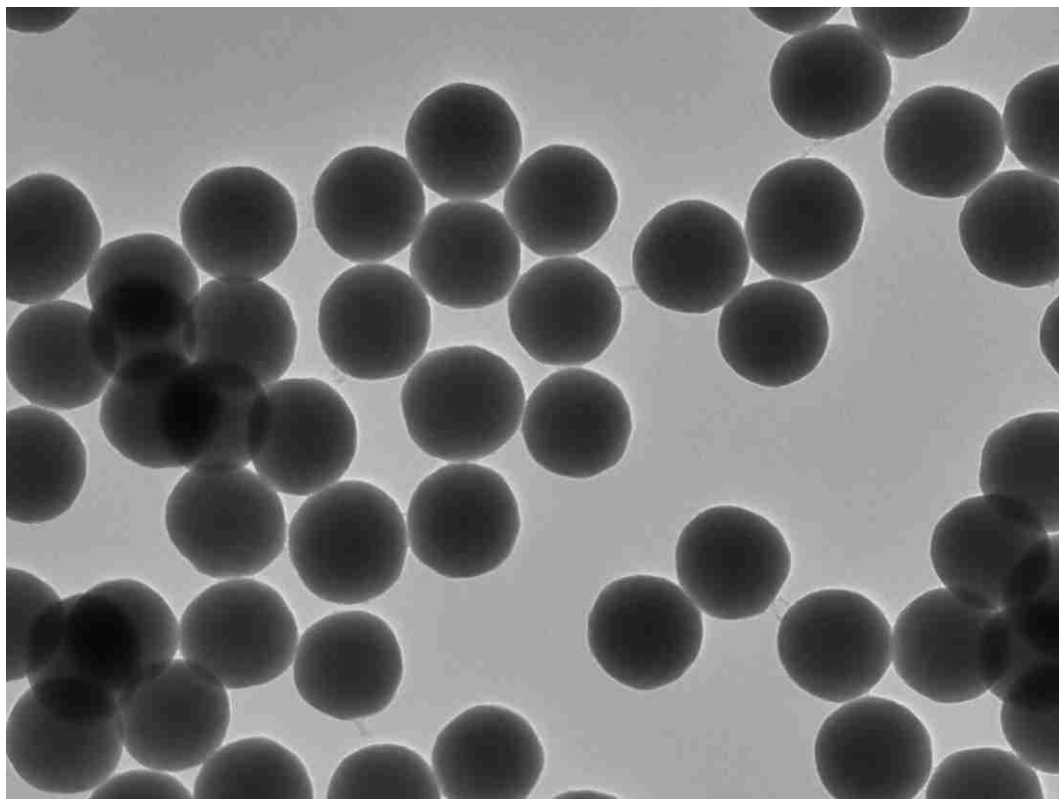


Figure 2.11 EFTEM image of the self-synthesized SiO₂ particles

2.3.4 Calculation of the coverage ratio of terbuthylazine on SiO₂ particles

Table 2.1 Information of terbuthylazine and SiO₂ needed for the coverage ratio calculation.

	Mass	M (molar mass, in g mol ⁻¹)	Bulk density (g mL ⁻¹)	Size of particles (nm)
TBA	47.078 mg	229.71	1.19	-
SiO ₂	1.001 g	60.08	2.2	160

One may try to estimate the surface coverage by TBA from the molecular structure for special orientations on the surface, starting from typical bond lengths (Allen et al., 1987):

- A: -C=N-C (conjugated) 1.476 Å
 B: X₃-C-Cl (X=C, H, N, O) 1.843 Å
 C: -NH-C (overall) 1.380 Å

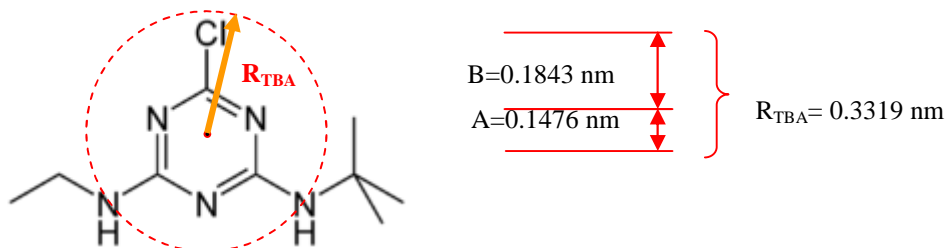


Figure 2.12 Scheme of the molecule structure of terbuthylazine and calculation of the maximum diameter of the plane area within molecule

The adsorption might be assumed to occur on a confined circle within the terbuthylazine molecule (as described above), the aromatic triazine ring. If the C-Cl bond is used as part of the longest radius, generating a radius R_{TBA} ($A+B$) shown in Figure 2.12, a maximum plane circle area could be calculated as Equation 2.2:

$$S_{TBA\text{molecule-max}} = \pi \cdot R_{TBA}^2 = 0.1102\pi \cdot \text{nm}^2 \quad 2.2$$

The hypothesis is made that the minimum number of adsorbed TBA molecules on the SiO₂ sphere is caused by adsorption via the plane circle with radius of R_{TBA} (in nm).

Then if the number of overall TBA molecules in this system is less than the maximum number of TBA molecules that could be adsorbed by the SiO₂ sphere, the TBA molecules adsorb to the SiO₂ surface as a monolayer.

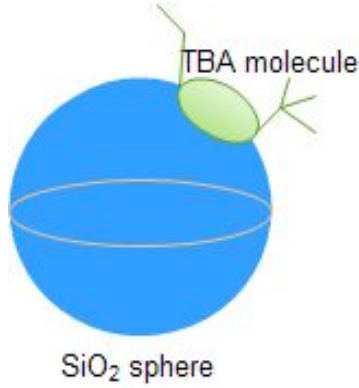


Figure 2.13 Illustration diagram of adsorption of TBA molecule to the SiO₂ surface

Based on the surface area data of SiO₂ particles, the minimum number of TBA ($N_{\text{TBA-monolayer}}$) that could be adsorbed onto the SiO₂ surface as a monolayer coating is calculated as below (Equation 2.3):

$$N_{\text{TBA-monolayer}} = \frac{SA \times m_{\text{SiO}_2}}{S_{\text{TBA molecule-max}}} = \frac{17.05 \text{m}^2/\text{g} \times 1.001 \text{g}}{0.1102\pi \times 10^{-18} \text{m}^2} = 4.9 \times 10^{19} \text{ molecule} \quad 2.3$$

The total number of TBA molecules in 47mg is calculated in Equation 2.4:

$$N_{\text{TBA}} = \frac{m_{\text{TBA}}}{M_{\text{TBA}}} \times N_A = \frac{47 \text{mg}}{229.71 \text{g/mol}} \times 6.02 \times 10^{23} \text{ molecule/mol} = 1.2 \times 10^{20} \text{ molecule} \quad 2.4$$

In this case, the N_{TBA} is slightly bigger than $N_{\text{TBA-monolayer}}$, indicating a possibility of molecular agglomeration of TBA molecules on the SiO₂ surface. However, the lone-pair electrons of the amino groups of TBA can interact with the protons on the hydrophilic aerosol surface to form hydrogen bonds. This would enable the molecule to stand upright (with a possibly lower area demand), forming an ordered, quasi-crystalline monolayer. Considering about this effect, the aerosol coating in this work is regarded as monolayer coating.

2.3.5 Generating aerosols in the chamber

The aerosol is introduced into the smog chamber through a motor-driven syringe (Perfusor Secura, Braun) through a nozzle (Schlick S8), see Figure 2.14. The size distribution of the aerosol suspensions inside the chamber was then measured by an electrostatic classifier (TSI, model 3071) and a condensation nuclei counter (TSI, model 3020).

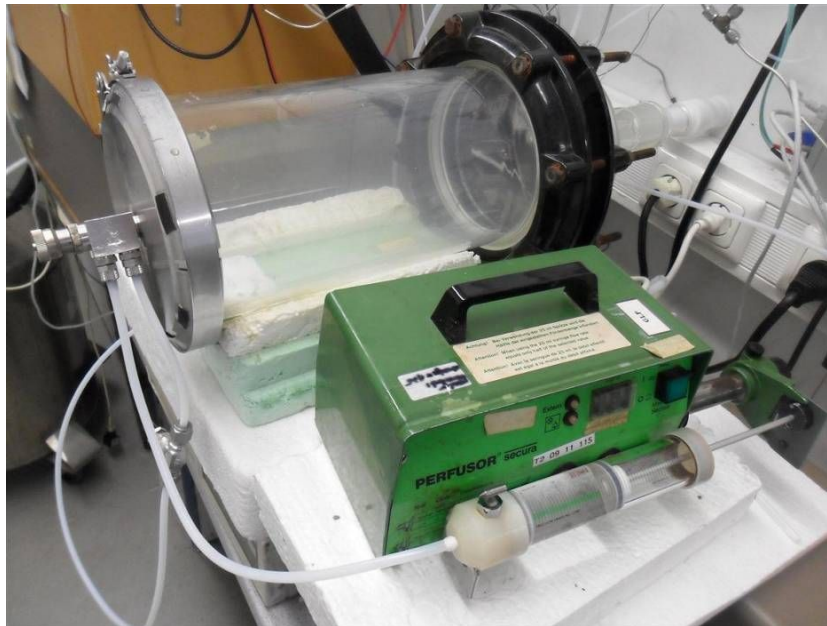


Figure 2.14 Motor-driven syringe and nozzle for injection of the suspension into the chamber



Figure 2.15 Photograph of the electrostatic classifier and condensation nucleus counter

2.3.6 Sampling of particles

As shown in Figure 2.16, the aerosol sampling device consists of a glass tube (L=160 cm, i. d. =16 mm, o. d. =20 mm, reaching the middle of the chamber), a filter holder (Figure 2.17), and a vacuum pump. Those parts are connected by Teflon tubes. A gas meter is used to record the air flow. Filter samples are taken on Teflon filters (Satorious, PTFE filter, d = 25 mm, pore size = 0.2 μm).

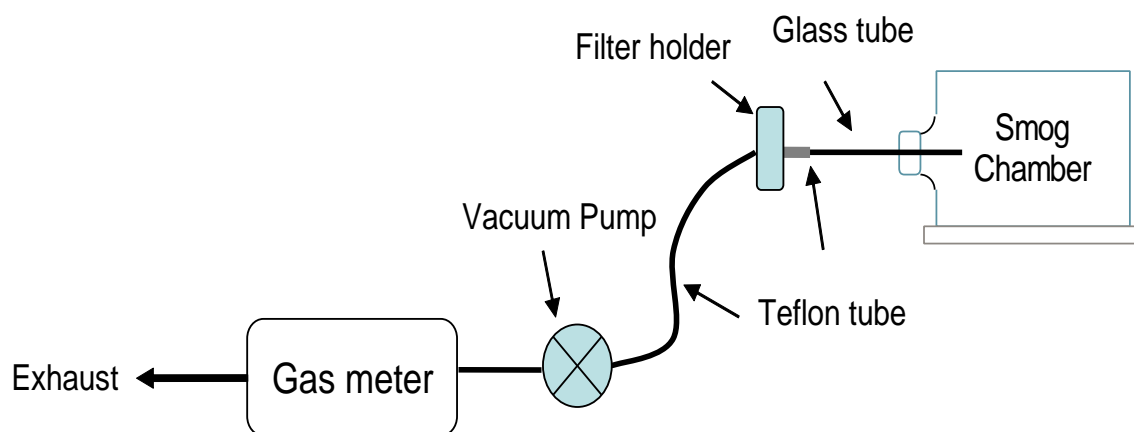


Figure 2.16 Schematic diagram of the aerosol sampling device. A glass tube was connected to the smog chamber, followed by a filter holder connected by a short Teflon tube. Aerosols were pumped out from the chamber by a vacuum pump. The sampling volume was measured by a gas meter.



Figure 2.17 Photograph of the filter holder with inserted Teflon filter

2.4 Reagents in the experiments

2.4.1 Chemicals and materials

Hydrocarbons:

n-Pentane (Grüssing, 99%)

n-Heptane (Fluka AG, UV Spectroscopy grade, >260nm, >99%)

2,2-Dimethylbutane (Janssen Chimica, 96%)

2,2,4-Trimethylpentane (Janssen Chimica, 99+%)

2,2,3,3-Tetramethylbutane (Sigma-Aldrich)

Toluene (Carl Roth, RotiSolv HPLC)

Inert standard:

n-Perfluorohexane (Sigma-Aldrich, 99%)

Solvents:

Dichloromethane (Sigma-Aldrich, Chromasolv, >99.8%)

2.4.2 Synthesis of methyl nitrite

Materials:

H₂SO₄: Analytical reagent grade, S. G. 1.83 (>95%), Fischer Scientific

Methanol: RotiSolv HPLC, ≥99.9%, Carl Roth

NaNO₂: p.a. ≥99%, Grüssing

NaOH: p.a. ≥99%, Merck

CaCl₂ · 2H₂O: p.a. ACS, ≥99%, Carl Roth

Procedure:

20 g NaNO_2 and 200 mL methanol were added into a 500 mL 3-necked flask one after another, N_2 was used as carrier gas (0.5 L/min, after the first 3 minutes the flow could be less). The flask was then placed inside an ice bath, and a magnetic stirrer was applied during the reaction. Slowly adding 100g 50% H_2SO_4 solution within 3 min generated the methyl nitrite. After passing through NaOH solution and dehydrating agent (CaCl_2), the methyl nitrite was collected in a cold trap. After the reaction was finished, the liquid methyl nitrite was transferred into a 2 mL vial and stored in a Dewar tank in liquid nitrogen (see Figure 2.18 and 2.19).

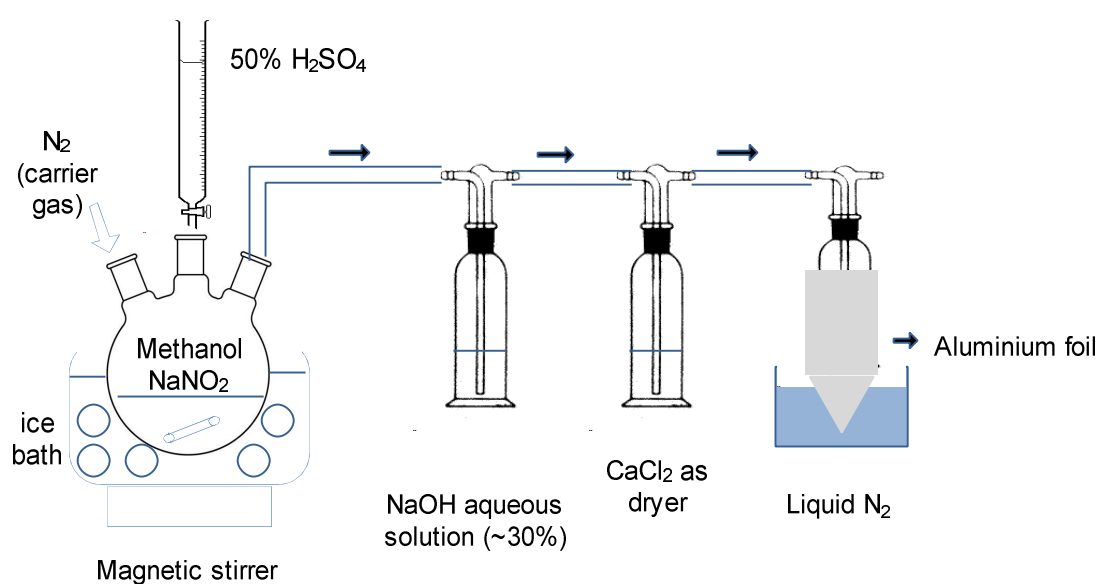


Figure 2.18 Schematic diagram of the synthesis of methyl nitrite



Figure 2.19 Photograph of the system for the synthesis of methyl nitrite

3. Kinetics of heterogeneous reactions

3.1 Langmuir-Hinshelwood mechanism

The pioneers Langmuir (Langmuir, 1918) and Hinshelwood (Hinshelwood, 1940) first raised the mechanism on solid catalyzed reactions, explaining how the gas phase reactions could happen with the assistance of a solid as catalyst. The mechanism and the Langmuir-Hinshelwood equations have been widely used to explain the photocatalytic processes (Turchi and Ollis, 1990, Jenny and Pichat, 1991, Sun and Pignatello, 1995, Lin and Gurol, 1998, Sauer et al., 2002, Sobczykński et al., 2004, Konstantinou and Albanis, 2004, Okitsu et al., 2005). Recently this mechanism has been applied to explain the heterogeneous reaction with O_3 on atmospheric particles (Alebić-Juretić et al., 2000, Kwamena et al., 2006, Kahan et al., 2006, Pflieger et al., 2009, Yang et al., 2010).

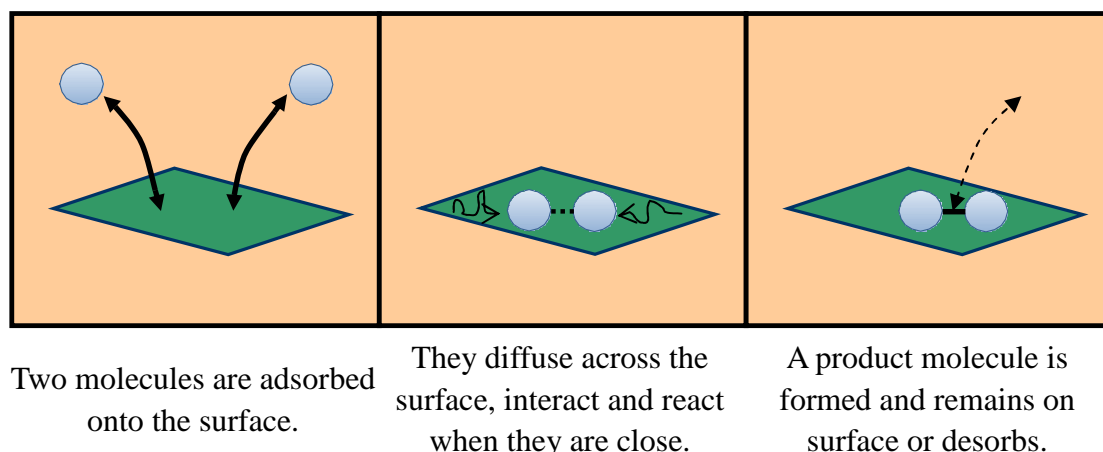
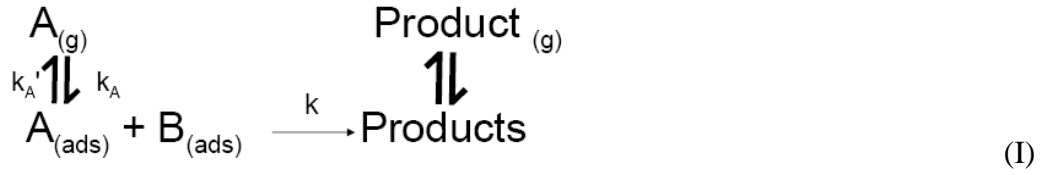


Figure 3.1 An illustration of molecules reacting according to the Langmuir-Hinshelwood mechanism

In case of this work, the terbuthylazine (refers to reactant B) molecules were adsorbed to the SiO_2 particles through rotary evaporation instead of gas-particle adsorption equilibrium; the general mechanism which illustrates the reaction pathways is described below (A refers to the OH radical):



The global reaction rate is:

$$r = -\frac{dC_A}{dt} = k \cdot C_{AS} \cdot C_{BS} = k \cdot \theta \cdot C_S \cdot C_{BS} \quad 3.1$$

Here r is the reaction rate, in molecule $m^{-2} s^{-1}$, k is the reaction rate constant, in $m^2 \text{ molecule}^{-1} s^{-1}$, C_{AS} , C_{BS} are the surface concentrations of sites occupied by A and B, in molecule m^{-2} , θ is the surface coverage by A, dimensionless, C_S is the total number of sites (occupied or not), in molecule m^{-2} , t is the time, in s.

The rate of adsorption of the reactant A is proportional to the fraction of unoccupied surface and the partial pressure. After the adsorptive equilibrium of A is achieved, the adsorbed molecules react with each other when they have come close to each other by diffusion. The reaction rate between the adsorbed compounds is proportional to the amounts on the surface. After the reaction, the product molecules could be desorbed from the surface when there are no longer bonds linked with the surface.

If we apply the steady state approximation to AS, then

$$\frac{dC_{AS}}{dt} = 0 = k_A \cdot C_A \cdot C_S \cdot (X - \theta) - k \cdot C_{AS} \cdot C_{BS} - k_A' \cdot C_{AS} \quad 3.2$$

Here k_A and k_A' are the adsorption and desorption rates of A, and X is the fraction of available sites after B has been adsorbed onto the surface; Equation 3.2 is then transformed to Equation 3.3:

$$k_A \cdot C_A \cdot C_S \cdot (X - \theta) - k \cdot \theta \cdot C_S \cdot C_{BS} - k_A' \cdot \theta \cdot C_S = 0 \quad 3.3$$

So

$$\theta = \frac{k_A \cdot C_A \cdot X}{k_A \cdot C_A + k \cdot C_{BS} + k_A'} \quad 3.4$$

Equation 3.1 is then expressed as below:

$$r = -\frac{dC_A}{dt} = \frac{k \cdot k_A \cdot C_A \cdot X \cdot C_S \cdot C_{BS}}{k_A \cdot C_A + k \cdot C_{BS} + k_A} \quad 3.5$$

If the limiting step is the reaction, then $k \ll k_A \cdot C_A$, k_A , and $k_{\max}^1 = k \cdot X \cdot C_S \cdot C_{BS}$ is the maximum reaction rate constant in case that all the available surface sites are occupied by A and the reaction happens between adsorbed species A and B. With $K_A = k_A / k_A$, Equation 3.5 is then transformed into Equation 3.6 as below:

$$r = \frac{k_{\max}^1 \cdot K_A \cdot C_A}{K_A \cdot C_A + 1} \quad 3.6$$

Currently, most research focused on the heterogeneous reaction of semi-volatile compounds with gas-phase ozone. However, there are only a few adsorption sites that are involved in the saturation of the surface (Ammann et al., 2003). Within the experimental conditions, as the OH precursor is introduced into the chamber continuously and thus resulting a circumstance with constant OH radicals, the rate of the reaction becomes independent of the OH concentration. In this work, Equation 3.6 is specified as below:

$$k_{\text{obs}}^1 = \frac{k_{\max}^1 \cdot K_{\text{OH}} \cdot C_{\text{OH}}}{(1 + K_{\text{OH}} \cdot C_{\text{OH}})} = k_{\text{OH}} \times C_{\text{OH}} \quad 3.7$$

Here k_{obs}^1 is the experimental pseudo-first-order rate constant, in s^{-1} , k_{\max}^1 is the maximum rate constant that would be observed at high OH radical concentrations, in s^{-1} , K_{OH} is the OH radical gas-to-surface equilibrium constant, in $\text{cm}^3 \text{ molecule}^{-1}$, k_{OH} is the OH radical reaction rate constant, in $\text{cm}^3 \text{ molecule}^{-1} \text{ s}^{-1}$, C_{OH} is the gas-phase OH radical concentration, in molecule cm^{-3}

If the OH level remains constant during the experiment period, Equation 3.7 can be converted to the following expression:

$$k_{\text{OH}} = \frac{k_{\max}^1 \cdot K_{\text{OH}}}{(1 + K_{\text{OH}} \cdot C_{\text{OH}})} \quad 3.8$$

From Equation 3.8, the parameters k_{\max}^1 and K_{OH} can be obtained by applying a

nonlinear least-squares fit or a linear fit to $1/k_{OH}$.

Reactions on surfaces with reactive organic species:

In some cases, there could be organic species adsorbed onto the surface of the particle. Since Bertram et al. (2001) have determined the reaction probability of OH with a methyl-terminated monolayer in a flow reactor to be larger than 0.29, those adsorbed state organic species can also react with OH radicals in the following way:



k_{other} is the reaction rate of substance A with organic impurities on the particle surface.

Following the same calculation process, the reaction rate is calculated as below:

$$r' = \frac{k \cdot k_A \cdot C_A \cdot X \cdot C_S \cdot C_{BS}}{k_A \cdot C_A + k \cdot C_{BS} + k_{A'} + k_{other} \cdot C_{organic}} = \frac{k_{max}^I \cdot K_A \cdot C_A}{K_A \cdot C_A + 1 + \frac{k_{other} \cdot C_{organic}}{k_{A'}}} \quad 3.9$$

k_{max}^I remains the same, and $r' < r$. If there are organic impurities on the surface, the apparent reaction rate is found to be lower than that on the pure surface, until the maximum reaction rate is reached. Bertram et al. (2001) found that the reaction probability of OH radicals had slightly differences on difference organic surfaces, which were caused by the k_{other} value.

Gas-particle adsorption equilibrium on both reactant molecules:

If the gas-particle adsorption equilibrium is also relevant to the terbuthylazine molecule, reaction mechanism I is changed into reaction mechanism III



k_B and $k_{B'}$ are adsorption and desorption rates of B (terbuthylazine), the rate law is:

$$r = k \cdot \theta_A \cdot \theta_B \cdot C_S^2 \quad 3.10$$

Proceeding as before, we get

$$\theta_A = \frac{k_A \cdot C_A \cdot \theta_E}{k_{A'} + k \cdot C_S \cdot \theta_B} \quad 3.11$$

Here θ_E is the fraction of empty sites, then $\theta_A + \theta_B + \theta_E = 1$. The hypothesis is made that

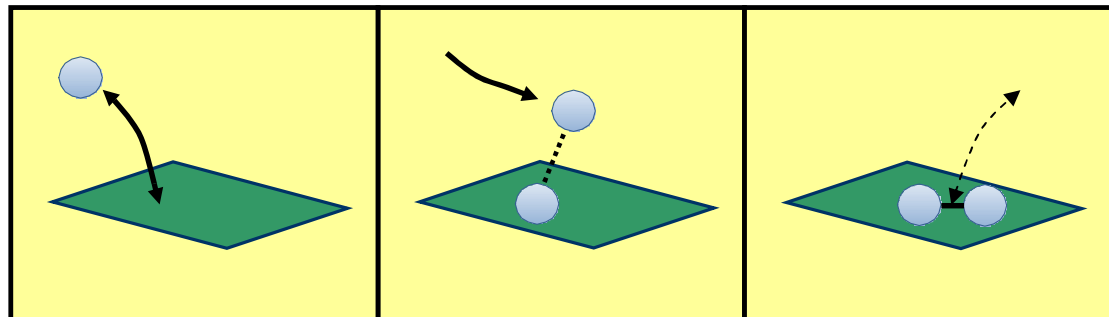
the rate limiting step is the reaction of the adsorbed molecules (the probability of two adsorbed molecules colliding is low), then $\theta_A = K_1 \cdot C_A \cdot \theta_E$. With adsorption constants $K_B = k_B/k_{B'}$, the reaction rate becomes

$$r = \frac{k \cdot C_S^2 \cdot K_A \cdot C_A \cdot K_B \cdot C_B \cdot \theta_E}{1 + K_A \cdot C_A + K_B \cdot C_B} \quad 3.12$$

In this work, the desorption of terbuthylazine to the gas phase is supposed to be very slow, so $K_B \cdot C_B \ll 1$, $K_A \cdot C_A$, and $k_{\max}^1 = k \cdot C_S^2 \cdot \theta_E \cdot K_B \cdot C_B$ (all empty surface sites are occupied by reactants), Equation 3.12 is then transformed to the same expression as Equation 3.6.

3.2 Eley-Rideal mechanism

The Eley-Rideal mechanism was proposed by Eley and Rideal (1941) more than 70 years ago. Unlike the Langmuir-Hinshelwood mechanism, the Eley-Rideal mechanism assumes that only one of the molecules adsorbs on the surface and the other one directly reacts with it from the gas phase, instead of adsorbing:



One molecule is adsorbed onto the surface. Another molecule passes by which interacts with the one on the surface. A product molecule is formed and remains on surface or desorbs.

Figure 3.2 An illustration of the reaction procedure during an Eley-Rideal mechanism

Under the experimental conditions of this work, the OH precursor methyl nitrite was introduced into the chamber continuously, and the OH level was in surplus with regard to the adsorbed pesticides. In this case, the dynamics of the reactions could be

assumed as a pseudo-first order reaction. The following equation is then generated.

$$k_{\text{obs}}^I = \frac{1}{t} \cdot \ln \left(\frac{C_{\text{TBA(ads)0}}}{C_{\text{TBA(ads)t}}} \right) = k_{\text{OH}} \cdot C_{\text{OH}} \quad 3.13$$

$C_{\text{TBA(ads)0}}$ and $C_{\text{TBA(ads)t}}$ represent the adsorption state concentration of terbuthylazine at initial time and time t , respectively; C_{OH} is the gas phase OH radical concentration. In the actual calculation applied in this study, we use the following equation for variable C_{OH} :

$$\ln \left(\frac{C_{\text{TBA(ads)0}}}{C_{\text{TBA(ads)t}}} \right) = k_{\text{OH}} \cdot C_{\text{OH}} \cdot t = k_{\text{OH}} \cdot \int_0^t C_{\text{OH}} \cdot dt \quad 3.14$$

If we plot $\ln \left(\frac{C_{\text{TBA(ads)0}}}{C_{\text{TBA(ads)t}}} \right)$ as a function of the time integral OH gas phase concentration, we get a linear plot, with k_{OH} as slope.

In this work, both the Langmuir-Hinshelwood mechanism and the Eley-Rideal mechanism are used for the calculation of experimental data. The results show that the application of each mechanism has been in association with the level of OH radical concentration and the characteristics of carrier particles. The Eley-Rideal mechanism corresponds to a Langmuir-Hinshelwood mechanism for the limit of low C_{OH} .

4. Production of OH radicals in the chamber

In this chapter, the ways to produce OH radicals will be described below. OH radicals could be generated through chemical reactions with / without the presence of a light source. Based on the spectrum of solar simulator, some precursors have limitation and could not be used in this study. The detailed reaction mechanism will also be described in this chapter.

4.1 Sources of OH radicals

In chamber simulation experiments, the OH radicals were produced by chemical reactions in the presence of a light source or during dark period. Photolysis of precursors is used more often to generate OH radicals. An efficient OH production method is the photolysis and consecutive photochemical reactions of H_2O_2 , O_3 , HONO or methyl nitrite (see Figure 4.1).

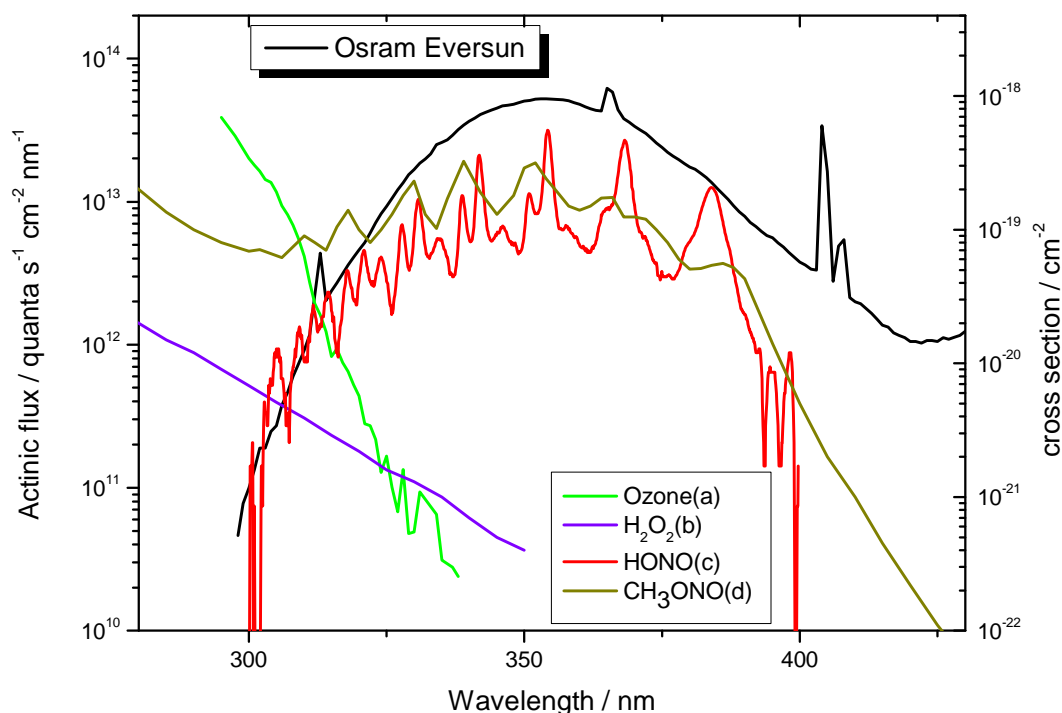
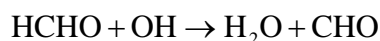
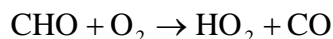
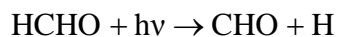
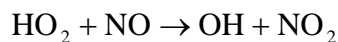
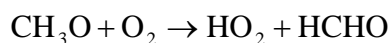
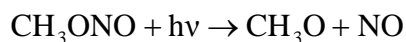


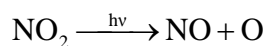
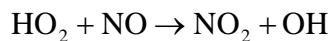
Figure 4.1 Overlap of the solar simulator spectrum with the spectra of ozone, hydrogen peroxide, HONO and methyl nitrite (a. Voigt et al. 2001; b. Sander et al., 2002; c. Bongartz et al., 1991; d. Taylor et al., 1980)

Methyl nitrite:



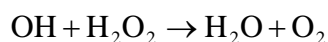
As the other precursors have small overlap with light source (see Figure 4.1), methyl nitrite is used as precursor in existence of light, and a high concentration of OH radicals could be obtained ($\sim 10^7$ molecule cm^{-3}). However, ozone and NO_x compounds are also produced as byproducts in the system. The ozone level can build up to a few ppm by the end of the photolysis.

Ozone can be formed by photolysis of NO_2 :



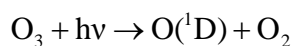
$\text{O} + \text{O}_2 + \text{M} \rightarrow \text{O}_3 + \text{M}$ (the Leighton relationship, see Finlayson-Pitts and Pitts Jr., 2000).

H_2O_2 :



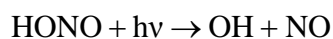
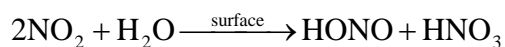
Beside the above two methods, there are two more pathways to generate OH radical under photochemistry conditions: (1) photolysis of ozone; (2) chemical reactions initiated by nitrogen dioxide (or photochemical reaction of HONO) in the presence of humid aerosols (Lammel and Cape, 1996).

Ozone:

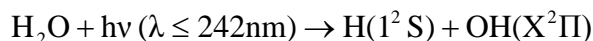




Nitrogen dioxide/HONO:



One possible OH source is the photolysis of water vapour (Ung, 1974):



However, in this spectral region, our lamps do not irradiate. As a result, there are no hydroxyl radicals produced.

OH radicals can also be produced through the dark reaction of ozone with olefins (trans-2-butene) (Orzechowska and Paulson, 2005) or hydrazine (Tuazon et al., 1983).

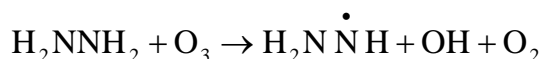
trans-2-Butene



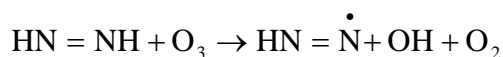
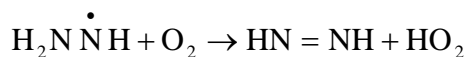
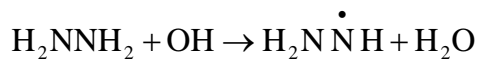
H₂NNH₂:

The reaction of hydrazine with O₃ follows a chain mechanism, from which N₂H₃, N₂H₂ and OH act as chain carrier. (Tuazon et al., 1981, Atkinson and Carter, 1984). It is used for some experimental runs as OH precursor.

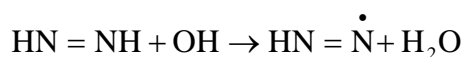
Initiation:



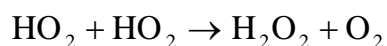
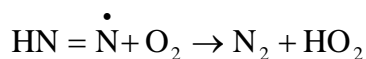
Propagation:



Termination:



Product formation:



4.2 OH radical production

In this study, the methyl nitrite is used as main OH precursor to provide radicals inside the chamber, in the presence of fluorescence lamps as solar simulator. In some experiments, the dark reaction of hydrazine with ozone is used to generate OH radicals in the chamber, in order to validate the experimental results with methyl nitrite.

A twin of gas containers is used to introduce methyl nitrite into the smog chamber (Figure 4.2 and 4.3). By this means, a fairly constant dosage of methyl nitrite could be achieved for almost 20 h (see Figure 4.4). The real OH concentration in the smog chamber is adjustable by the air flow rate and by the amount of methyl nitrite injected inside. During our experiments, the concentration of OH radical in smog chamber ranged from 2 to 28×10^6 molecule cm^{-3} .

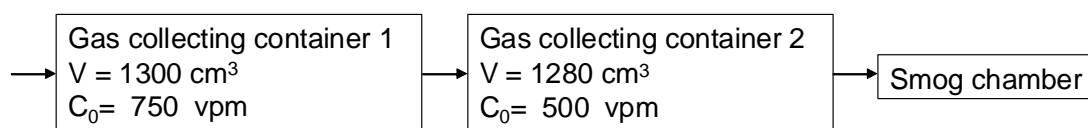


Figure 4.2 Schematic diagram of gas-collecting containers used to introduce methyl nitrite into the smog chamber

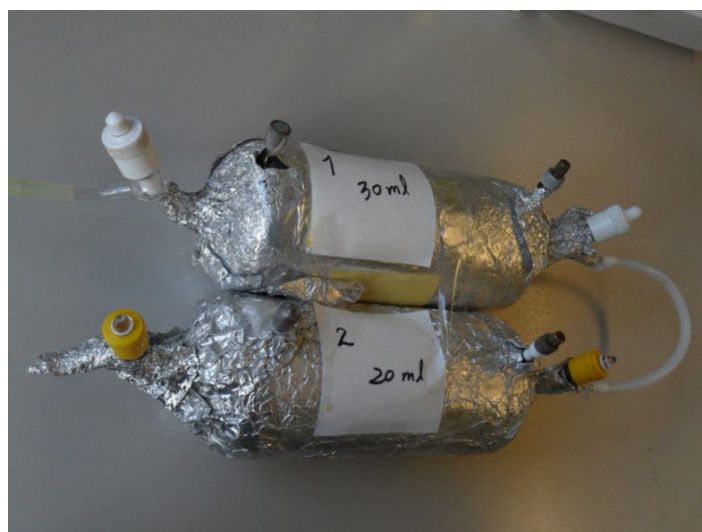


Figure 4.3 Photo of the twin of gas containers, used to introduce methyl nitrite into the smog chamber

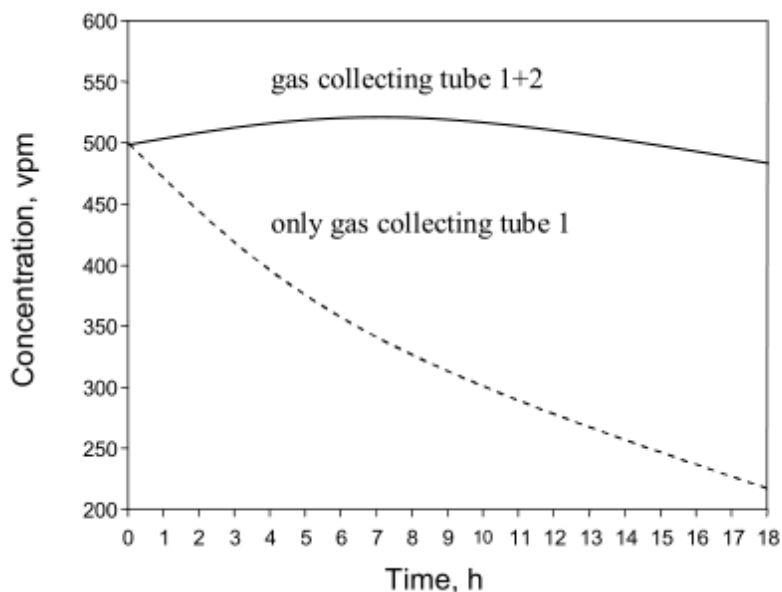


Figure 4.4 Comparison of the introduction of methyl nitrite into the smog chamber, using only one gas collecting container and twins' gas collecting container, respectively (Gavrillov, 2007)

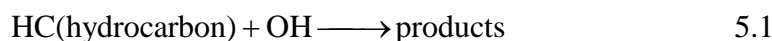
4.3 Determination of the OH radical concentration in the chamber

The absolute concentration of OH radicals could be measured by a sensitive absorption technique: Cavity ring-down spectroscopy (CRDS, Meijer et al., 1994, Cheskis et al., 1998), laser-induced fluorescence (LIF) combined with fluorescence assay with gas expansion (FAGE) (Schlosser et al., 2009), long-path Differential-Optical-Absorption Spectroscopy (DOAS, Hausmann et al., 1997, Fuchs et al., 2012), and recently developed Proton-Transfer-Reaction Mass Spectrometry (PTR-MS) measurement (Barnet et al., 2012). However, in most cases, the OH radical concentration is monitored via relative measurement. The steady-state methods were used in which the reaction goes on in competition with a reference reaction, involving a compound whose reactivity with OH is known from absolute measurements. In our experiments, three to four hydrocarbons were used as reference compounds to calculate the OH concentration in the chamber. As the air inside the chamber was sucked out for aerosol sampling, the dilution of the chamber was calculated by using an inert standard. The analysis of the inert standard and the hydrocarbons will be discussed in the following chapter.

5. Calculation of the apparent rate constant of the heterogeneous reaction of terbuthylazine with OH radicals

5.1 Calculation of the OH radical concentration from hydrocarbons

In the gas phase, the reaction of hydrocarbons with OH radicals follows a second order reaction as below:



Since OH concentration is almost constant, reaction 5.1 actually follows pseudo-first order kinetics. The concentration of a hydrocarbon during the experiment is then described as below:

$$\frac{dC_{\text{HC}}}{dt} = -k_{\text{OH}} \cdot C_{\text{OH}} \cdot C_{\text{HC}} - k_{\text{dilution}} \cdot C_{\text{HC}} \quad 5.2$$

C_{HC} is the hydrocarbon concentration, k_{OH} is the second order reaction rate constant for the reaction with OH radicals, C_{OH} is the OH radical concentration, k_{dilution} is the loss rate caused by dilution. Perfluorohexane (PFH) is considered to be chemically inert. In fact, the hydrocarbon concentrations are affected by the dilution process. Therefore, a standardization procedure is applied here to calculate the concentrations using perfluorohexane. For each single hydrocarbon, the peak area of the FID signal is normalized as shown below:

$$C_{\text{HC(norm),i}} = C_{\text{HC,i}} \cdot C_{\text{PFH,0}} / C_{\text{PFH,i}} \quad 5.3$$

$C_{\text{HC(norm),i}}$ is the normalized hydrocarbon peak area at time i , $C_{\text{HC,i}}$ is the peak area calculated from measurement at time i , $C_{\text{PFH,0}}$ is the initial measured FID peak area of perfluorohexane, $C_{\text{PFH,i}}$ is the measured FID peak area of perfluorohexane at time i . It is applicable to all reference hydrocarbons used for the smog chamber.

$$\ln\left(\frac{C_{\text{HC(norm)},t}}{C_{\text{HC(norm)},0}}\right) = -k_{\text{OH}} \cdot \int_0^t C_{\text{OH}} \cdot dt - k_{\text{other}} \cdot t \quad (\text{for constant } k_{\text{other}}) \quad 5.4$$

In Equation 5.4, $C_{\text{HC},t}$ and $C_{\text{HC},0}$ are the concentrations of the hydrocarbons at time t and initial time, respectively, k_{OH} is the second order reaction rate constant, C_{OH} is gas-phase OH radical concentration in the chamber, and k_{other} is the loss of hydrocarbons caused by other reasons, such as dilution or wall effect. A plot of the logarithm of the relative concentration of hydrocarbons at time t versus OH rate constants could yields the integral OH concentration as the slope.

The mean OH concentration in the chamber is obtained from the slope of the linear regression of integral OH concentration versus time. An average OH concentration value is taken from the calculation result for all hydrocarbons.

5.2 Calculation of the rate constant of terbuthylazine with OH radical

In this work, the semi-volatile compound is supposed to undergo a heterogeneous reaction with the OH radical. The reaction then happens with terbuthylazine in the adsorbed state.



It is supposed that the second order reaction 5.5 could also be described using pseudo-first-order kinetics (here the reactant refers to terbuthylazine which was adsorbed on the surface of the particles; the OH radicals exist in the gas phase (according to the Eley-Rideal mechanism)). The concentration of the aerosol-borne terbuthylazine is then described as:

$$\frac{dC_{\text{TBA(ads)}}}{dt} = -k_{\text{OH}} \cdot C_{\text{OH}} \cdot C_{\text{TBA(ads)}} \quad 5.6$$

A monoexponential depletion of terbuthylazine (TBA) was found for reaction 5.5. In this study, the precursor was continuously flushed into chamber by air stream, thus a constant OH concentration could be obtained in the chamber as Equation 5.7:

$$\ln\left(\frac{C_{\text{TBA(ads)},t}}{C_{\text{TBA(ads)},0}}\right) = -k_{\text{OH}} \cdot C_{\text{OH}} \cdot t \quad 5.7$$

6. Analysis of the compounds in the smog chamber

6.1 Analysis of the gas phase compounds

6.1.1 Introduction of the hydrocarbons into smog chamber

A gas storage container (Figure 6.1) was prepared as hydrocarbon storage source. Three or four hydrocarbons were used as reference compounds to calculate the OH level in the smog chamber. After mixing, 50 mL gas was taken out of the gas storage container and then introduced into the smog chamber through a leak-tight syringe (Figure 6.2). A ventilator inside the chamber was used to achieve a homogeneously dispersion.



Figure 6.1 Photo of the gas storage container



Figure 6.2 Photo of the syringe to inject gas into chamber

Perfluorohexane is used as dilution indicator due to its inert characteristics. As to the other hydrocarbons, the OH rate constants are known from the literature (Atkinson, 2003, shown in Table 6.2). The gas storage container needs to be renewed after every 10 experiments. The amount of hydrocarbons used for the gas storage container is shown in Table 6.1. Equation 6.1 and 6.2 are used to calculate the concentration of hydrocarbons in the smog chamber (60 ppb for each).

$$C_{\text{HC, chamber}} = \frac{V_{\text{HC, liquid}} \times \rho_{\text{HC, liquid}}}{M_{\text{HC}}} \times \frac{24\text{Lmol}^{-1}}{1.3\text{L}} \times \frac{50\text{mL}}{3200\text{L}} \quad 6.1$$

$$C_{\text{HC, chamber}} = \frac{m_{\text{HC, solid}}}{M_{\text{HC}}} \times \frac{24\text{Lmol}^{-1}}{1.3\text{L}} \times \frac{50\text{mL}}{3200\text{L}} \quad 6.2$$

$V_{\text{HC, liquid}}$ is the liquid volume for the gas storage container (μL), $\rho_{\text{HC, liquid}}$ is the density of liquid hydrocarbon (g cm^{-3}), M_{HC} is the molar mass of hydrocarbon (g mol^{-1}), $m_{\text{HC, solid}}$ is the measured mass for solid hydrocarbon (mg), the molar volume of ideal gas is 24L mol^{-1} , volume of the gas storage container is 1.3 L. During the experiment, 50 mL gas from the gas storage container was injected into the smog chamber.

Table 6.1 Amount of hydrocarbons corresponding to a concentration of 60 ppb in the smog chamber

Name of hydrocarbons	Source & purity	Amount for gas storage container
Perfluorohexane	Aldrich, 99%	45.0 μ L
n-Pentane	Grüssing GmbH, 99%	26.0 μ L
n-Heptane	Fluka AG, UV Spectroscopy grade, >260nm, >99%	32.5 μ L
2,2-Dimethylbutane	Janssen Chimica, 96%	24.5 μ L
2,2,4-Trimethylpentane	Janssen Chimica, 99+%	37.0 μ L
2,2,3,3-Tetramethylbutane	Sigma-Aldrich, \geq 94%	25.45 mg
Toluene	Carl Roth, RotiSolv HPLC, \geq 99.8%	23.5 μ L

Table 6.2 Rate constant for the reaction with OH radicals with reference compounds^a

Name of hydrocarbons	$10^{12} \times k$ ($\text{cm}^3 \text{ molecule}^{-1} \text{ s}^{-1}$) at 298 K	$10^{12} \times k$ ($\text{cm}^3 \text{ molecule}^{-1} \text{ s}^{-1}$) at 279.5 K	$10^{12} \times k$ ($\text{cm}^3 \text{ molecule}^{-1} \text{ s}^{-1}$) at 263 K
Perfluorohexane ^b	0	0	0
n-Pentane	3.80	^c	^c
n-Heptane	6.76	^c	^c
2,2-Dimethylbutane	2.23	1.87	1.56
2,2,4-Trimethylpentane	3.34	3.03	2.77
2,2,3,3-Tetramethylbutane	0.97	0.82	0.70
Toluene ^d	6.16	6.44	7.25

^a (Atkinson, 2003)

^b Nonreactive

^c These hydrocarbons were not used in those experiments

^d (Atkinson, 1986)

6.1.2 Sampling and analysis of the hydrocarbons from the chamber

A GC-FID (Simens Sicromat II), combined with a self-designed cold trap injector, was used for hydrocarbon on situ analysis (detailed information is described in chapter 3). The gas phase hydrocarbons are sampled automatically from the chamber every 30 minutes.

The sampling time for the gas phase was 2 minutes. 20 mL of each gas sample were cryofocussed onto the glass-lined tube in the cold trap during the cooling stage (-120°C in liquid nitrogen). A magnetic valve was used to switch the gas flow between the chamber and the carrier gas. The glass-lined tube was then heated to about 100 °C and the hydrocarbon samples were then injected into the FID column.

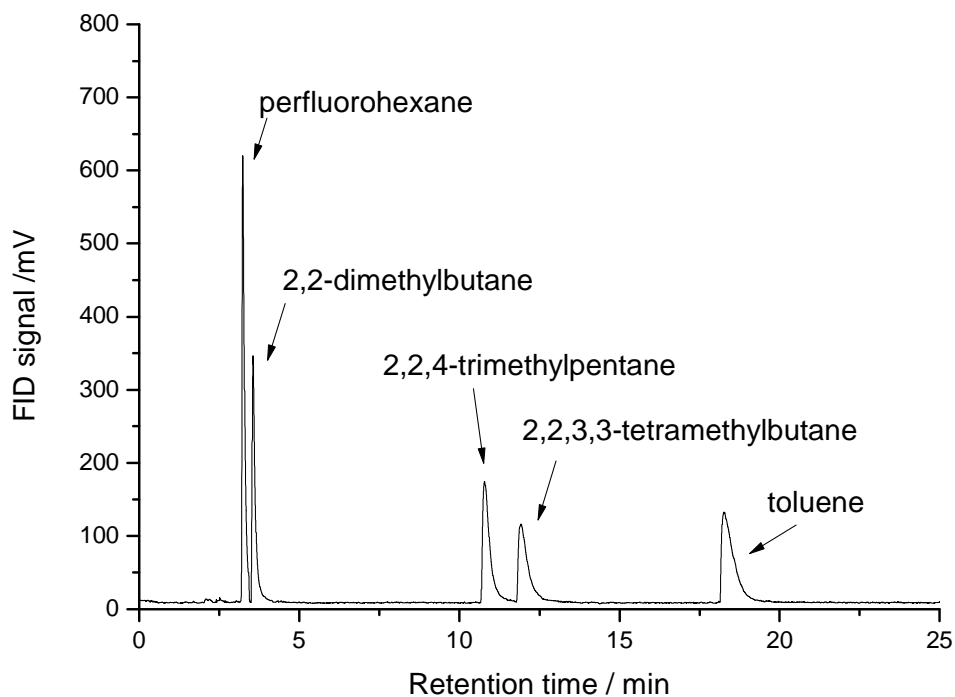


Figure 6.3 Chromatograms of hydrocarbons used in the chamber run

Figure 6.3 shows the GC-FID chromatogram of hydrocarbons. The peak areas are manually integrated.

6.2 Analysis of the particle-borne compounds

6.2.1 Aerosol injection into the chamber

A suspension containing coated particles was injected into the chamber before

hydrocarbons were injected. Around 37.0 mg aerosol materials were suspended in 50 mL double distilled water (dilution 1:1350). The suspension was then treated in an ultrasonic bath (Bandelin, Sonorex RK 255H) for 30 minutes in order to prevent agglomeration. Right after the preparation, the suspension was filled into a motor-driven syringe and sprayed by zero air through a nozzle (see chapter 2). In the subsequent glass cylinder, the aerosol droplets dry and form SiO₂ aerosol. The flow rate of the suspension is 22 mL/h and the air flow is 25 L/min.

6.2.2 Characterization of aerosol mass, size distribution and residence time

Figure 6.4 shows the size distribution of SiO₂ particles inside the chamber. There was a major peak of particles whose size was around 160 nm. According to the observed diameter of the SiO₂ spheres (159±2 nm, measured by SEM, see chapter 2), there is a great portion of single SiO₂ particles existing in the smog chamber (sharp peak at about 170 nm). The other peak around 240 nm and extending to more than 1000 nm consist of agglomerated particles. Those agglomerates are formed inside the storage flask of coated particles, and the ultrasonic process can not separate them very well.

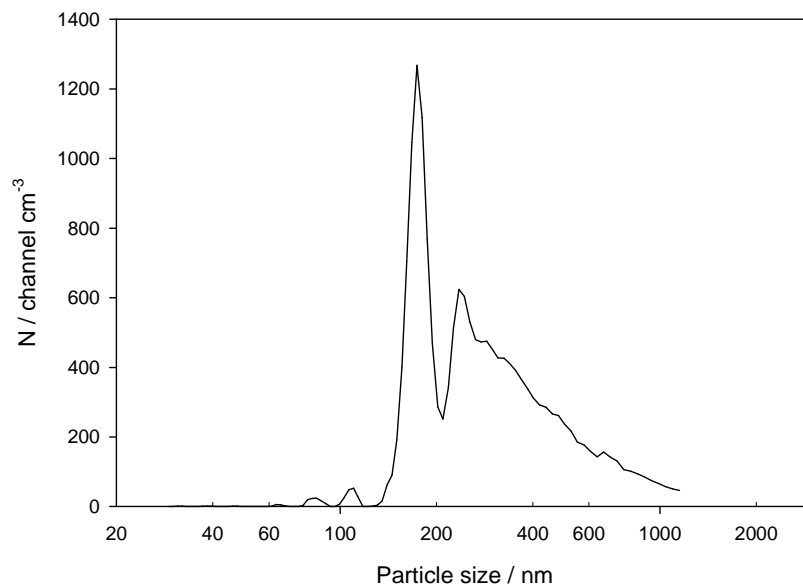


Figure 6.4 Size distribution of SiO₂ particles suspended in the chamber

To evaluate the residence time of particles limited mainly by sedimentation in the chamber, the particle concentrations were measured. The relation of sedimentation rate with particle concentrations is described in Equation 6.3.

$$C_p = C_{p,0} e^{-k_{\text{sedi}} t} \quad 6.3$$

C_p is the accumulative particle concentration at time t , $C_{p,0}$ is the initial particle concentration, k_{sedi} is the sedimentation rate of particles. Figure 6.5 shows a measurement of C_p versus time. The residence time of the particles in the chamber could then be calculated from the slope of the linear regression of the semilogarithmic plot:

$$\tau_{\text{particle}} = 1/k_{\text{sedi}} = 24.3 \text{ h} \quad 6.4$$

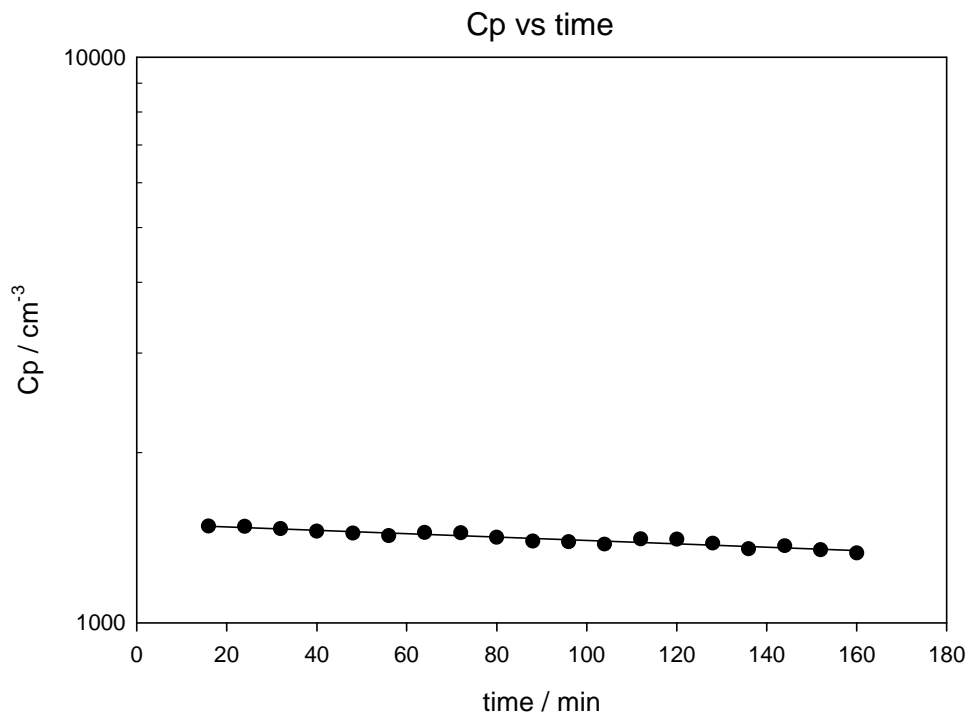


Figure 6.5 Concentration of suspended particles versus time t

6.3 Sampling and extraction of the aerosol samples

The aerosols were collected on a FTPE filter through a sampling device (see chapter 2). Four filters were regarded as weighing filters (one under dark conditions, three filters during the experiment). They were kept below a discharging unit (β radiation) for ≈ 24 hours. The aerosol mass was then determined by a microbalance (Sartorius, type SC02). 4-6 filters, treated as analysis filters, were put inside a 2 mL vial with 1 mL dichloromethane, then put in an ultrasonic bath (Sonorex RK 255H) for 5 minutes for extraction. The aerosol suspension was then removed by a centrifuge (Heraeus,

Biofuge A, 6000 U/min) for 3 minutes. The final solution was analyzed by gas chromatography with a flame ionization detector, employing on-column injection. Two injections were made to check the reproducibility. Figure 6.6 shows a FID chromatogram from the filter extract.

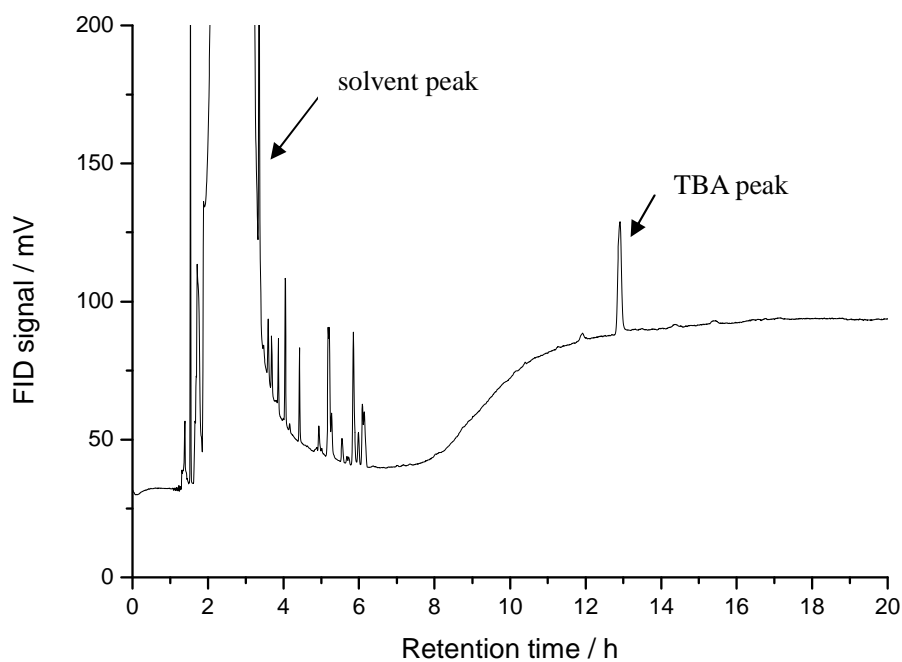


Figure 6.6 FID Chromatogram of the extract from a filter sample. (extraction from filter 0 for experiment D111115 at 25°C)

7. Results and discussion

In this chapter, the results of different experiments will be described and discussed. All experiments were performed with freshly prepared aerosol suspensions (see chapter 6 for detailed information). Two days were required for each single experiment: during the first day, the gas samples were analyzed continuously during the aerosol chamber run, and the filter samples were taken; during the second day, all filter samples were analyzed (both the weighing filters and the analysis filters).

Temperature and relative humidity of the air inside the chamber were monitored continuously during the experiment at two measuring sites in the chamber: one was close to the chamber wall on the top; the other was right in the middle of the chamber (see Figure 7.1).

The concentrations of ozone and nitrogen oxides inside the chamber were also monitored continuously.

The experiments were performed in the smog chamber at three different temperature levels (25 °C, 6.5 °C and -10 °C) in order to determine the temperature dependence of such heterogeneous reactions.

7.1 Monitoring of temperature and relative humidity in the smog chamber

There were two temperature sensors inside the smog chamber in order to monitor the temperature at different positions inside the chamber. The sensor close to the top of chamber measured the air temperature and humidity. The sensor in the middle of chamber measured the air temperature at the central axis of the chamber. Figure 7.1 shows the position of the temperature sensors.

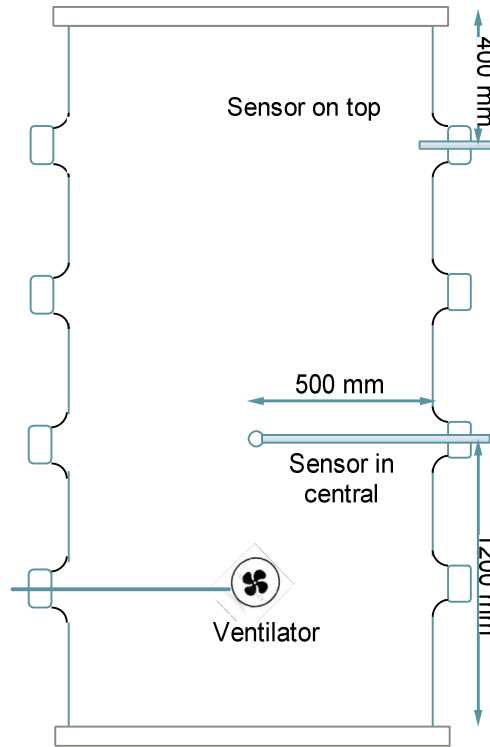


Figure 7.1 Illustration of the position of the temperature sensors in the chamber (the sensor on top of the chamber is close to the wall and 400 mm from the top, the sensor in the middle of the chamber is 130 mm from the chamber wall at a height of 1200 mm from the bottom of chamber)

7.1.1 Results of the temperature and relative humidity measurement at 25 °C

Figure 7.2 shows the data of temperatures observed by both sensors during a dark experiment. It can be seen from the data that the air temperature close to the chamber walls are greatly affected by temperature within the room (the steps in the curve for T_{TOP} and relative humidity (R.H.) are given by the digital resolution). The temperature control of the cooling was switched off during this run. The convex decrease of humidity is caused by the dilution of chamber air due to the filter sampling process and the synchronous dry air supply to the chamber.

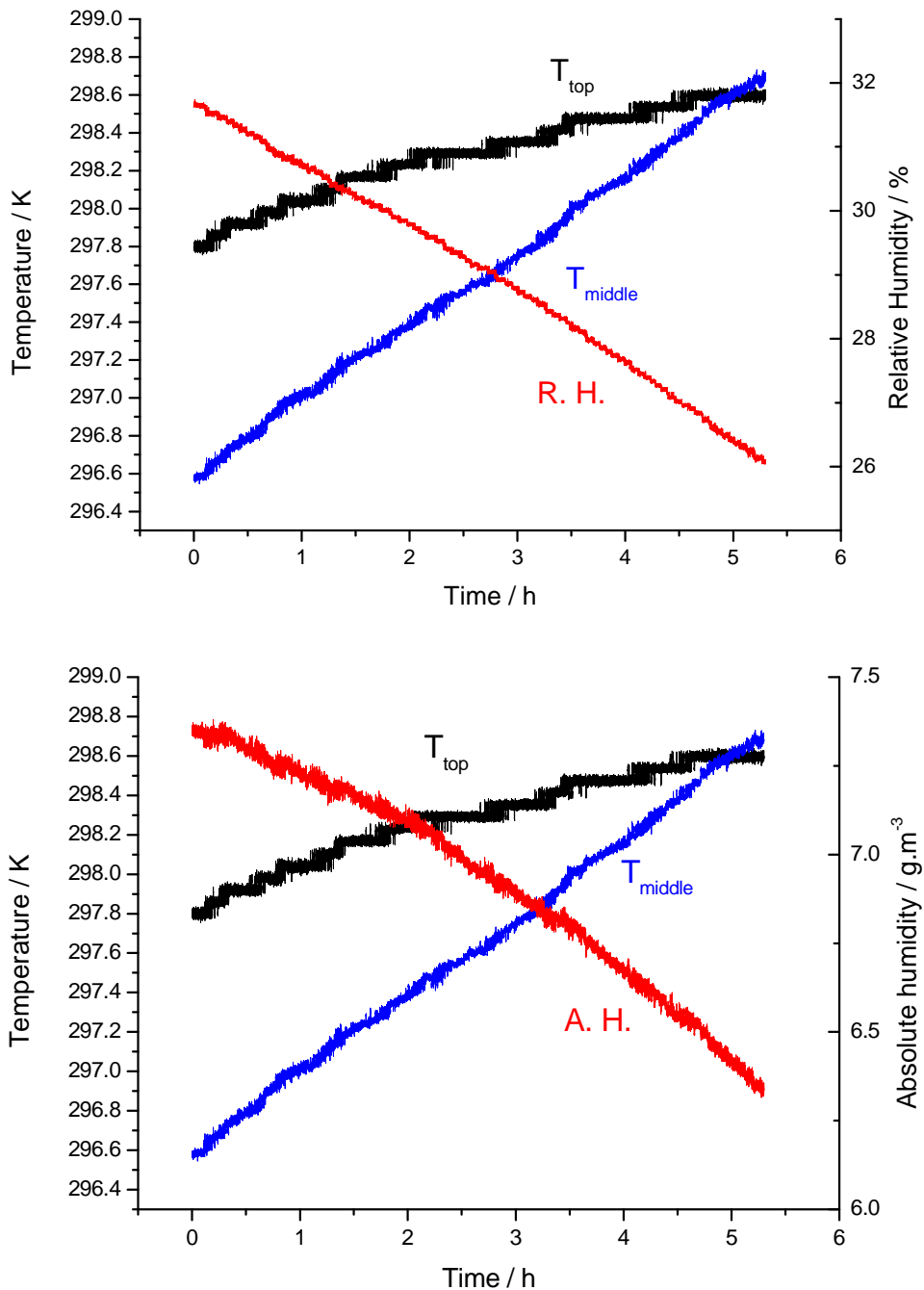


Figure 7.2 Performance of temperature and humidity in the smog chamber at 25°C during a run in darkness (D111105). T_{top} and T_{middle} represent the temperature obtained by sensor on top and middle of the smog chamber, respectively; R. H. and A. H. mean the relative and absolute humidity.

During a typical experiment with photochemical production of OH radicals by UV radiation from the solar simulator, the air in the middle of the chamber was heated up, leading to an increase of the temperature by $\Delta T=7.8$ °C (see Figure 7.3).

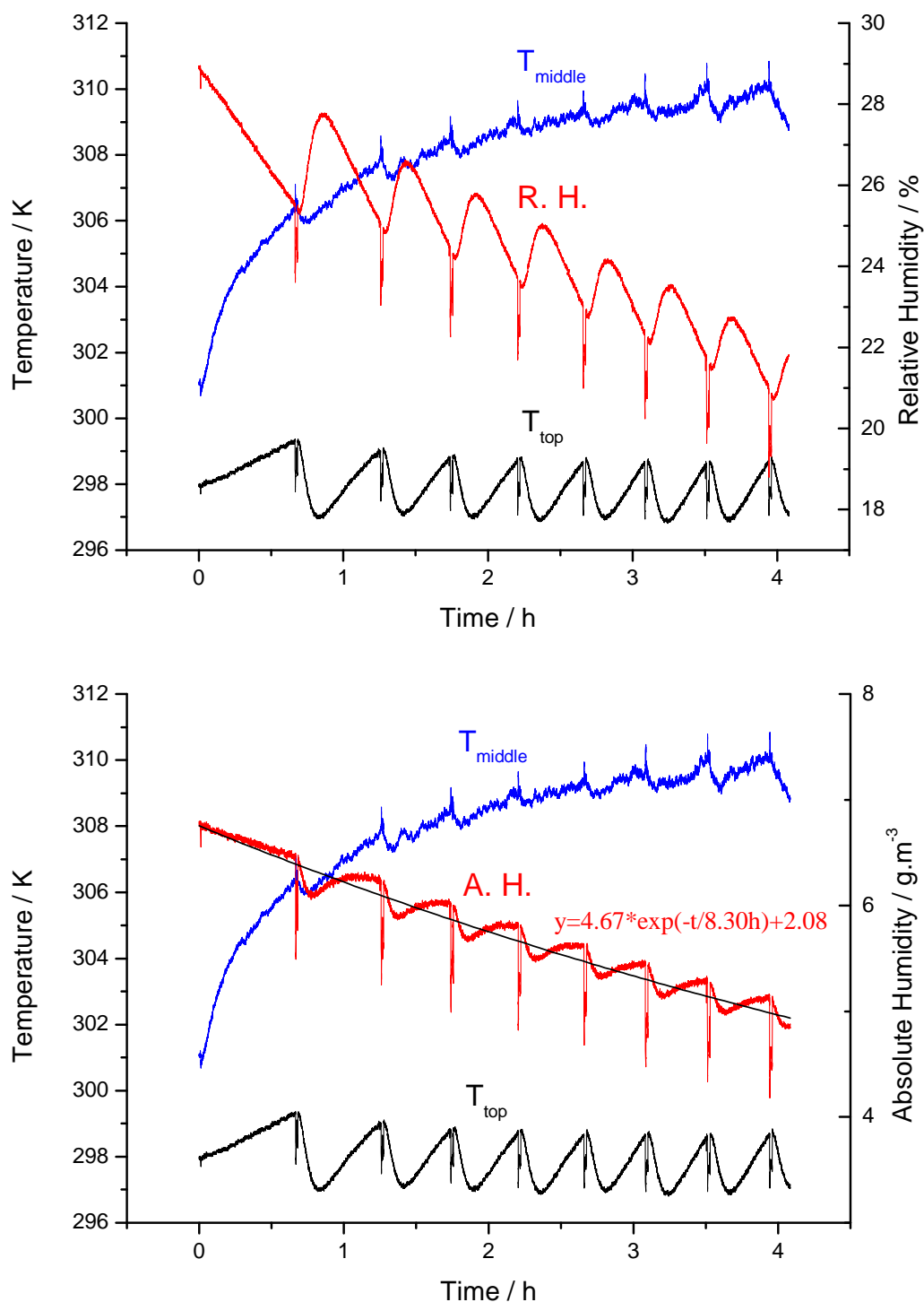


Figure 7.3 Performance of temperature and relative humidity in the smog chamber at 25°C during an experimental run of the OH reaction with the solar simulator on (D111005). T_{top} and T_{middle} represent the temperature obtained by sensor on top and middle of the smog chamber, respectively. R. H. and A. H. mean the relative and absolute humidity. The sharp spikes are an electronic interference from the relay of the temperature control.

7.1.2 Results of the temperature and relative humidity measurement at 6.5 °C and -10°C

In this work, in order to investigate the impact of temperature on the chemical kinetics, the chamber experiments were also performed at 6.5 °C and -10 °C. Figure 7.4 and Figure 7.5 show the temperature trend inside the chamber at 6.5 °C and -10 °C, respectively. At lower temperature, the change of the temperature was small compared to the results at 25 °C. It was caused by different cooling power set: lower cooling power at 25°C and high at other lower temperature.

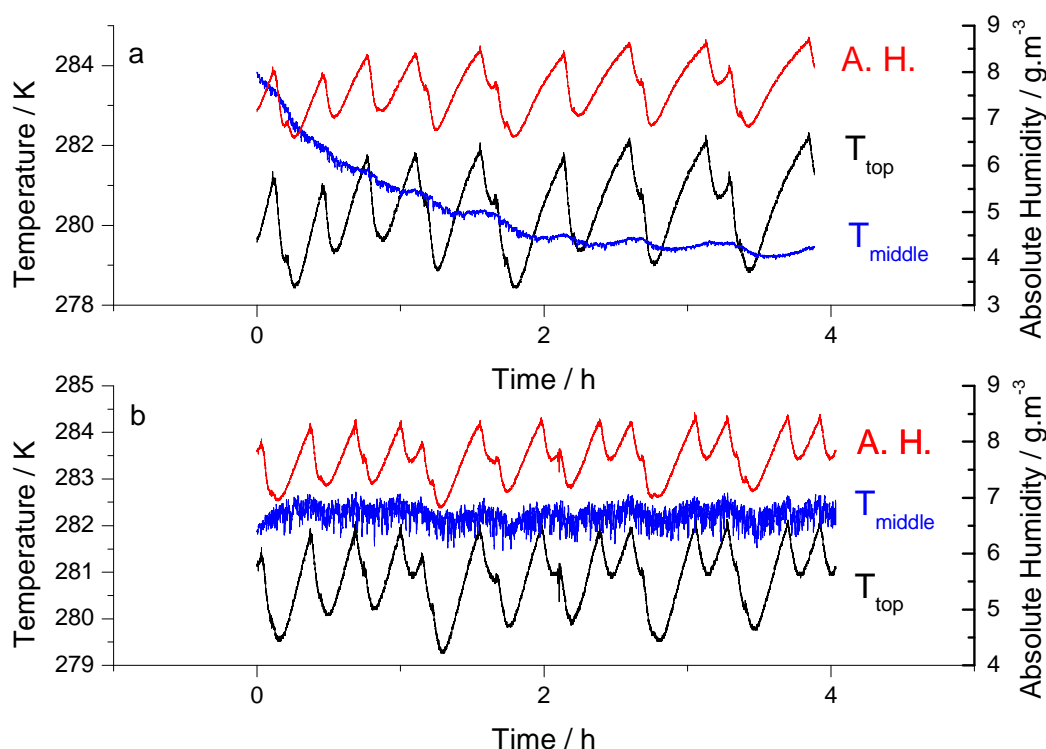


Figure 7.4 Temperature and absolute humidity in the smog chamber at 6.5 °C during an experimental run under dark conditions, where the temperature control was about to reach equilibrium (D121226) (a) and with the solar simulator switched on (D120113) (b). T_{top} and T_{middle} represent the temperature obtained by sensor on top and middle of the smog chamber, respectively. A. H. means the absolute humidity.

In Figure 7.4, graph (a) and graph (b) show the temperature and absolute humidity result at 6.5 °C in darkness and in the presence of light, respectively. The noises of temperature on top of the chamber was strongly influenced by the cooling system. However, the air temperature in the middle of the chamber has no big variations.

($\Delta T=1.7$ °C in darkness and $\Delta T=0.6$ °C with solar simulator on). At 6.5 °C, the humidity remains constant during the whole experimental run, because the air inside the chamber is saturated with water vapour and the filter sampling process does not have any influence on the humidity change.

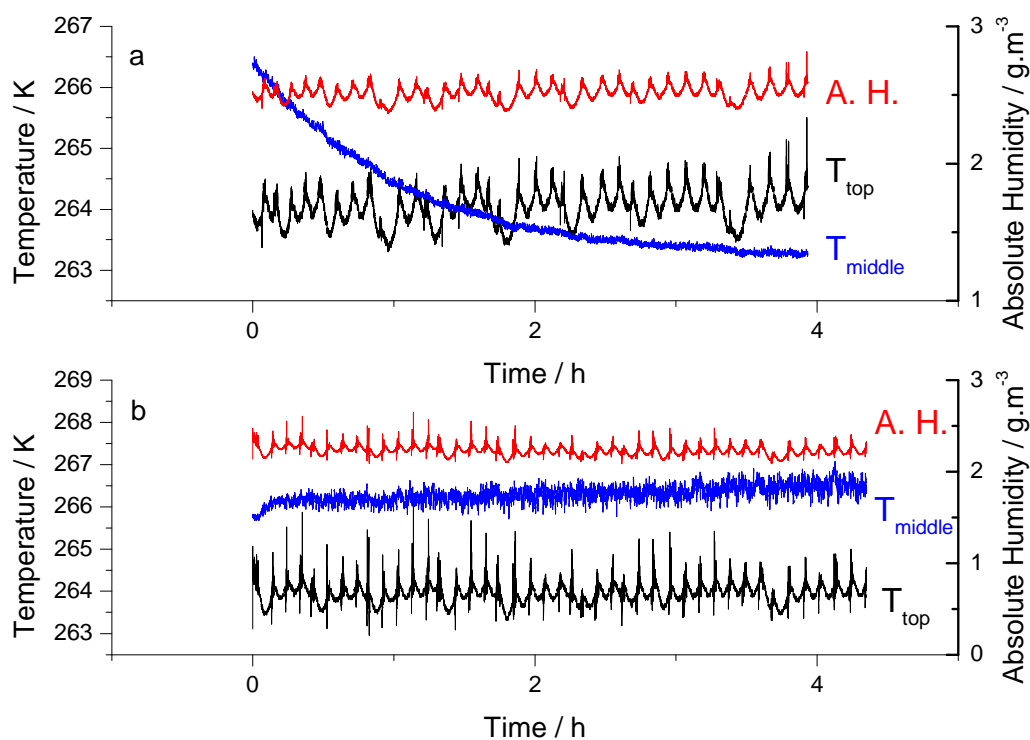


Figure 7.5 Temperatures and absolute humidity in the smog chamber at -10 °C during an experimental run under dark conditions (D120415) (a) and with solar simulator on (D120405) (b)

Figure 7.5 graph (a) and graph (b) show the temperatures and relative humidity observed at -10 °C in darkness and in the presence of light, respectively. The higher frequency of spikes is caused by the strong cooling power. When the solar simulator is switched on, the air temperature in the middle of the chamber remains stable during the experimental period ($\Delta T=0.7$ °C with solar simulator on). At -10°C there is ice on the wall of chamber, so the absolute humidity is lower than that at 6.5°C.

7.2 Measurements of the concentrations of ozone and nitrogen oxides in the smog chamber

The concentrations of NO_x and ozone are monitored in the chamber by the ozone

analyzer and the NO_x analyzer (detailed description in chapter 3). The concentrations of NO_x and ozone can be regarded as reference data.

7.2.1 Results of NO_x and ozone measurement in the experiment at 25°C

During an experiment with methyl nitrite as OH precursor, the levels of NO_x and ozone increased after the solar simulator was switched on (shown in Figure 7.6). Within the experimental period of around 5 hours, the ozone level builds up to 450 ppb.

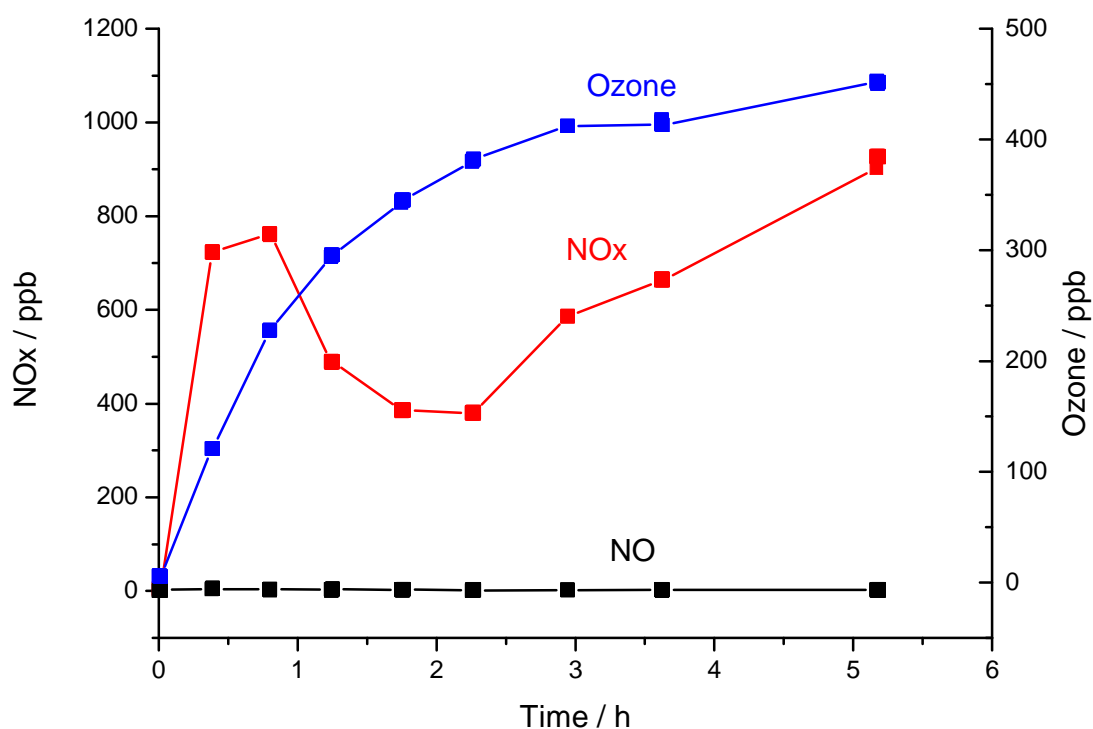


Figure 7.6 Ozone and NO_x monitoring during an experiment with OH radical in the smog chamber at 25 °C (solar simulator on, D111012)

According to the Leighton ratio (Leighton, 1961), the photo stationary state Φ is defined as:

$$\phi = \frac{J_{\text{NO}_2} [\text{NO}_2]}{k_{(\text{NO}+\text{O}_3)} [\text{NO}] [\text{O}_3]} \quad 7.1$$

J_{NO_2} is the photolysis frequency of NO₂, in s⁻¹; $k_{(\text{NO}+\text{O}_3)}$ is the temperature-dependent rate constant for the reaction between NO and O₃, in ppb⁻¹ s⁻¹ (Junkermann et al., 1989). A steady state is assumed, and $\Phi \Rightarrow 1$ (Rohrer et al., 1998),

then the ratio of $\frac{[\text{NO}_2]}{[\text{NO}][\text{O}_3]}$ should be a constant during one experiment with stable irradiation (constant= $k_{(\text{NO}+\text{O}_3)}/J_{\text{NO}_2}$). Figure 7.7 shows the ratio of $\frac{[\text{NO}_2]}{[\text{NO}][\text{O}_3]}$ during an experimental run at 25 °C, the value of this ratio is 0.64 ± 0.28 , in ppb^{-1} .

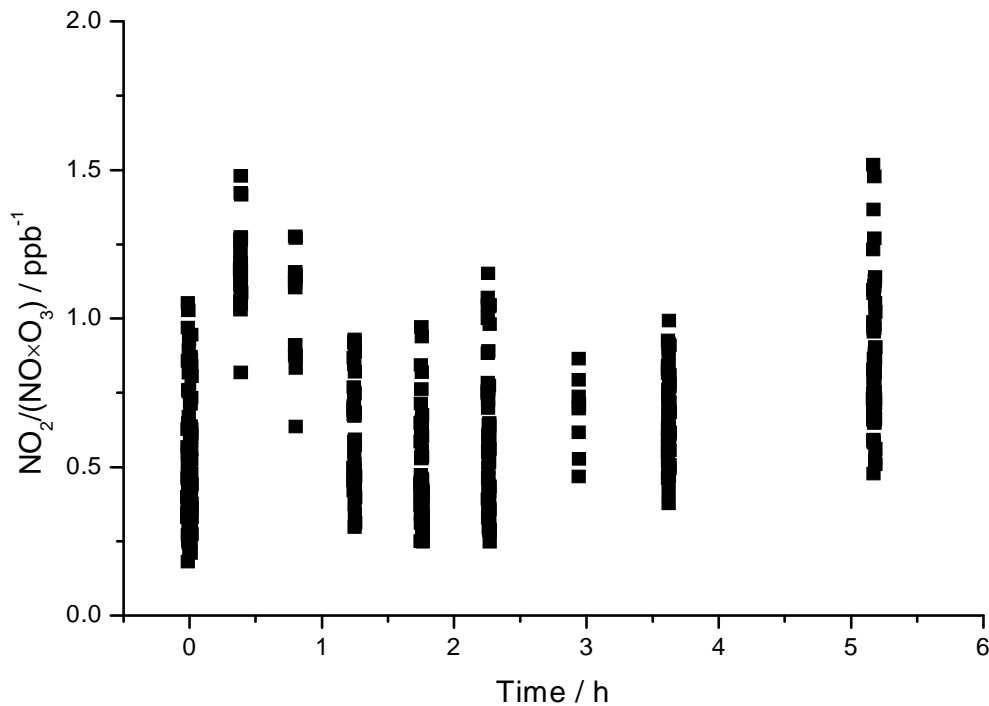


Figure 7.7 The ratio $[\text{NO}_2] / ([\text{NO}]\times[\text{O}_3])$ during an experiment with OH radicals in the smog chamber at 25 °C (solar simulator on, D111012)

7.2.2 Results of NO_x and ozone measurement in the experiment at 6.5 °C

The monitoring result of NO_x and ozone during an experiment at 6.5 °C (Figure 7.8) also showed an accumulation of the concentrations of NO_x and ozone with time.

The sum of the concentration levels of NO_x and ozone were a bit smaller than at 25°C (approximately 140 ppb NO_x and 70 ppb ozone after 4 hours).

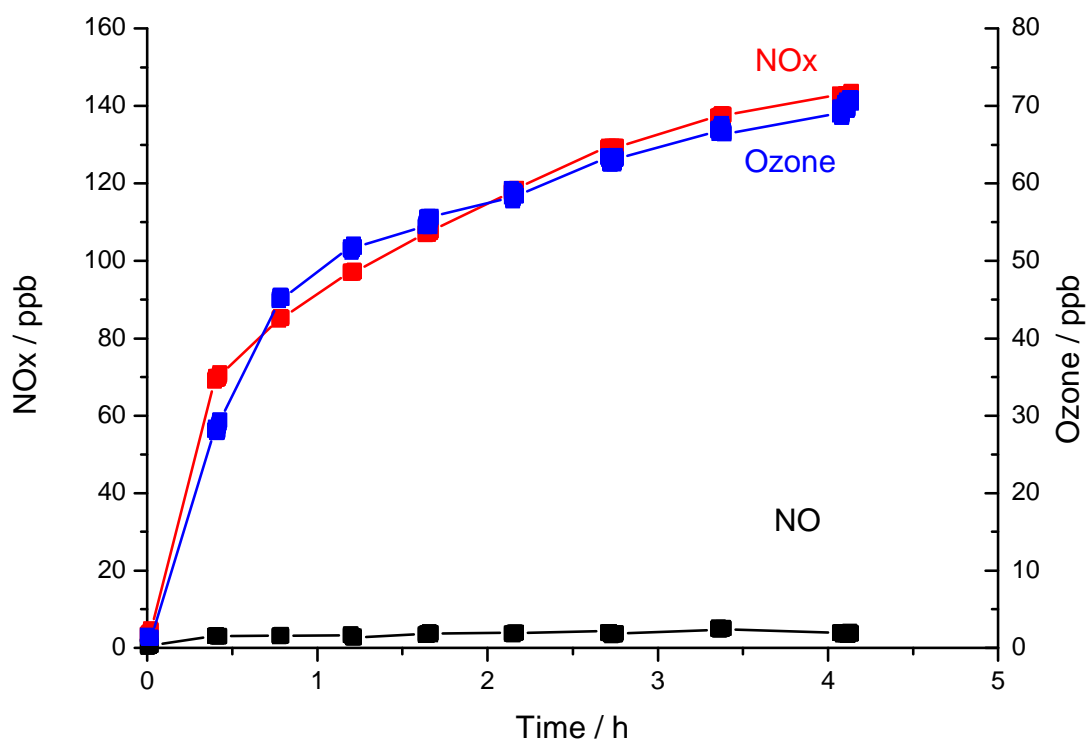


Figure 7.8 Ozone and NO_x monitored during an experiment with OH radicals in the smog chamber at 6.5 °C (solar simulator on, D120113). The Leighton ratio is 0.56±0.10, in ppb⁻¹(see Figure 7.10).

7.2.3 Results of NO_x and ozone measurement in the experiment at -10 °C

Figure 7.9 shows the levels of NO_x and ozone in the smog chamber at -10°C. The NO_x concentration builds up in a fashion similar to the experiments 25°C and 6.5°C, together with a slight increase of the NO level. The ozone level has an increase from 0 to approximately 70 ppb, and then decreases slowly as the photochemistry goes on. One possible explanation is that there could be ice particles on the chamber wall, which could cause the ozone depletion in existence of light and NO_x (Tolbert et al., 1988). However, it is not clear to what degree such reactions could happen in the smog chamber.

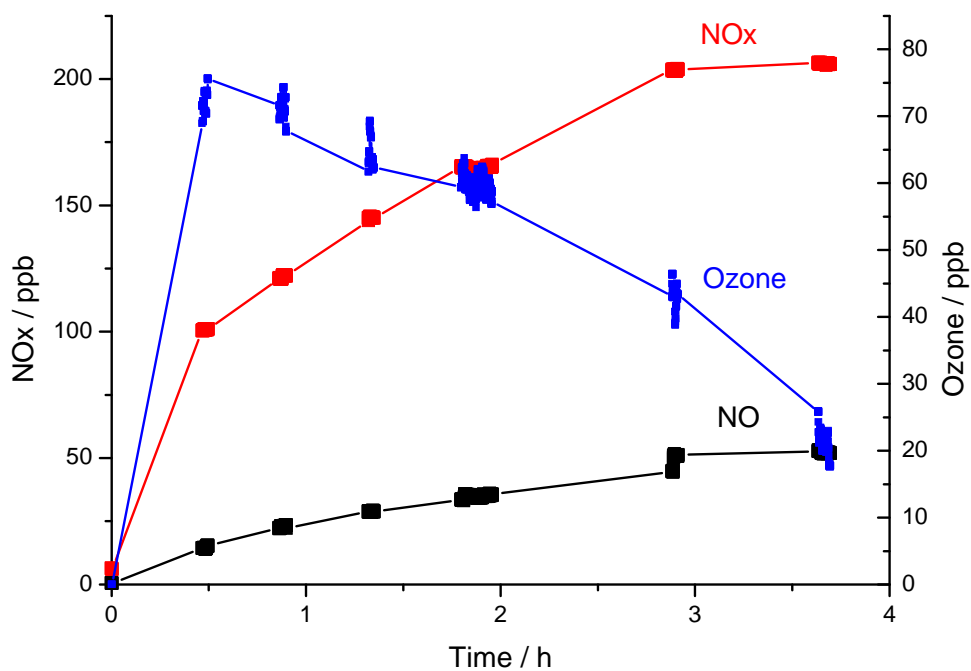


Figure 7.9 Ozone and NO_x monitored during an experiment with OH radicals in smog chamber at -10 °C (solar simulator on, D110405). The Leighton ratio is 0.10±0.04, in ppb⁻¹(see Figure 7.10).

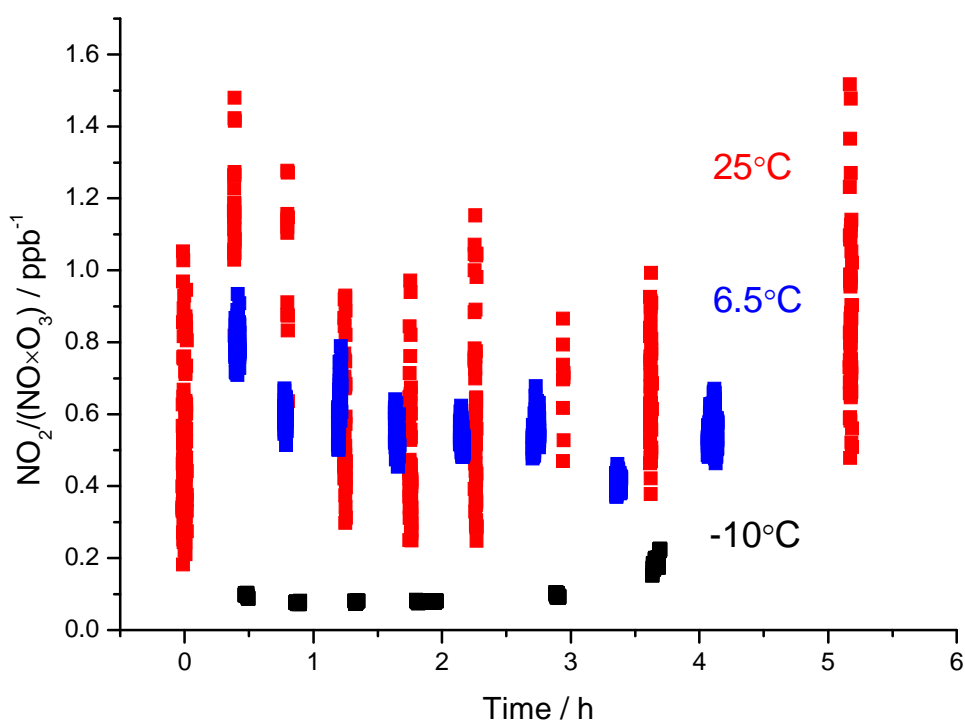


Figure 7.10 The ratio of $\frac{[\text{NO}_2]}{[\text{NO}]\times[\text{O}_3]}$ during experiments with OH radicals in the smog chamber at 25 °C, 6.5 °C, and -10 °C, respectively

The ratios of $\frac{[\text{NO}_2]}{[\text{NO}][\text{O}_3]}$ at different temperatures are given in Figure 7.10. From the

figure, it can be seen that this value remains constant for experiments at different temperatures. The ratios are similar at 25 °C and 6.5 °C (0.64 ± 0.28 at 25 °C and 0.56 ± 0.10 at 6.5 °C, in ppb^{-1}), which are higher than the value at -10 °C (0.10 ± 0.04 , in ppb^{-1}). This could be caused by the slower reaction of ozone with NO at lower temperatures (Clough and Thrush, 1966).

7.3 Coating efficiency during the aerosol coating process

After the SiO_2 particles were coated by terbuthylazine, the initial mass fractions on the dispersed aerosol were determined. The results showed a value of $F_{\text{TBA}}=0.045$. Compared to the initial mass fraction of TBA on aerosol ($F_{\text{TBA},0}=0.047$), the loss during the coating procedure is about 4%. It is probably caused by the adsorption of TBA on the surface of glass walls in the aerosol generator.

7.4 Summary of experiments in the smog chamber

Experiments were performed in the smog chamber at 25°C, -6.5°C, and -10°C. At each temperature, there were blank experiments in which the light or OH precursor were absent in order to understand the impact of the smog chamber on the reactions. The duration of all experiments and OH precursors used are summarized in the following tables.

Table 7.1 Summary of aerosol smog chamber experiments performed at 25 °C

Experiments No.	OH precursor	τ_{aero} (h)	$C_{\text{OH}} (\times 10^6 \text{ cm}^{-3})$	$k_{\text{OH}} (\times 10^{-12} \text{ cm}^3 \text{ s}^{-1})$	$k_{\text{obs}}^1 (\times 10^{-5} \text{ s}^{-1})$	Comments
D110831	none	8.20±0.13	0.89±0.35	8.8±0.76	0.79±0.31	
D110902	methyl nitrite	7.71±0.29	5.74±0.31	4.5±1.3	2.56±0.73	
D110905	methyl nitrite	8.33±0.69	22.4±1.3	2.88±0.03	6.44±0.37	
D110907	none (dark)	/	/	/	/	perfusor error
D110909	methyl nitrite	/	/	/	/	perfusor error
D110915	methyl nitrite	8.55±0.10	2.59±0.17	6.71±0.89	1.74±0.30	
D110919	methyl nitrite	7.25±0.16	22.9±1.2	2.37±0.33	5.44±0.82	
D110927	methyl nitrite	10.42±0.87	15.89±0.68	3.49±0.13	5.55±0.36	
D110929	methyl nitrite	7.17±0.87	22.47±0.85	2.95±0.90	6.6±2.0	
D111005	methyl nitrite	9.80±0.87	12.93±0.25	3.91±0.30	5.05±0.41	
D111010	methyl nitrite	6.58±0.35	27.39±0.69	2.66±0.30	7.28±0.85	
D111012	methyl nitrite	7.14±0.51	15.35±0.54	3.51±0.27	5.38±0.48	
D111105	none (dark)	16.39±2.69	0.86±1.36	/	1.9±3.7	
D111107	none	9.26±0.09	1.41±0.63	11.03±2.0	1.6±1.2	
D111112	methyl nitrite	/	/	/	/	perfusor error
D111115	methyl nitrite	9.17±0.25	15.08±0.21	3.49±0.23	5.27±0.36	
D111208	N ₂ H ₄ +O ₃	/	/	/	/	perfusor error
D111211	N ₂ H ₄ +O ₃	/	/	/	/	perfusor error
D111215	N ₂ H ₄ +O ₃	/	/	/	/	perfusor error
D111216	N ₂ H ₄ +O ₃	/	/	/	/	perfusor error
D111222	N ₂ H ₄ +O ₃	/	/	/	/	perfusor error
D111223	N ₂ H ₄ +O ₃	/	/	/	/	perfusor error
D120423	N ₂ H ₄ +O ₃	11.63±1.08	34.06±1.66	0.84±0.07	2.86±0.30	

* dark experiment

Table 7.2 Summary of aerosol smog chamber experiments performed on Aerosil 200 particles at 25°C

Experiments No.	OH precursor	τ_{aero} (h)	$C_{\text{OH}} (\times 10^6 \text{ cm}^{-3})$	$k_{\text{OH}} (\times 10^{-12} \text{ cm}^3 \text{ s}^{-1})$	$k_{\text{obs}}^{\text{I}} (\times 10^{-5} \text{ s}^{-1})$	Comments
D111020	none (dark)	16.67±2.78	0.59±0.38	/	0.72±0.48	
D111023	none (dark)	9.35±0.79	1.12±0.22	18.1±1.3	2.03±0.55	
D111028	methyl nitrite	12.20±0.30	7.52±0.56	13.16±0.87	9.9±1.0	
D111121	methyl nitrite	13.51±2.56	11.89±0.75	11.5±1.2	13.7±1.7	
D111206	methyl nitrite	13.33±0.53	18.57±0.73	8.09±0.18	15.03±0.70	

* dark experiment

Table 7.3 Summary of aerosol smog chamber experiments performed at 6.5 °C

Experiments No.	OH precursor	τ_{aero} (h)	$C_{\text{OH}} (\times 10^6 \text{ cm}^{-3})$	$k_{\text{OH}} (\times 10^{-12} \text{ cm}^3 \text{ s}^{-1})$	$k_{\text{obs}}^{\text{I}} (\times 10^{-5} \text{ s}^{-1})$	Comments
D111226	none (dark)	12.50±1.56	0.53±1.16	/	0.88±1.9	
D111228	none	11.49±0.92	0.81±0.80	13.5±1.4	1.09±1.28	
D111230	methyl nitrite	11.76±0.83	16.73±1.11	3.23±0.22	5.40±0.56	
D120102	methyl nitrite	11.11±1.23	20.17±0.42	2.69±0.22	5.43±0.47	
D120104	methyl nitrite	13.16±0.52	18.92±1.51	2.77±0.29	5.24±0.73	
D120106	methyl nitrite	17.24±2.08	20.52±7.00	2.60±0.27	5.34±0.60	
D120109	methyl nitrite	13.16±0.87	16.26±0.65	3.35±0.41	5.45±0.71	
D120111	methyl nitrite	10.64±1.02	14.10±0.67	2.70±0.51	3.81±0.75	
D120113	methyl nitrite	12.20±1.19	24.72±0.99	2.43±0.09	6.00±0.35	
D120116	N ₂ H ₄ +O ₃	13.33±2.67	2.34±0.55	6.35±1.81	1.49±0.70	
D120121	N ₂ H ₄ +O ₃	/	/	/	/	cancelled
D120425	N ₂ H ₄ +O ₃	11.49±0.26	2.94±0.34	5.39±0.77	1.59±0.36	

* dark experiment

Table 7.4 Summary of aerosol smog chamber experiments performed at -10 °C

Experiments No.	OH precursor	τ_{aero} (h)	C_{OH} ($10^6 \times \text{cm}^{-3}$)	k_{OH} ($\times 10^{-12} \text{cm}^3 \text{s}^{-1}$)	k_{obs} ($\times 10^{-5} \text{s}^{-1}$)	Comments
D120415	none (dark)	8.77±0.69	0.5±1.1	/	0.6±1.2	
D120325	none	9.09±0.83	0.78±0.29	6.2±1.5	0.48±0.21	
D120327	methyl nitrite	16.67±2.78	8.60±0.83	2.77±0.48	2.38±0.47	
D120329	methyl nitrite	9.09±0.83	2.85±0.33	5.0±1.4	1.43±0.43	
D120401	methyl nitrite	10.87±1.06	14.88±0.55	1.75±0.07	2.60±0.14	
D120403	methyl nitrite	10.75±0.35	18.22±0.48	1.77±0.07	3.23±0.15	
D120405	methyl nitrite	12.05±0.73	14.30±0.25	1.83±0.40	2.62±0.57	
D120408	methyl nitrite	11.11±1.23	10.10±0.32	2.37±0.51	2.40±0.52	
D120410	methyl nitrite	10.87±0.35	23.06±1.59	1.57±0.27	3.62±0.66	
D120427	N ₂ H ₄ +O ₃	8.31±0.44	5.09±0.23	3.59±0.49	1.83±0.26	

* dark experiment

7.5 Heterogeneous degradation of terbuthylazine on SiO₂ at 25 °C.

The duration of each chamber experiment was typically two days. During the first day, after the hydrocarbons and aerosol suspension were injected into the smog chamber and well mixed, the OH precursor was injected into the chamber. The reaction started when the solar simulator was turned on. The concentrations of hydrocarbons were measured every 30 minutes (see chapter 2) and the filter samples were taken. During the second day, the extracts of the analysis filters were evaluated by GC-FID and the weighing filter were measured (for detailed information see chapter 6).

7.5.1 Calculation of the OH concentration

According to Equation 5.4 (see above), the integral OH concentration at time t , can be calculated based on the measured FID peak areas of each hydrocarbon. A plot of the integral OH concentration versus time t , yields the OH concentration in the chamber as the slope. Figure 7.11 shows the integral OH concentration derived from different hydrocarbons in experiment D111012 versus time.

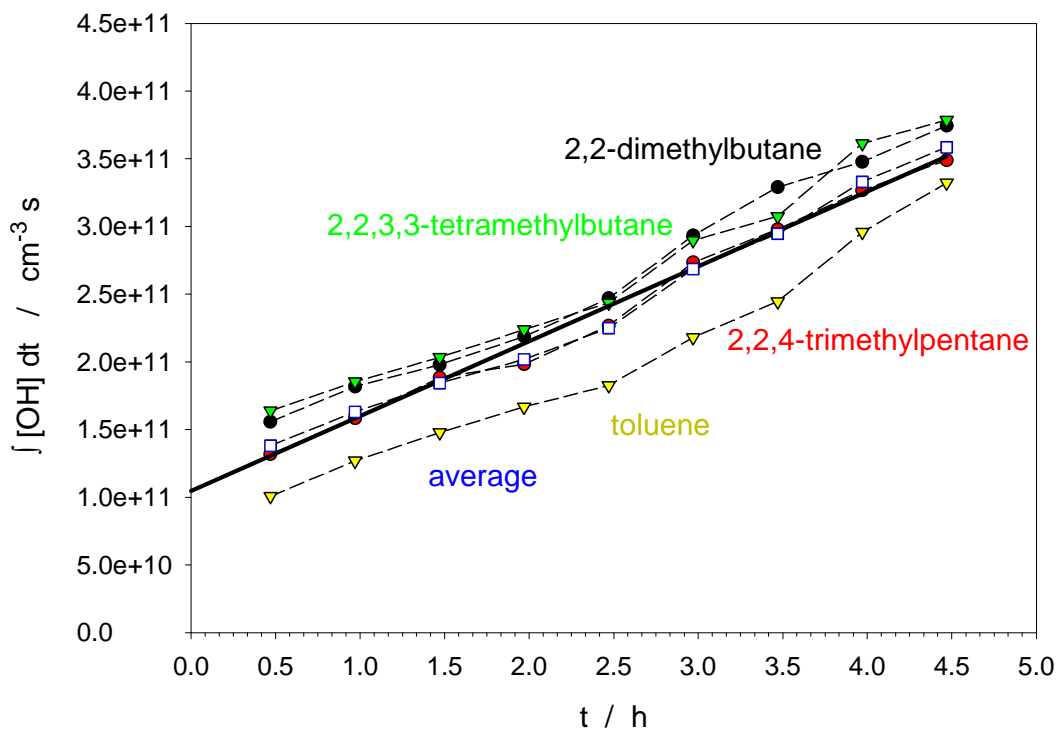


Figure 7.11 Integral OH concentration derived from different hydrocarbons in experiment D111012 versus time. The linear regression shown in this figure yields the mean OH concentration from the slope $((15.35 \pm 0.54) \times 10^6 \text{ cm}^{-3})$

In Figure 7.11, the intercept of the regression line does not start from zero. This phenomenon could be explained by the experimental procedure to generate OH radical in the smog chamber: Methyl nitrite was injected continuously about 2-3 minutes before the solar simulator was turned on. When the methyl nitrite started to photolyse to generate OH radicals, the OH concentration could reach a high level instantaneously and then fall to a constant value (as shown in Figure 7.12). The deviation of intercept of the hydrocarbons in Figure 7.11 is caused by a lack of time resolution and the amount of consumed hydrocarbons by this "pulse OH radical" based on their reaction rate with OH radicals.

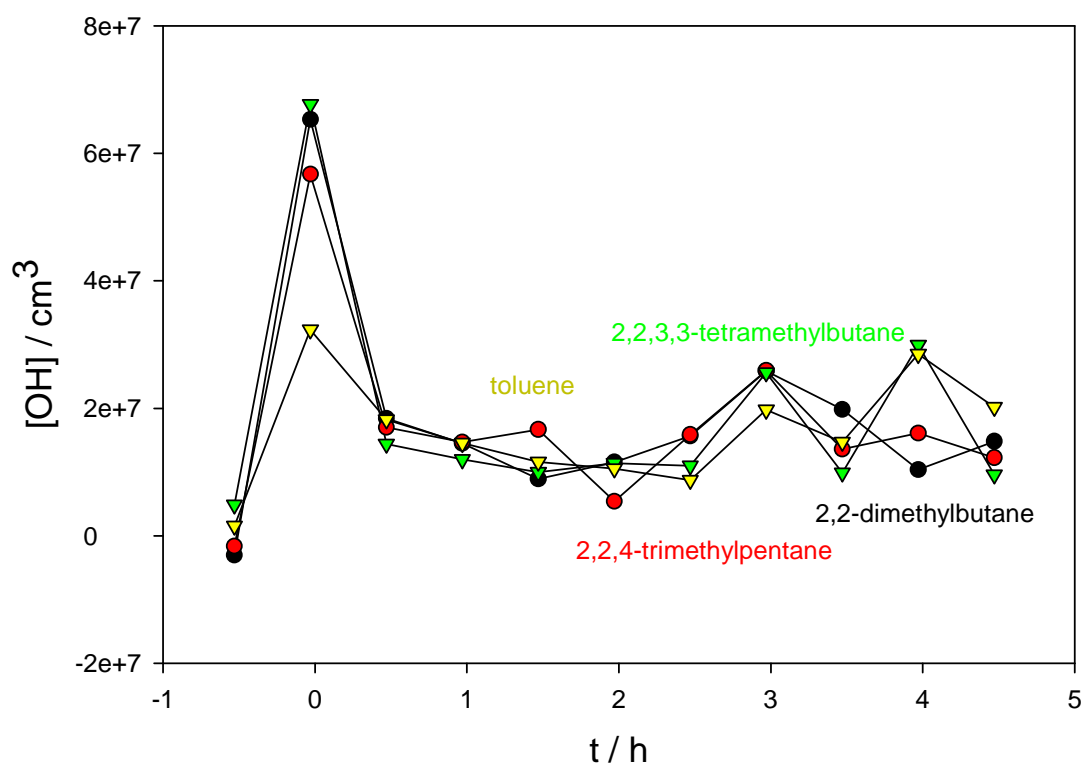


Figure 7.12 OH concentration calculated from different hydrocarbons versus time (D111012). The high level of OH concentration was caused by the methyl nitrite accumulated before the light was turned on.

7.5.2 Calculation of the TBA concentration adsorbed on aerosol

To calculate the aerosol concentration C_{Ae} , the filter weight and sampled air volume are needed:

$$C_{Ae} = m_f / V_f \quad 7.2$$

where C_{Ae} is the aerosol concentration in the smog chamber, in mg cm^{-3} , m_f is the weight of aerosol masses collected on the filter, in mg, and V_f is the volume of air which was taken for the filter sampling, in cm^{-3} .

At the same time, the dilution factor should also be evaluated for every filter sample. It can be calculated from the filter sampling volume and the chamber volume

$$d_v = \exp(V_{\text{dil}} / 3200) \quad 7.3$$

Where d_v is the dilution factor and V_{dil} is the sampling volume which caused the dilution, in L. The chamber volume is 3200 L. The interpolated aerosol concentration C'_{Ae} (mg cm^{-3}) can thus be corrected by d_v :

$$C'_{\text{Ae}} = C_{\text{Ae}} \cdot d_v \quad 7.4$$

During each experiment, 4 weighing filters were taken to determine the aerosol concentration at different time. As the aerosol concentration follows an exponential decay, the aerosol mass of the analysis filter samples can be interpolated from the weighing filter results. Since the aerosol concentration decreases exponentially, the analysis samples, which are taken between the aerosol concentration samples, can be interpolated to obtain the aerosol mass for the other filter samples. A plot of the logarithm of the aerosol concentration at time t versus corresponding time yields the initial aerosol concentration $C_{\text{Ae},0}$ from the intercept and the time constant b of the aerosol deposition from the slope. From Equation 7.3, the aerosol concentrations C_{Ae} for time t can be calculated for every experiment. Figure 7.13 shows the trend of aerosol concentration for the weighing filters and the interpolated analysis filter during an experimental run.

$$C_{\text{Ae}} = C_{\text{Ae},0} \cdot e^{-b \cdot t} \quad 7.5$$

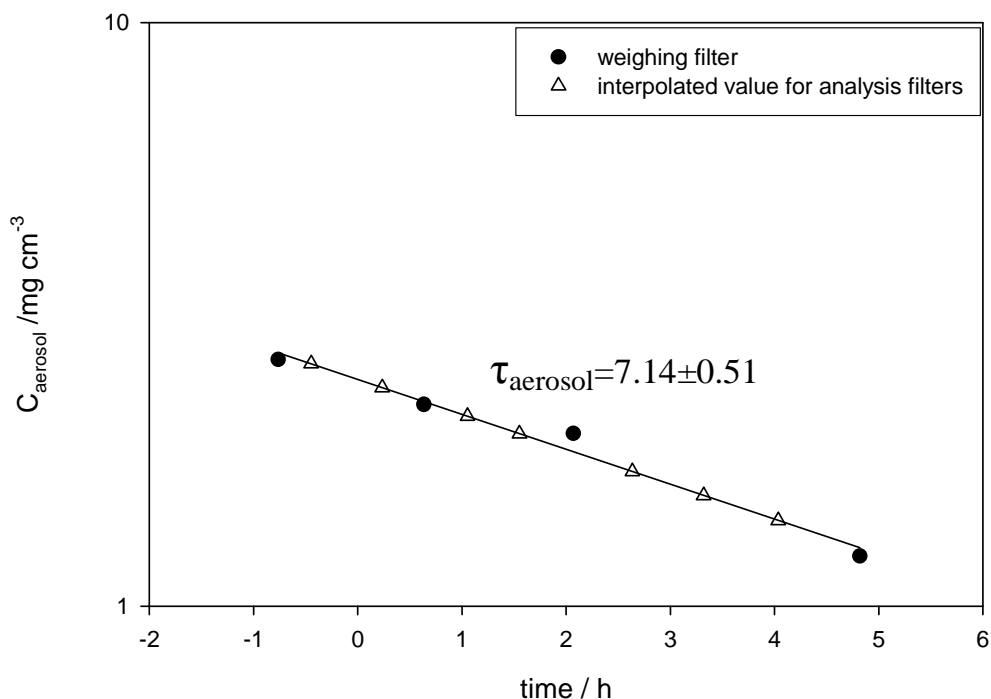


Figure 7.13 Decrease of the aerosol mass concentration of SiO_2 coated with terbuthylazine in an experiment at 25°C (D111012). The solid circles represent the measured results for weighing filters; the hollow triangles show the interpolated aerosol concentrations from Equation 7.5

7.5.3 Determination of the OH rate constant of terbuthylazine

The filter extracts were analyzed by GC-FID (detailed description see chapter 3). As only the relative concentrations were needed to calculate the rate constant of terbuthylazine (Equation 6.7), the peak areas from the FID peaks were used for the calculation.

$$\ln\left(\frac{C_{\text{TBA(ads),t}}}{C_{\text{TBA(ads),0}}}\right) = -k_{\text{OH}} \cdot C_{\text{OH}} \cdot t \quad 5.7$$

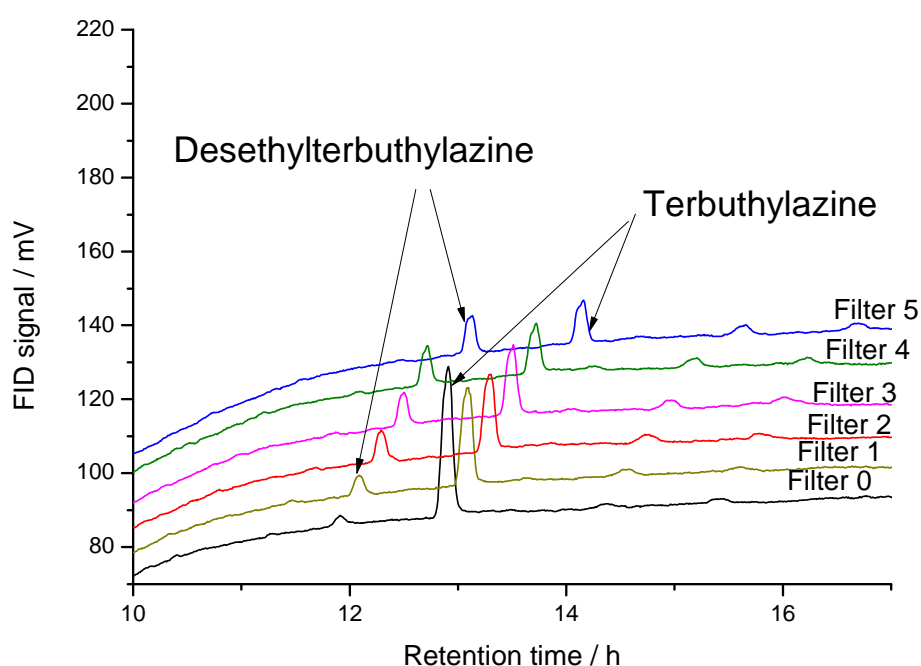


Figure 7.14 Chromatograms of experiment D111012. The lines represent filter samples taken at different exposure times of the coated aerosol particles.

Following Equation 5.7, a plot of the logarithm of the terbuthylazine concentration on the aerosols versus the integral OH concentration is made and the linear regression yields the rate constant k_{OH} from the slope.

In Figure 7.14, there is a sharp decrease of the terbuthylazine peak from filter 0 to filter 1; Figure 7.15 clearly shows the trend. This phenomenon is caused by the high instantaneous OH radical concentration when the solar simulator was switched on (as shown in Figure 7.12). After that, the terbuthylazine on the aerosol reacts continuously with OH radicals at a constant level, and the decay rate could be

calculated based on the known OH radical concentration. So in this study, the experimental point of filter 0 in the darkness is excluded, and only the remaining filters are used for the calculation.

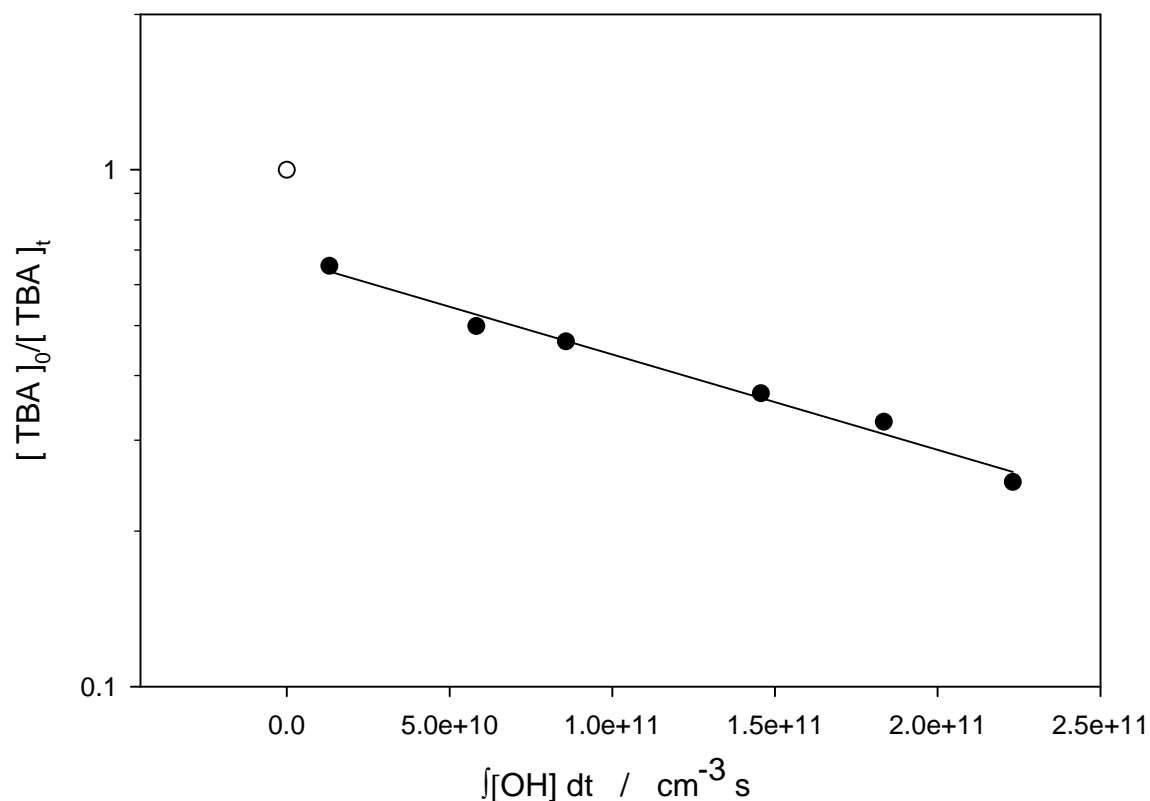


Figure 7.15 Relative ratios of TBA on the aerosol versus integral OH concentration in an experiment at 25°C (D111012). The solid points represent the filter sample data points after the solar simulator was switched on; the hollow point represents the first analysis filter (F₀), which was excluded from the regression as discussed above.

From Figure 7.15, the rate constant for the reaction of terbuthylazine with OH radicals is obtained from the slope of linear regression of the semilogarithmic diagram. The k_{OH} in experiment D111012 is calculated to be $(4.25 \pm 0.27) \times 10^{-12} \text{ cm}^3 \text{ s}^{-1}$.

7.5.4 Application of the Langmuir-Hinshelwood and Eley-Rideal mechanisms on the experimental data at 25°C

Table 7.1 (see Chapter 7.4) gives a summary of the results of the experimental runs performed at 25°C. The data of experiment D111105 (dark) follows the same calculation procedure. All experimental results have been corrected by the $k_{\text{obs}}^{\text{I}}$ value

obtained in the dark experiment, and the k_{OH} was recalculated after the correction. Considering the small surface area of self-synthesized SiO_2 particles, a possible loss path of terbuthylazine in the dark might be desorption from the aerosol.

A plot of the second order rate constants versus the OH concentrations (Figure 7.16) shows that k_{OH} decreases with increasing OH radical concentration. As described in chapter 3, the Langmuir-Hinshelwood mechanism could explain this negative dependence of k_{OH} on OH concentration (see Equation 3.8 in chapter 3).

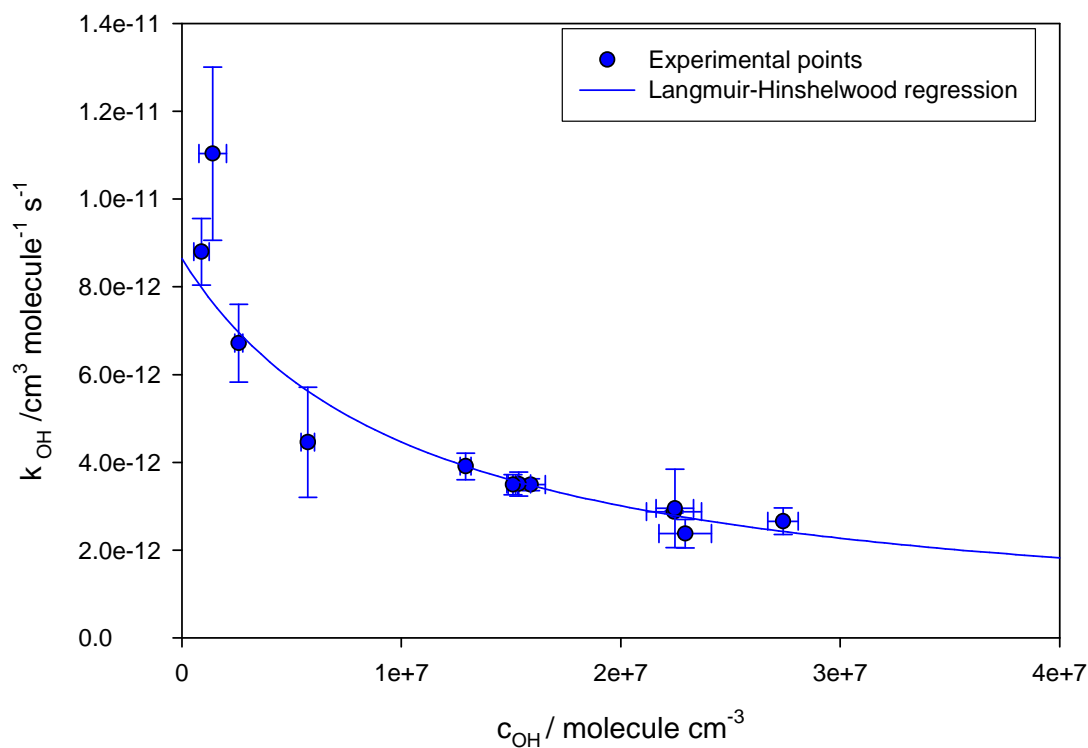


Figure 7.16 Experimental second order rate constant, k_{OH} , versus OH radical concentration in the heterogeneous reaction of OH radicals with terbuthylazine adsorbed on home-made SiO_2 particles in the LOTASC chamber

The experimental pseudo-first-order rate constant, k_{obs}^1 , was also plotted versus the OH radical concentration (see Figure 7.17), in order to verify this hypothesis. As can be seen in Figure 7.17, the k_{obs}^1 values approach a plateau at higher OH concentrations, which shows a likelihood of following the Langmuir-Hinshelwood mechanism.

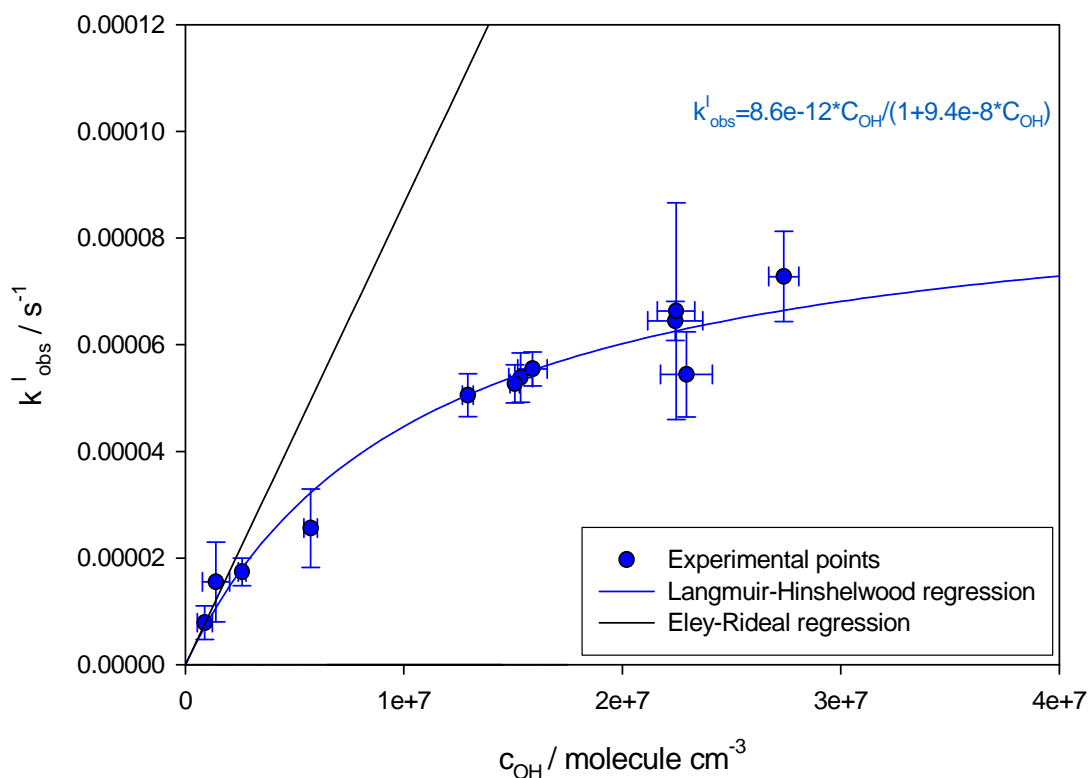


Figure 7.17 Experimental pseudo-first-order rate constant k_{obs}^I versus the OH radical concentration in the heterogeneous reaction of OH radicals with terbuthylazine, adsorbed on home-made SiO₂ particles in the LOTASC chamber

In order to obtain the K_{OH} and k_{max}^I values for the Langmuir-Hinshelwood mechanism (Equation 3.8) from a simple linear regression, the reciprocal of k_{OH} was employed. Equation 7.6 is derived from Equation 3.8:

$$\frac{1}{k_{OH}} = \frac{1}{k_{max}^I \cdot K_{OH}} + \frac{C_{OH}}{k_{max}^I} \quad 7.6$$

Such a regression of $1/k_{OH}$ versus C_{OH} then yields $1/k_{max}^I$ as slope and $1/(k_{max}^I \cdot K_{OH})$ as intercept. For those experiments at 25°C with the self-synthesized SiO₂ particles as carrier particles, Figure 7.18 shows the linear regression according to Equation 7.6. The parameters for the Langmuir-Hinshelwood regression are derived as below:

$$K_{OH} = (9.4 \pm 1.6) \times 10^{-7} \text{ cm}^3 \text{ molecule}^{-1}$$

$$k_{max}^I = (9.24 \pm 0.84) \times 10^{-5} \text{ s}^{-1}$$

From these results and according to the Langmuir-Hinshelwood mechanism (see

Equation 3.7), a regression line was generated in Figure 7.17 and the fitting equation is shown as below:

$$k_{\text{obs}}^{\text{I}} = 8.6 \times 10^{-12} C_{\text{OH}} / (1 + 9.4 \times 10^{-8} C_{\text{OH}}) \quad 7.7$$

The data points in Figure 7.17 could also be used to obtain the parameters of the Eley-Rideal mechanism. The limiting slope for the Eley-Rideal mechanism should be taken at $C_{\text{OH}} \rightarrow 0$, and then based on Equation 3.8 the $k_{\text{OH (Eley-Rideal)}}$ equals to $k_{\text{max}}^{\text{I}} \times K_{\text{OH}}$ and yields $(8.6 \pm 1.2) \times 10^{-12} \text{ cm}^3 \text{ molecule}^{-1} \text{ s}^{-1}$.

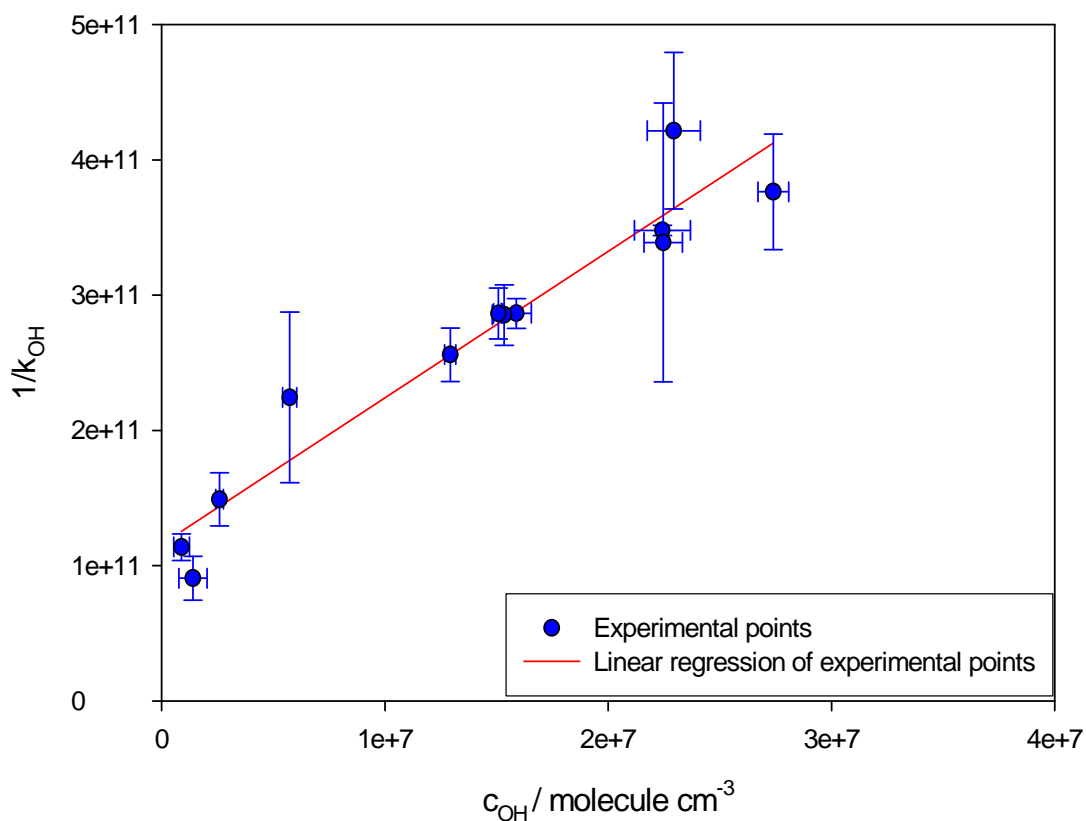


Figure 7.18 Reciprocal of k_{OH} versus OH radical concentration for all experiments.

7.5.5 Comparison with experiments of the OH radical reaction of terbuthylazine adsorbed on Aerosil 200 particles

In order to understand the impact of the characteristics of the particulate matter, the results from this work were compared with previous work by Palm et al. (1997). To

understand to what extent the systematic error (volume of chamber, methodology of aerosol injection, different OH precursors, etc.) would affect the results, several experiments with Aerosil 200 particles, coated with terbuthylazine, were performed in the LOTASC chamber. Figure 7.19 shows the experimental second order rate constant k_{OH} versus OH concentration on SiO_2 particles in this work, the results from Palm et al. (1997), and the results on Aerosil 200 in this work, respectively. It can be clearly seen that the Aerosil 200 experimental points correspond to the previous data quite well.

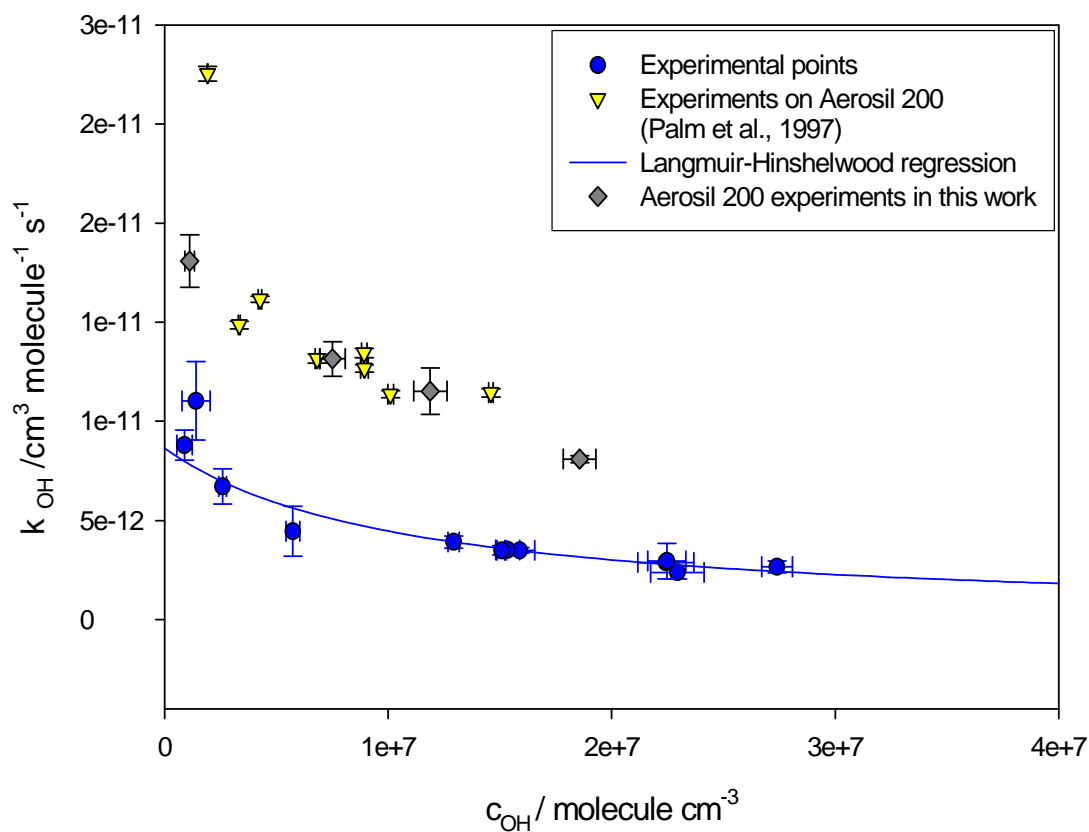


Figure 7.19 Experimental second order rate constant k_{OH} versus the OH radical concentration in the heterogeneous reaction of OH radicals with terbuthylazine adsorbed on home-made SiO_2 particles in the LOTASC chamber

Figure 7.20 gives the results of the pseudo-first-order rate constant (k_{obs}^I) versus the OH radical concentration on Aerosil 200 particles and on the self-synthesized particles. From the previous results from Palm et al. (1997), the data points give a good linear regression, which indicates a domination of the Eley-Rideal mechanism.

The repetitive experiments with Aerosil 200 as carrier particles in this work also meet the fitting line. However, combined with experimental results on Aerosil 200 from this work, an estimation of Langmuir-Hinshelwood mechanism can also be made as below:

$$K_{\text{OH (Aerosil 200)}}=(8.4\pm 1.4)\times 10^{-8}\text{ cm}^3\text{ molecule}^{-1}$$

$$k_{\text{max (Aerosil 200)}}^{\text{I}}=(2.65\pm 0.34)\times 10^{-4}\text{ s}^{-1}$$

The experimental data on SiO₂ particles follows the Langmuir-Hinshelwood mechanism very well. Even more so, based on the above discussions, the limiting value for low OH concentrations gives a second order rate constant based on the Eley-Rideal mechanism of $k_{\text{max}}^{\text{I}} \times k_{\text{OH}}$. For the results on SiO₂ particles, $k_{\text{OH (Eley-Rideal)}}$ is $(8.6\pm 1.2)\times 10^{-12}\text{ cm}^3\text{ molecule}^{-1}\text{ s}^{-1}$, in reasonable agreement with the previous results on Aerosil 200: $k_{\text{OH}}=(1.1\pm 0.2)\times 10^{-11}\text{ cm}^3\text{ molecule}^{-1}\text{ s}^{-1}$ (Palm et al., 1997). In this point, the heterogeneous reaction of gas phase OH radicals with aerosol-borne terbuthylazine follows similar kinetics on both Aerosil 200 particles and self-synthesized SiO₂ particles. The appearance of either a Langmuir-Hinshelwood or an Eley-Rideal mechanism is possibly caused by the characteristics of particles: The specific surface area of Aerosil 200 is $200\text{ m}^2\text{ g}^{-1}$, which is much higher than that of the self-synthesized SiO₂ particles (calculated to be $17\text{ m}^2/\text{g}$, see chapter 2), in this case, the OH radical can be adsorbed sufficiently around the terbuthylazine molecule on the Aerosil 200 surface. The OH radicals could react freely with the adsorbed terbuthylazine on the aerosol surface, like the gas phase reactions. That could explain the domination of Eley-Rideal mechanism for experiments on Aerosil 200.

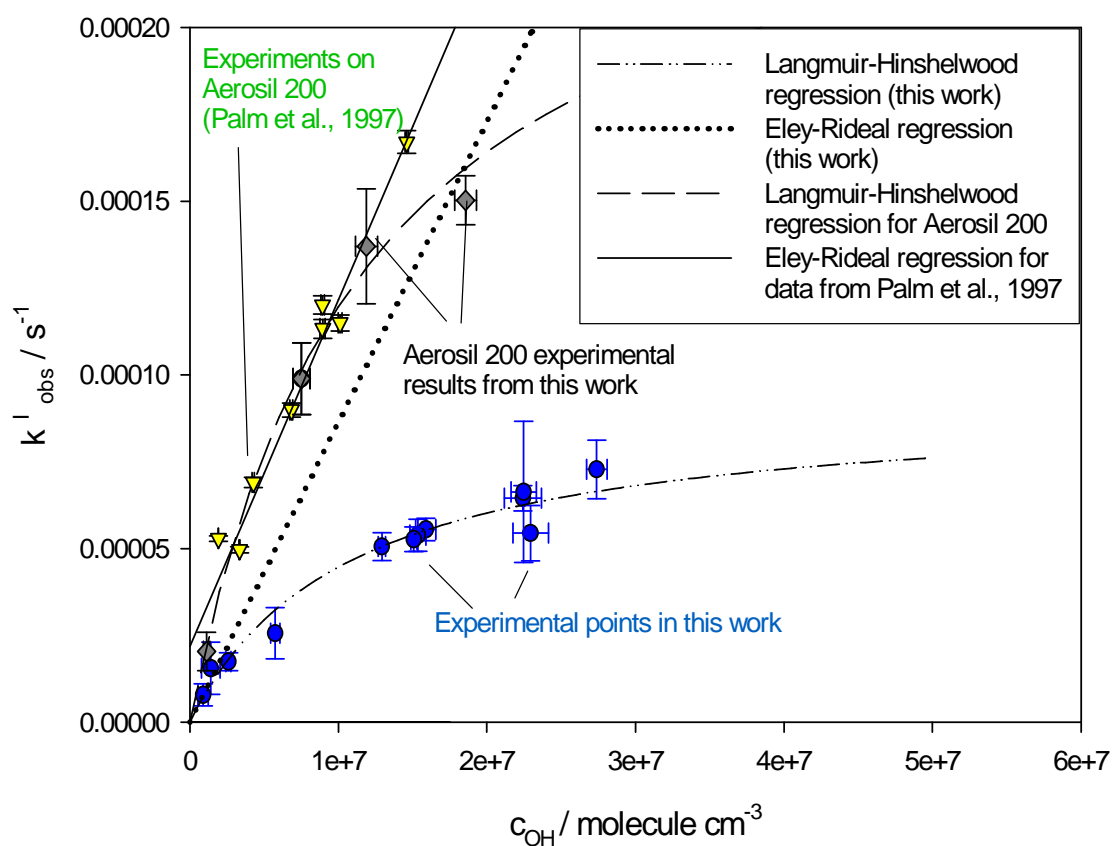


Figure 7.20 Experimental pseudo-first-order rate constant k_{obs}^I versus OH radical concentration, in comparison with experiments with Aerosil 200 as carrier particles.

From the Eley-Rideal regressions both on Aerosil 200 particles ($k_{\text{obs}}^I = 9.98 \times 10^{-12} \times C_{\text{OH}} + 2.18 \times 10^{-5}$) and on the self-synthesized SiO_2 particles ($k_{\text{obs}}^I = 8.6 \times 10^{-12} \times C_{\text{OH}}$), the results are quite similar. It shows that other factors do not have a big impact on the chemical kinetics of the heterogeneous reaction of OH radicals with aerosol-borne terbuthylazine, such as the volume of the smog chamber, type of solar simulator, and source of OH radicals.

Behnke et al. (1987b) reported the second order rate constant for the heterogeneous reaction of OH radicals with di-(2-ethylhexyl)-phthalate, which was adsorbed on different metal oxide aerosols. Their results confirmed that there was a higher heterogeneous OH reactivity on aerosols which had high surface areas (more than $100 \text{ m}^2 \text{ g}^{-1}$), while the rate constant decreased about 40% for reactions on coal fly ash, whose surface areas was only $8 \text{ m}^2/\text{g}$. Sørensen et al., (2002) have proposed that, for

volatile organic compounds, different types of aerosol have no effect on the rate for reaction of OH radicals with gaseous organic compounds. However, their work mainly focused on gas-phase kinetics, so it is not relevant to heterogeneous kinetics. Considering that there have been only a few studies about heterogeneous atmospheric reactions of OH radical with SVOCs, further investigations are urgently needed.

7.5.6 Result of an experiment at higher OH level

In this study, an attempt of applying higher OH concentration to the system was made. During one experimental run, hydrazine and ozone were used as OH precursor (for the detailed mechanism, see chapter 4) and a high level of OH radicals was achieved ($(3.41 \pm 0.17) \times 10^7$ molecule cm^{-3}). The second order rate constant for heterogeneous reaction was expected to follow the Langmuir-Hinshelwood regression as well. However, the result showed a deviation from the regression line obtained before (see Figure 7.21). The calculated rate constant k_{OH} appeared to be quite low and did not follow the Langmuir-Hinshelwood regression at 25 °C. This data point seemed to be an outlier.

When we compare our result with other experimental study, which was performed at Marseille (Pflieger et al., 2013) in flow reactors at higher OH concentration ($(9.0 \pm 4.0) \times 10^7$ molecule cm^{-3}), it shows that the rate constant obtained from Pflieger ($k = (1.5 \pm 0.8) \times 10^{-13}$ cm^3 molecule $^{-1}$ s $^{-1}$) was much too low to follow the Langmuir-Hinshelwood regression derived from experimental data in this study (see Figure 7.22, Figure 7.23).

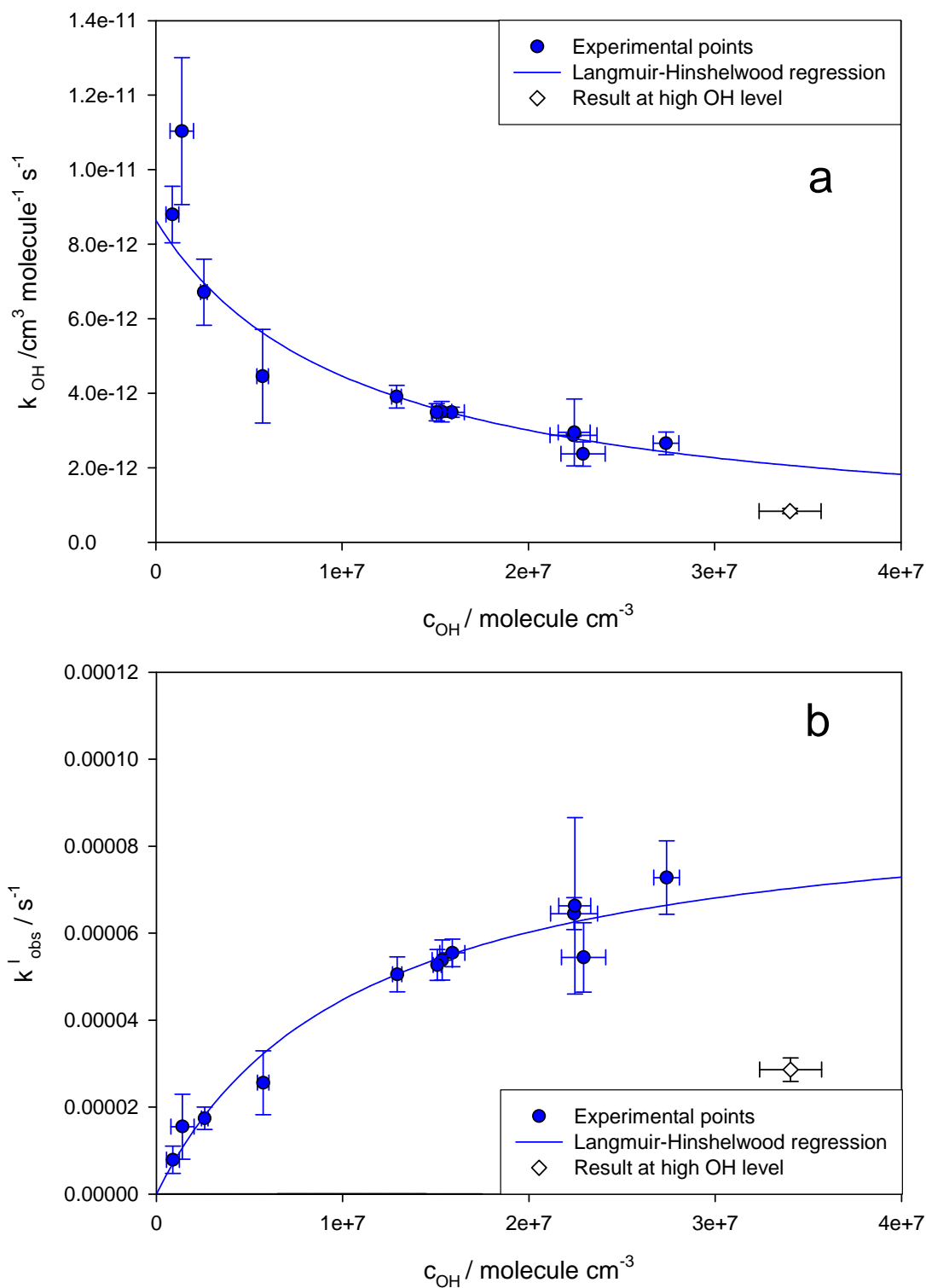


Figure 7.21 Experimental results of the heterogeneous reaction of OH radical with terbuthylazine adsorbed on SiO₂ particle at high OH concentration. a) Second order rate constant k_{OH} versus OH radical concentration; b) pseudo-first-order rate constant k_{obs}^I versus OH radical concentration

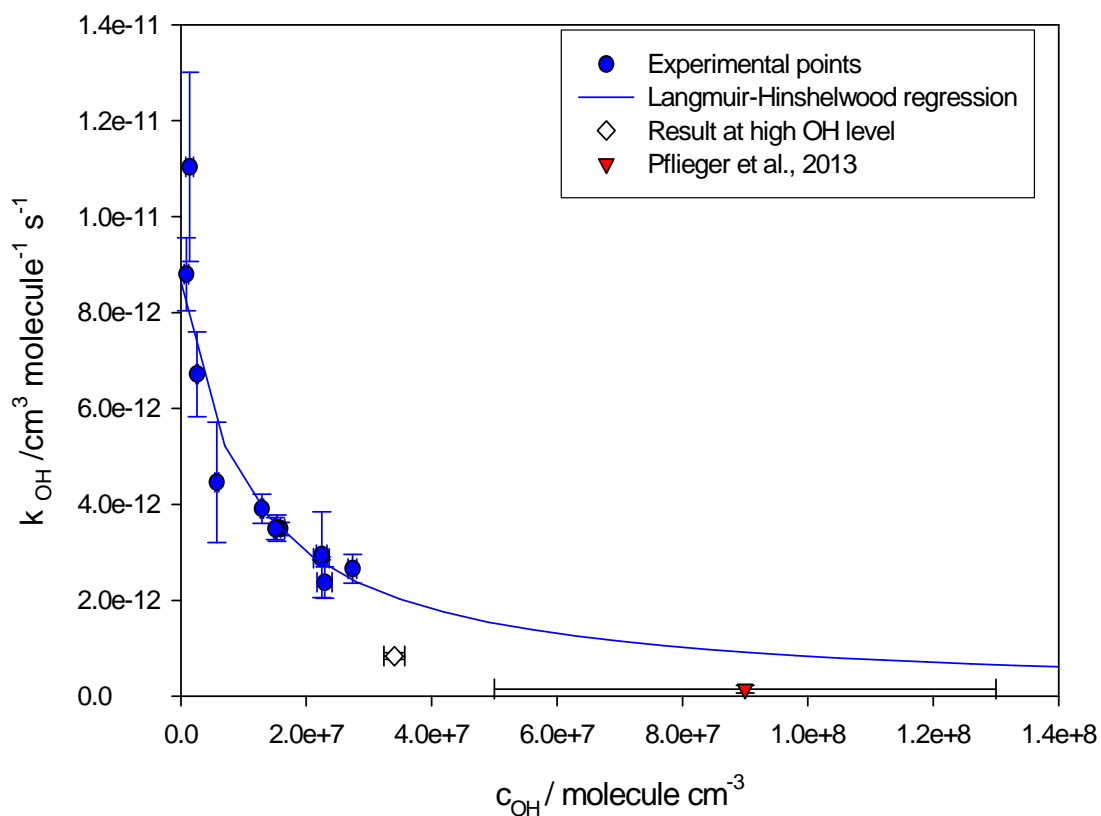


Figure 7.22 Second order rate constant k_{OH} versus OH radical concentration in the LOTASC chamber, shown in combination with results from other studies at higher OH concentration. \diamond Experiment with hydrazine and O_3 as precursor on self-synthesized SiO_2 particles, \blacktriangledown result from Pflieger et al. (2013)

Thinking about the concentration of OH radicals, one has to define the apparent OH concentration and the actual OH concentration which really takes part in the heterogeneous reaction. From Equation 3.7, a new formula could be derived as Equation 7.8:

$$k_{obs}^I = \frac{k_{max}^I \cdot K_{OH} \cdot C_{OH}}{(1 + K_{OH} \cdot C_{OH})} \quad 3.7$$

$$k_{obs}^I = \frac{k_{max}^I \cdot K_{OH}}{\left(\frac{1}{C_{OH}} + K_{OH}\right)} \quad 7.8$$

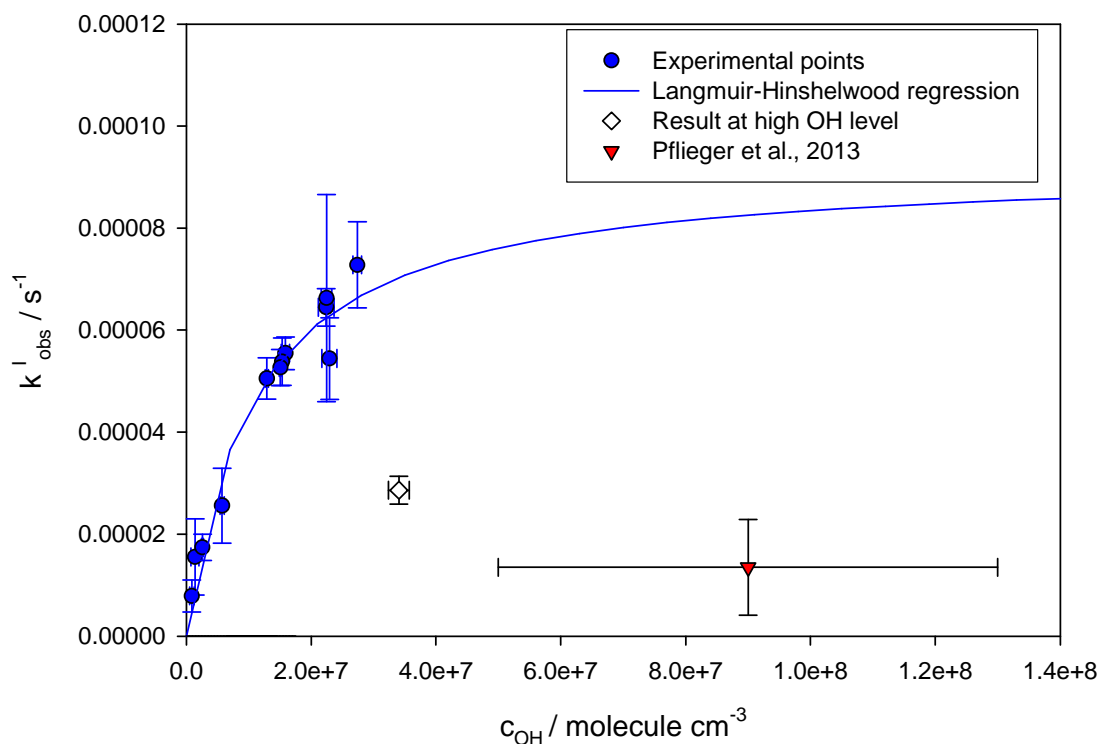


Figure 7.23 Experimental pseudo-first-order rate constant k_{obs}^I versus OH radical concentration, in combination with results from other studies at higher OH concentration. ◇ Experiment with hydrazine and O_3 as precursor on self-synthesized SiO_2 particles, ▼ result from Pflieger et al. (2013)

In Equation 7.3, the OH concentration only occurs in the denominator, so that k_{obs}^I has a positive correlation with C_{OH} . In this case, a low k_{obs}^I value could be probably related to a low OH concentration, which actually participates in the heterogeneous reaction. In the work of Pflieger et al. (2013), although they reported a very high OH concentration ($(9.0 \pm 4.0) \times 10^7 \text{ molecule cm}^{-3}$), it only represents an "apparent" OH concentration, the OH radicals which really take part in the heterogeneous reaction could be very few. The result from Pflieger et al. (2013) is not relevant to the Langmuir-Hinshelwood mechanism. What's more, due to the small volume of the flow reactor, the OH radicals are probably not homogeneously dispersed inside, which will absolutely cause different kinetics on the aerosol surfaces. From this point, the uncertainty of measurement is greatly increased. Considering the differences of flow reactor and smog chamber studies, further investigations are needed to understand more about the mechanism of heterogeneous kinetics on aerosol surfaces.

Table 7.5 Comparison of experimental conditions of different terbuthylazine experiments

	Palm et al. (1997)	This work	Pflieger et al., (2013)
Device	Smog chamber (2400L)	Smog chamber (3200L)	Flow reactor (~230 cm ³)
Carrier particle-Silica	Aerosil 200	Self-synthesized SiO ₂	Aerosil R812
OH precursor	H ₂ O ₂ , O ₃ , NO ₂	Methyl nitrite	2,3-Dimethyl-2-butene (ozonolysis)
Light source	Osram, HMI-Metallogen	Osram Eversun (16)	None
OH concentration	10 ⁵ -10 ⁷ cm ⁻³	10 ⁵ -3×10 ⁷ cm ⁻³	(9.0 ± 4.0) × 10 ⁷ cm ⁻³
Relative humidity	42-50%	20-30%	0.7%

Table 7.5 shows the different experimental conditions applied in the previous work from Palm et al. (1997) and Pflieger et al. (2013). According to the conclusions in Chapter 7.5.5 that the source of OH and volume of smog chamber have no impact to the chemical kinetics; only the characteristics of particle would affect the mechanism and rate of heterogeneous reactions. Table 7.6 lists the comparison of Aerosil 200 and Aerosil R812 particles.

Table 7.6 comparison of particle characteristics of Aerosil 200 and Aerosil R812

Type	Aerosil 200	Aerosil R812
Particle size	12 nm	7 nm
Hydrophobicity	Hydrophilic	Hydrophobic
Specific surface area (m ² g ⁻¹)	200	260

The surfaces of Aerosil R812 particles are occupied by methyl groups (Bode et al., 1967). Those organic groups have moderate reactivity to OH radicals (1.0×10⁻¹² cm³ molecule⁻¹ s⁻¹, Atkinson, 1991), which will consume most of the OH radicals in the

gas phase and suppress the reaction of OH with adsorbed terbuthylazine, especially in the narrow flow reactor system. According to Equation 3.9, this could be a reasonable explanation why the result from Pflieger et al. (2013) is far away from the results of Palm et al. (1997) and also the results from this work.

$$r' = \frac{k \cdot k_A \cdot C_A \cdot X \cdot C_S \cdot C_{BS}}{k_A \cdot C_A + k \cdot C_{BS} + k_{A'} + k_{\text{other}} \cdot C_{\text{organic}}} = \frac{k_{\text{max}}^I \cdot K_A \cdot C_A}{K_A \cdot C_A + 1 + \frac{k_{\text{other}} \cdot C_{\text{organic}}}{k_{A'}}} \quad 3.9$$

During the process to synthesize SiO₂ particles, there could also be precursors (Si(OC₂H₅)₄) left on surface of the monodisperse silica particles. Those organic groups would also have some impact on the heterogeneous rate constant.

The special distribution of OH radicals also raises a question. In smog chamber experiments, with the ventilator, the OH precursor was dispersed in the chamber before the solar simulator was switched on; however, this question remains unclear whether the OH radicals in the flow tube could also be evenly dispersed. Suppose the OH radicals accumulated more close to the inlet of the flow tube and could not reach inside, the coated terbuthylazine molecules then had less chance to react with high concentration of OH radicals. In such a case, the observed heterogeneous reactivity would be quite low.

Another possible explanation is that the relative humidity varied in the different studies (42% on Aerosil 200, Palm et al., 1997; 32% on self-synthesized SiO₂, this study; and 0.7% on silica, Pflieger et al., 2013), which could have an impact on the heterogeneous reaction on particle surfaces. Previous research on oxidation of aerosol-borne SVOCs by ozone has shown some results on the impact of relative humidity to the heterogeneous kinetics. Kwamena et al. (2004) reported that at higher relative humidity the kinetics could be accelerated. However, in another study from their group (Kwamena et al., 2006), there was no change for the kinetics at different relative humidities. There are also studies in which decreased PAH reactivity was observed at higher relative humidity, especially from the work by Pitts et al. (1986). In this regard, it is not clear what effect relative humidity would have on the

heterogeneous kinetics on aerosol surface.

7.6 Experimental results of the heterogeneous reaction of OH radicals with terbuthylazine adsorbed on SiO₂ particles at different temperatures

In this work, chamber experiments were also performed at low temperatures (6.5°C and -10°C), in order to understand the temperature dependence of the heterogeneous reaction. Results were also evaluated with the Langmuir-Hinshelwood and Eley-Rideal mechanisms.

7.6.1 Experiments at 6.5°C for the reaction of OH radical with terbuthylazine on SiO₂ particles

Table 7.3 (see Chapter 7.4) summarizes the experimental results performed at 6.5°C. Data points are plotted in Figure 7.24 and Figure 7.25. Results at 6.5°C have shown a similar trend as those at 25°C. The Langmuir-Hinshelwood and Eley-Rideal regression lines are shown in the figures.

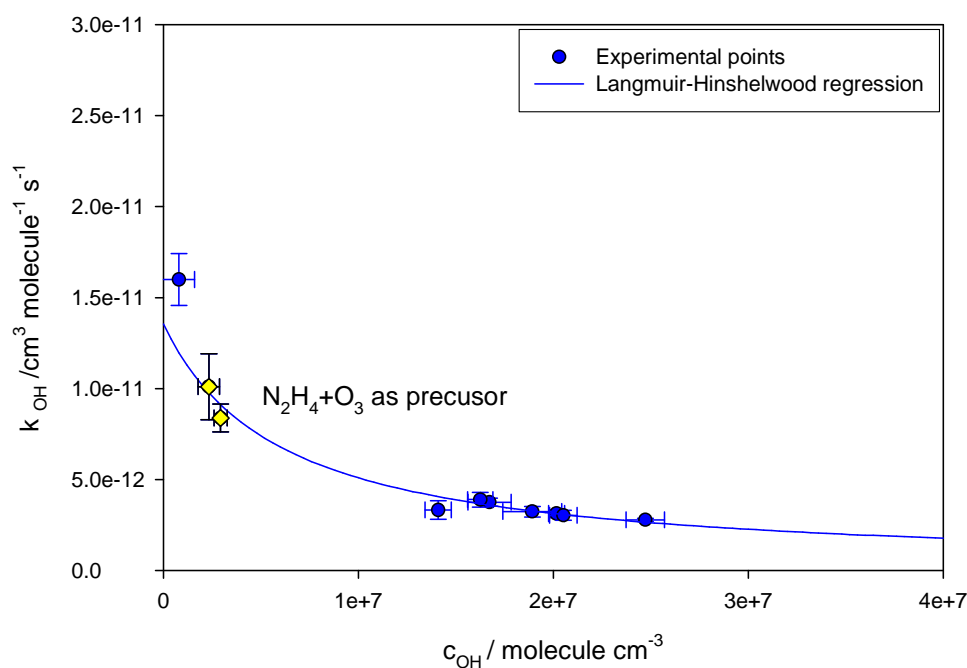


Figure 7.24 Experimental results of second order rate constant k_{OH} versus OH radical concentration on the self-synthesized SiO₂ particle at 6.5 °C

Following the previous calculation procedure (described in chapter 7.5.4), k_{\max}^I and K_{OH} could be obtained from the linear regression of reciprocal of k_{OH} versus C_{OH} (see Figure 7.26). The calculation results of k_{\max}^I and K_{OH} are shown below:

$$k_{\max}^I = (7.89 \pm 0.89) \times 10^{-5} \text{ s}^{-1}$$

$$K_{\text{OH}} = (1.07 \pm 0.24) \times 10^{-7} \text{ cm}^3 \text{ molecule}^{-1}$$

The expression of the Langmuir-Hinshelwood regression is given in Equation 7.9:

$$k_{\text{obs}}^I = 8.5 \times 10^{-12} C_{\text{OH}} / (1 + 1.07 \times 10^{-7} C_{\text{OH}}) \quad 7.9$$

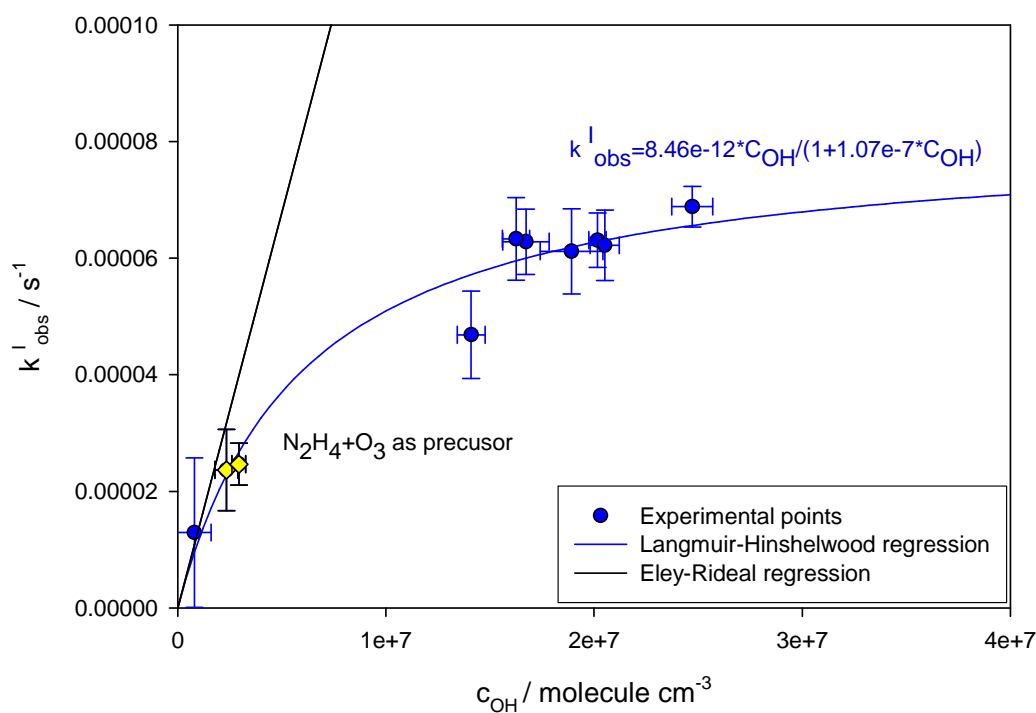


Figure 7.25 Experimental results of the pseudo-first-order rate constant k_{obs}^I versus OH radical concentration on the self-synthesized SiO_2 particle at 6.5°C

Based on the discussion in Chapter 7.5.4, the Eley-Rideal regression can be obtained from $k_{\max}^I \times k_{\text{OH}}$, for $C_{\text{OH}} \rightarrow 0$ from Equation 3.8. The k_{OH} (Eley-Rideal) then equals to $k_{\max}^I \times k_{\text{OH}}$ and yields $(8.5 \pm 1.6) \times 10^{-12} \text{ cm}^3 \text{ molecule}^{-1} \text{ s}^{-1}$.

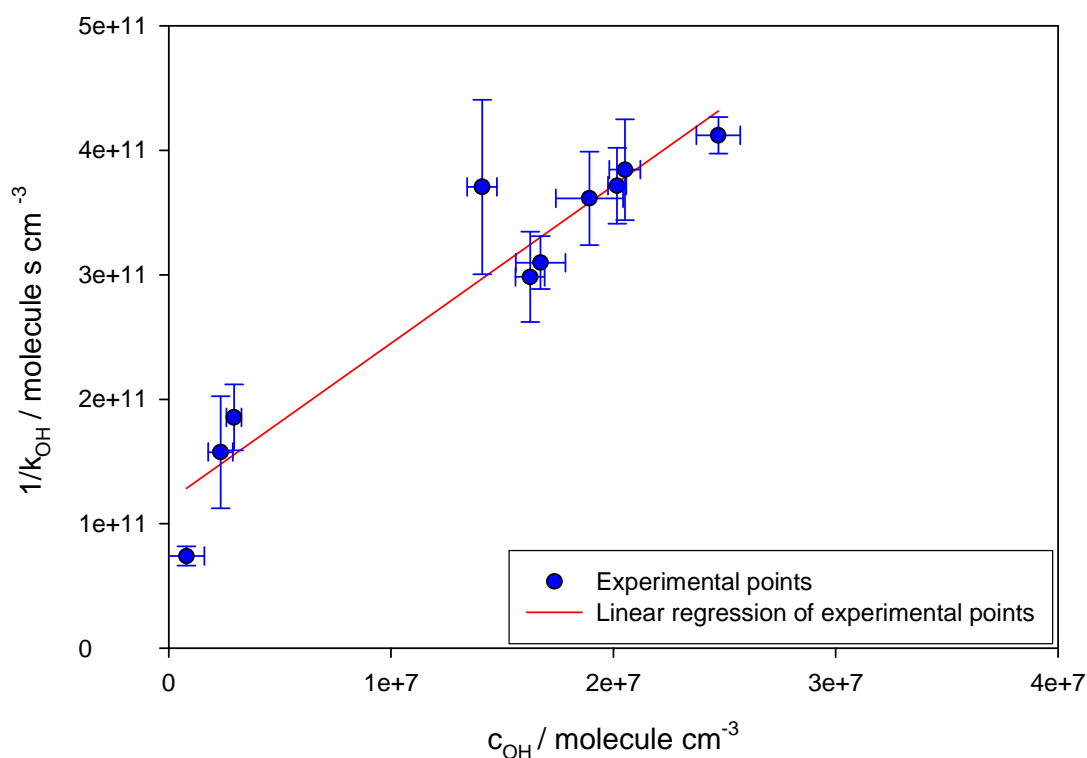


Figure 7.26 Reciprocal of k_{OH} versus OH radical concentration for all experiments at 6.5°C .

7.6.2 Comparison with previous experiments on the reaction of OH radicals with TBA adsorbed on filters at 6.5°C

Filter experiments of terbuthylazine adsorbed on Aerosil 200 were performed previously at 6.5°C in the smog chamber by exposing filter samples of coated particles to OH radicals. The procedure of how to prepare the filter samples was described in detail in Palm et al. (1998). Results from this work and those from Krüger (2001) were plotted together in Figure 7.27, 7.28 and 7.29.

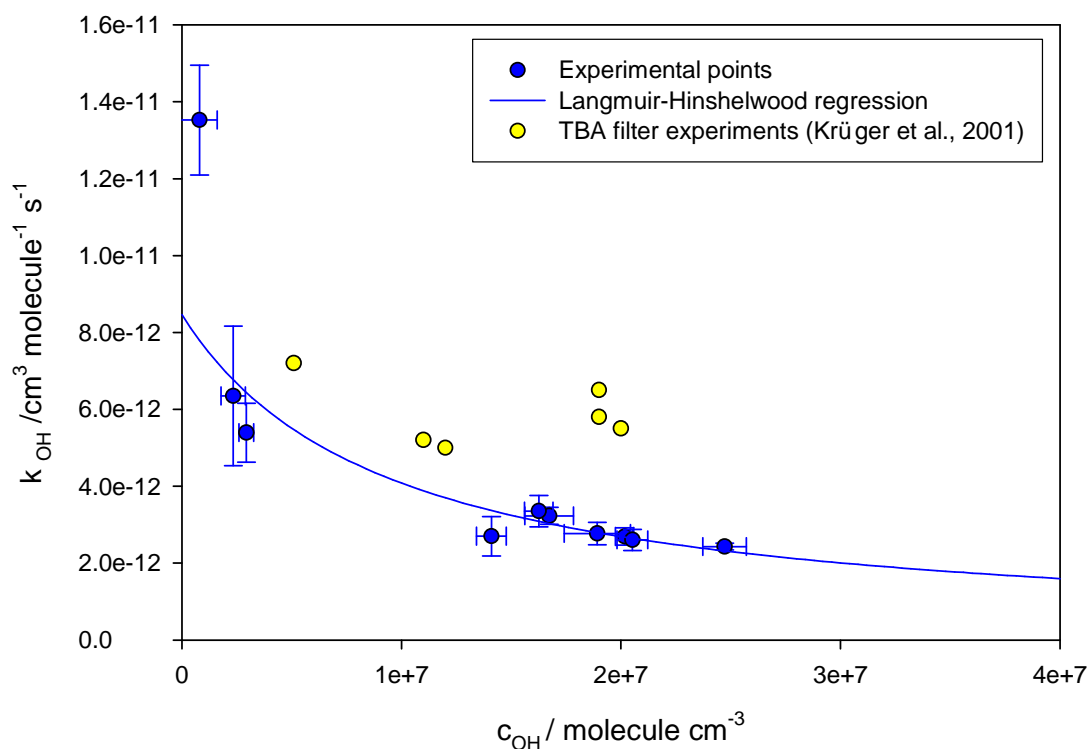


Figure 7.27 Experimental results of second order rate constant k_{OH} versus OH radical concentration on the self-synthesized SiO_2 particle at 6.5 °C (in combination with previous data from Krüger et al., (2001))

Previous results at 6.5 °C (Krüger, 2001) have shown that the second order rate constants on Aerosil 200 particles on filter samples are higher than the results from reactions on aerosol-borne SiO_2 particles. From Figure 7.28, it can be seen that experiments on filter samples with Aerosil 200 follow the Eley-Rideal mechanism. A linear regression of k_{obs}^I versus OH concentration yields the second order rate constant k_{OH} as the slope. $k_{OH(\text{filter})} = (5.84 \pm 0.75) \times 10^{-12} \text{ cm}^3 \text{ molecule}^{-1} \text{ s}^{-1}$ for previous filter experiments ($r^2 = 0.94$, as shown in Figure 7.28). This value is lower than the $k_{OH(\text{Eley-Rideal})}$ value from the experimental results on SiO_2 particles ($(8.5 \pm 1.6) \times 10^{-12} \text{ cm}^3 \text{ s}^{-1}$), which means that if compressed on filter samples, the kinetic reactivity could be reduced because of steric hindered access to the OH radicals.

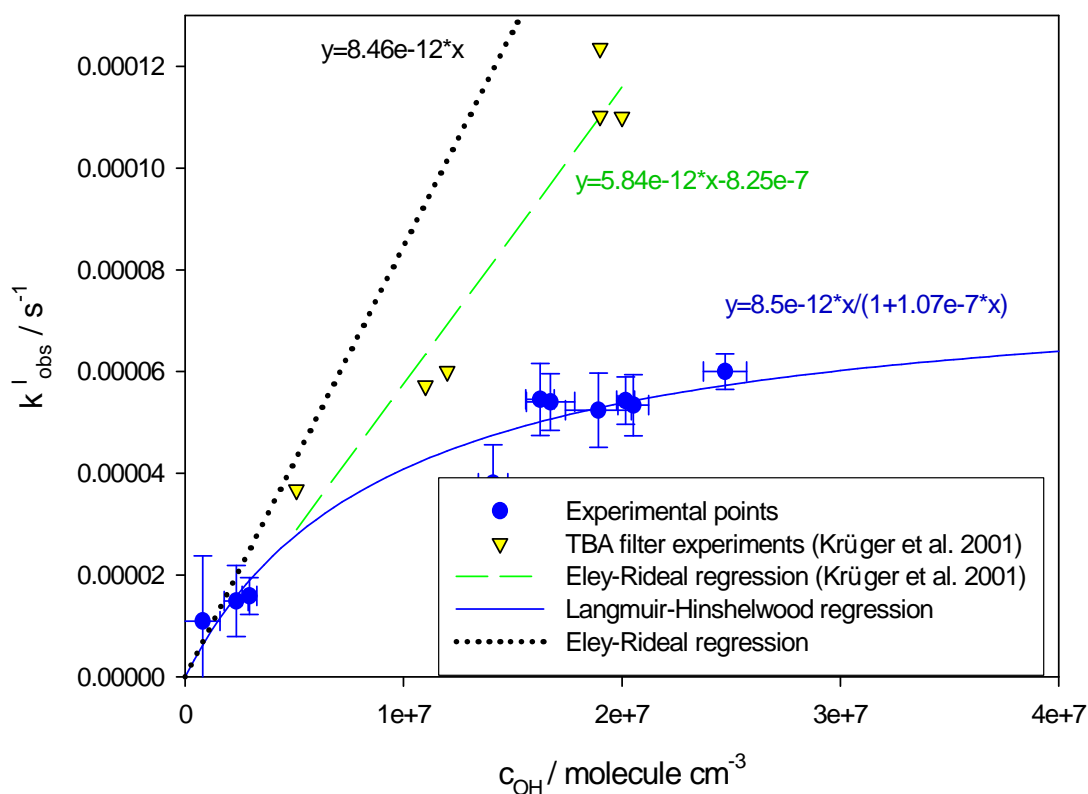


Figure 7.28 Experimental results of pseudo-first-order rate constant $k_{\text{obs}}^{\text{I}}$ versus OH radical concentration on the self-synthesized SiO_2 particle at 6.5°C

From Figure 7.28, it can be clearly seen that for the heterogeneous reaction on the self-synthesized SiO_2 particles, the heterogeneous kinetics follows mainly the Langmuir-Hinshelwood mechanism. The Eley-Rideal regression obtained from this work could be a model for the gas phase. Results from filter samples at 6.5°C give a lower $k_{\text{OH(Eley-Rideal)}}$ value $((5.84 \pm 0.75) \times 10^{-12} \text{ cm}^3 \text{ molecule}^{-1} \text{ s}^{-1})$, in comparison with the aerosol experimental results with Aerosil 200 at room temperature (Palm et al., 1997). The explanation could be that either the reactivity on aerosol surfaces would be reduced at lower temperature or the compressed state of aerosols on filters could prevent the access of OH radicals to the aerosol-borne terbuthylazine, in comparison with conditions on free aerosols in the smog chamber.

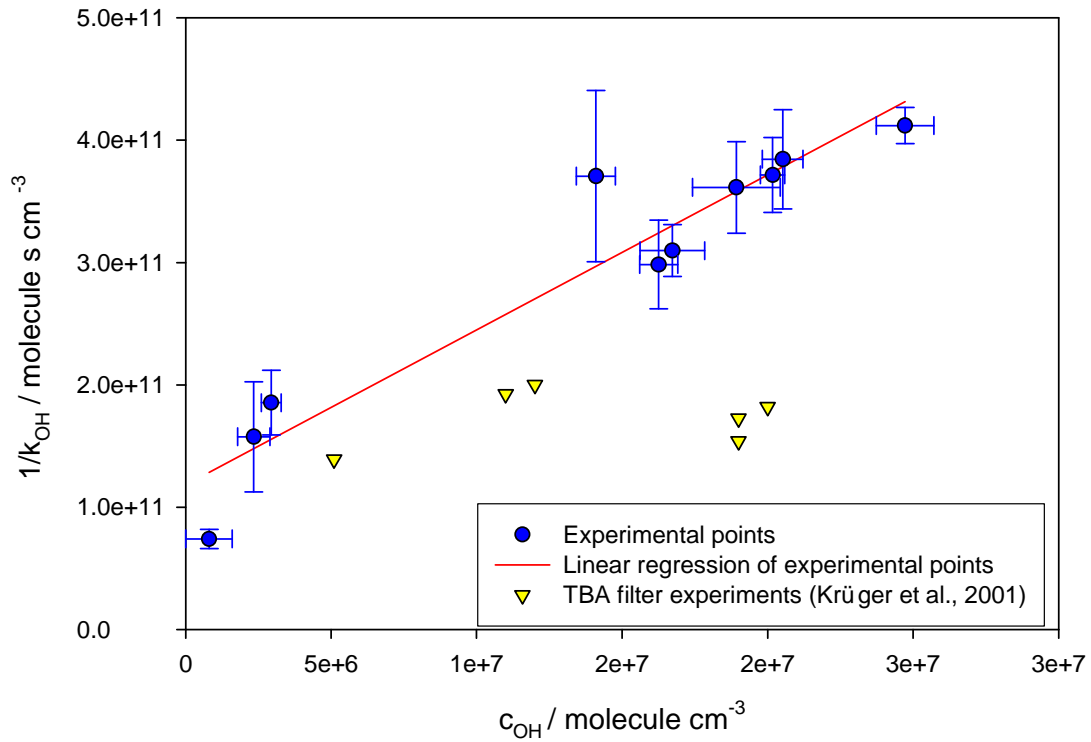


Figure 7.29 Reciprocal of k_{OH} versus OH radical concentration for all experiments at 6.5°C.

7.6.3 Experiments at -10°C for the reaction of OH radical with terbuthylazine on SiO_2 particles

Table 7.4 (see Chapter 7.4) summarized the experimental results at -10°C for reaction of OH radical with aerosol-borne terbuthylazine. Results at -10°C (Figure 7.30 and Figure 7.31) follow mainly the Langmuir-Hinshelwood mechanisms. In Figure 7.31, the Eley-Rideal mechanism estimation is also given. From the linear regression of the reciprocal of k_{OH} versus C_{OH} (see Figure 7.32), k_{max}^I and K_{OH} are calculated as below:

$$k_{max}^I = (4.33 \pm 0.38) \times 10^{-5} \text{ s}^{-1}$$

$$K_{OH} = (1.40 \pm 0.26) \times 10^{-7} \text{ cm}^3 \text{ molecule}^{-1}$$

The expression of Langmuir-Hinshelwood mechanism is shown in Equation 7.10:

$$k_{obs}^I = 6.08 \times 10^{-12} C_{OH} / (1 + 1.40 \times 10^{-7} C_{OH}) \quad 7.10$$

According to the previous discussion, the Eley-Rideal regression can be obtained from $k_{max}^I \times k_{OH}$, in condition of $C_{OH} \Rightarrow 0$ from Equation 3.8. The $k_{OH(Eley-Rideal)}$ then equals to $k_{max}^I \times k_{OH}$ and yields $(6.08 \pm 0.97) \times 10^{-12} \text{ cm}^3 \text{ molecule}^{-1} \text{ s}^{-1}$.

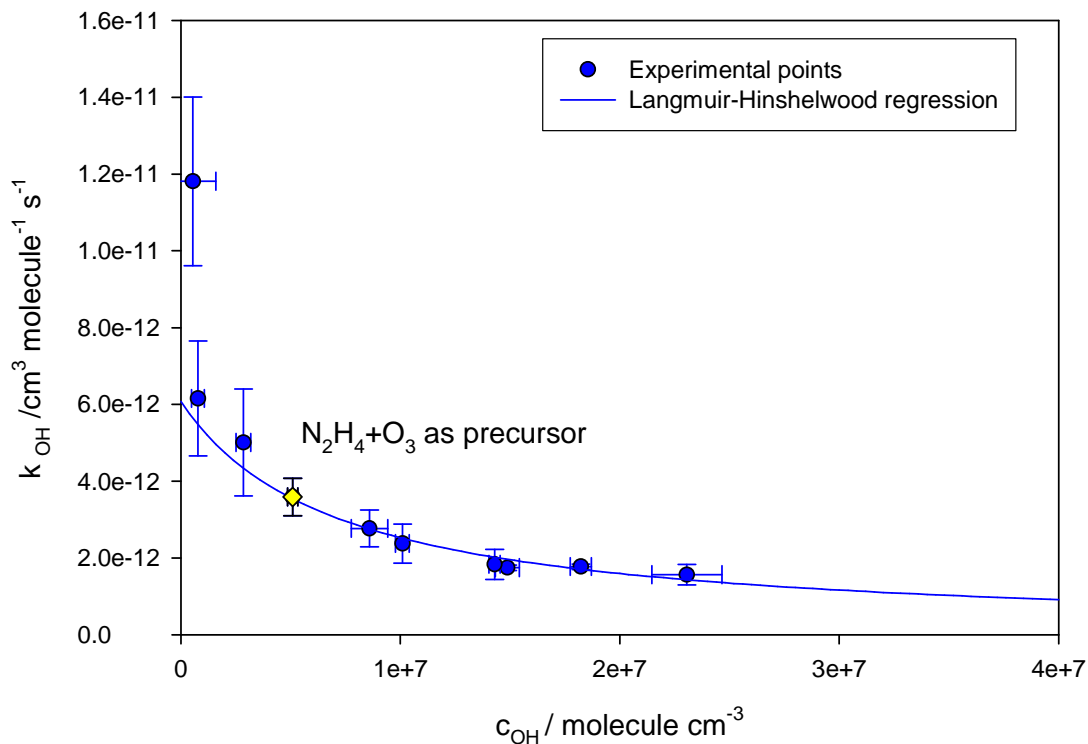


Figure 7.30 Experimental results of second order rate constants k_{OH} versus OH radical concentrations on the self-synthesized SiO₂ particle at -10°C

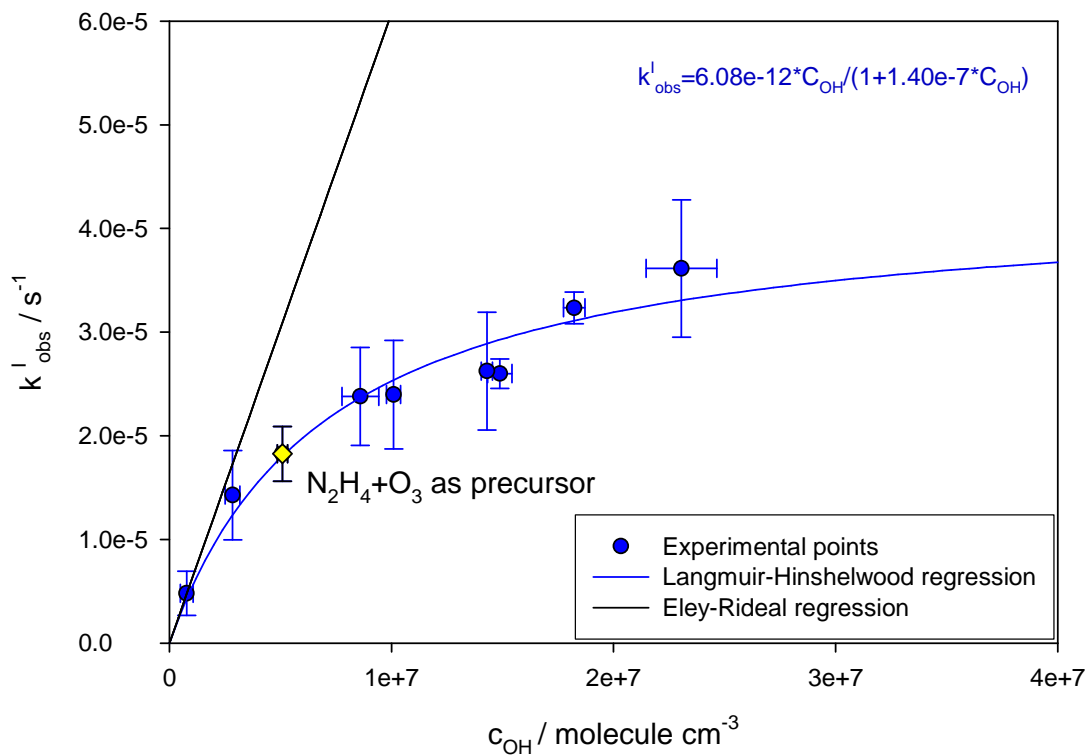


Figure 7.31 Experimental results of the pseudo-first-order rate constants, k_{obs}^I , versus the OH radical concentrations on the self-synthesized SiO₂ particles at -10°C

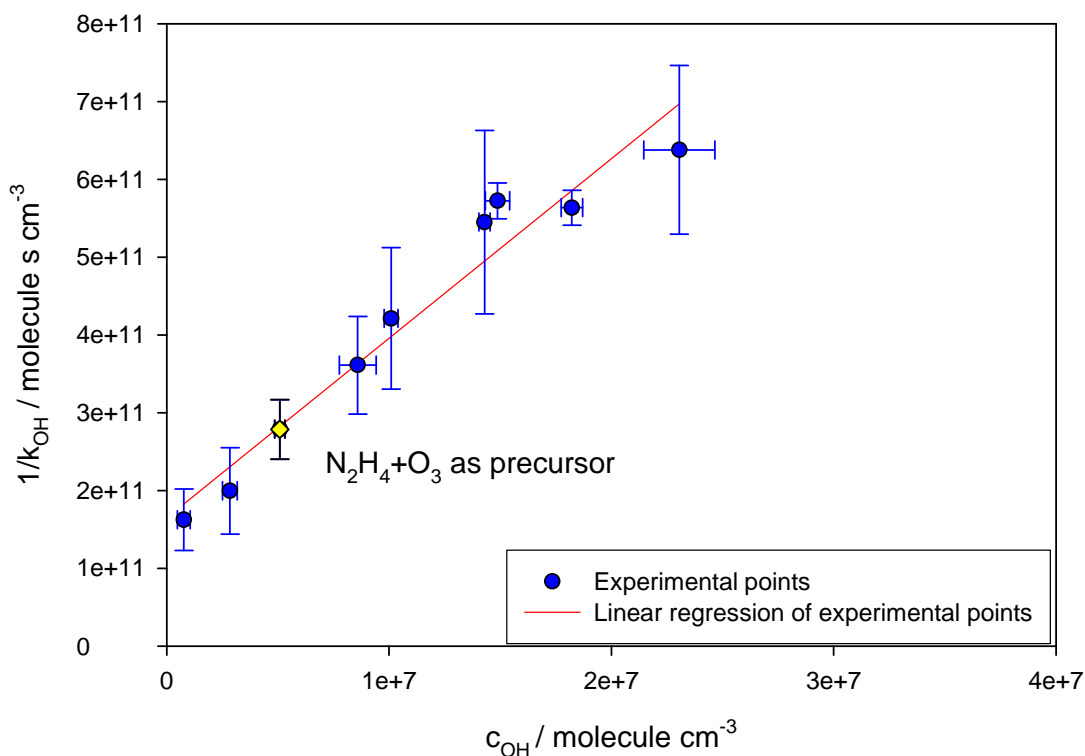


Figure 7.32 Reciprocal of k_{OH} versus OH radical concentration at -10°C .

7.7 Temperature dependence of the heterogeneous reaction on self-synthesized SiO_2 particles

Figure 7.33 shows all experimental data points at 25°C , 6.5°C and -10°C . In order to understand to what extent the temperature would have an impact on the kinetics of the heterogeneous reaction; experimental data from different temperatures are plotted versus the inverse absolute temperature (K^{-1}) in Figure 7.34. It can be seen that there is a slight temperature dependence of k_{max}^1 and K_{OH} (based on the Langmuir-Hinshelwood mechanism calculation). However, considering the difference of reactivity caused by particle characteristics ($k_{OH} = (1.1 \pm 0.2) \times 10^{-11} \text{ cm}^3 \text{ molecule}^{-1} \text{ s}^{-1}$ for Aerosil 200, and $k_{OH} = (1.42 \pm 0.35) \times 10^{-11} \text{ cm}^3 \text{ molecule}^{-1} \text{ s}^{-1}$ for self-synthesized SiO_2 particle) at 25°C , the thermodynamic factor has little impact on the reaction mechanism.

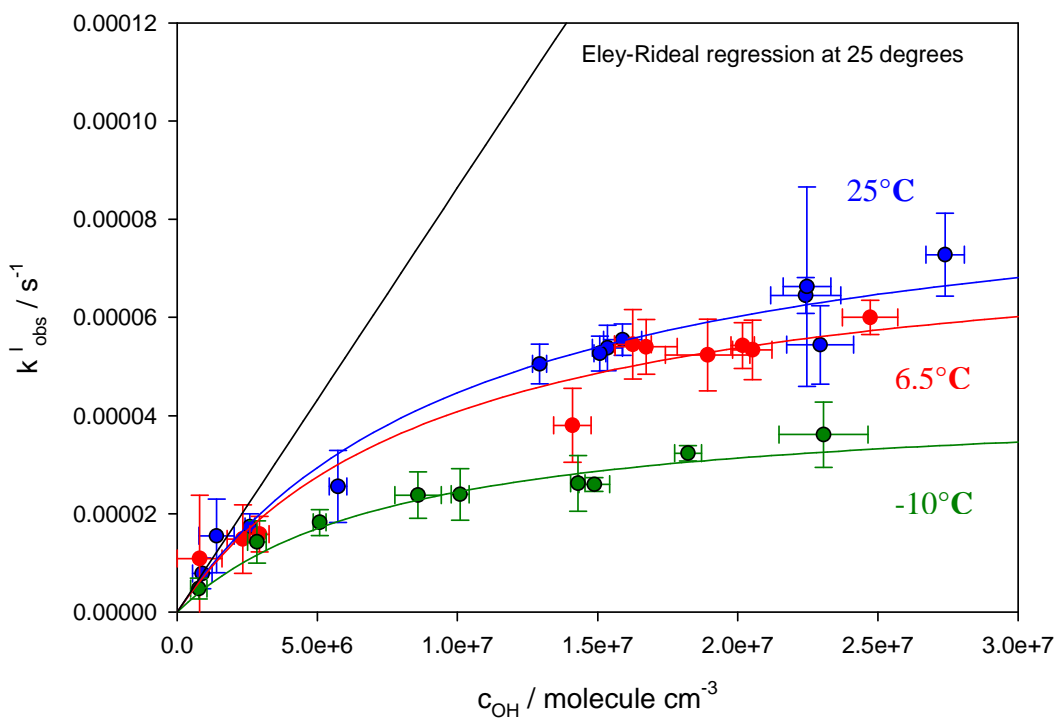


Figure 7.33 Experimental pseudo-first-order rate constants, k_{obs}^I , versus OH radical concentrations at different temperatures

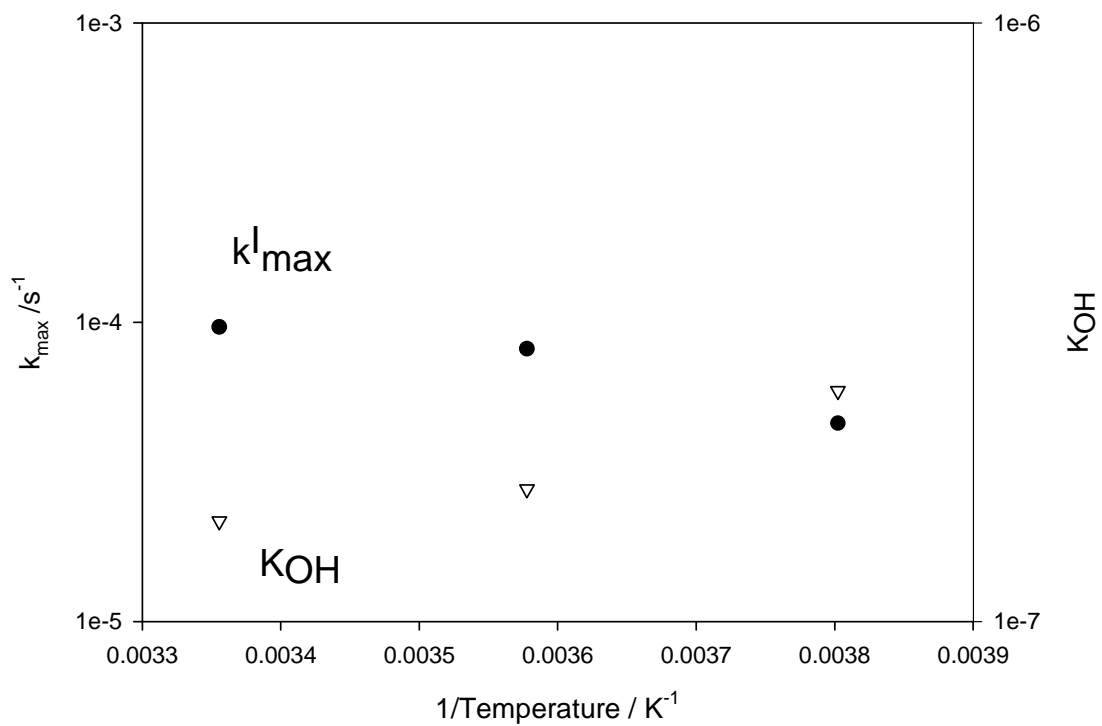


Figure 7.34 Comparison of k_{max}^I and K_{OH} at different temperatures.

According to the Arrhenius plot in Equation 7.11:

$$\ln(k) = \frac{-E_a}{R} \frac{1}{T} + \ln(A) \quad 7.11$$

Here k is the second order rate constant of a chemical reaction ($\text{cm}^3 \text{ molecule}^{-1} \text{ s}^{-1}$), T is the absolute temperature (K), E_a is the activation energy (J mol^{-1}), R is the universal gas constant ($8.314 \text{ J mol}^{-1} \text{ K}^{-1}$) and A is the pre-exponential factor.

In Figure 7.35, the natural logarithm of second rate constant k (derived from the Eley-Rideal mechanism) is plotted versus the reciprocal of temperature (absolute temperature, in K), in order to obtain an idea about the activation energy/heat of adsorption of OH. From the linear regression, E_a is calculated to be $(6.6 \pm 3.3) \text{ kJ mol}^{-1}$, and A is calculated to be 1.3×10^{-10} . Figure 7.36 shows the relation of natural logarithm of equilibrium constant K_{OH} versus the reciprocal of temperature. The adsorption heat is then calculated to be $(7.6 \pm 4.2) \text{ kJ mol}^{-1}$.

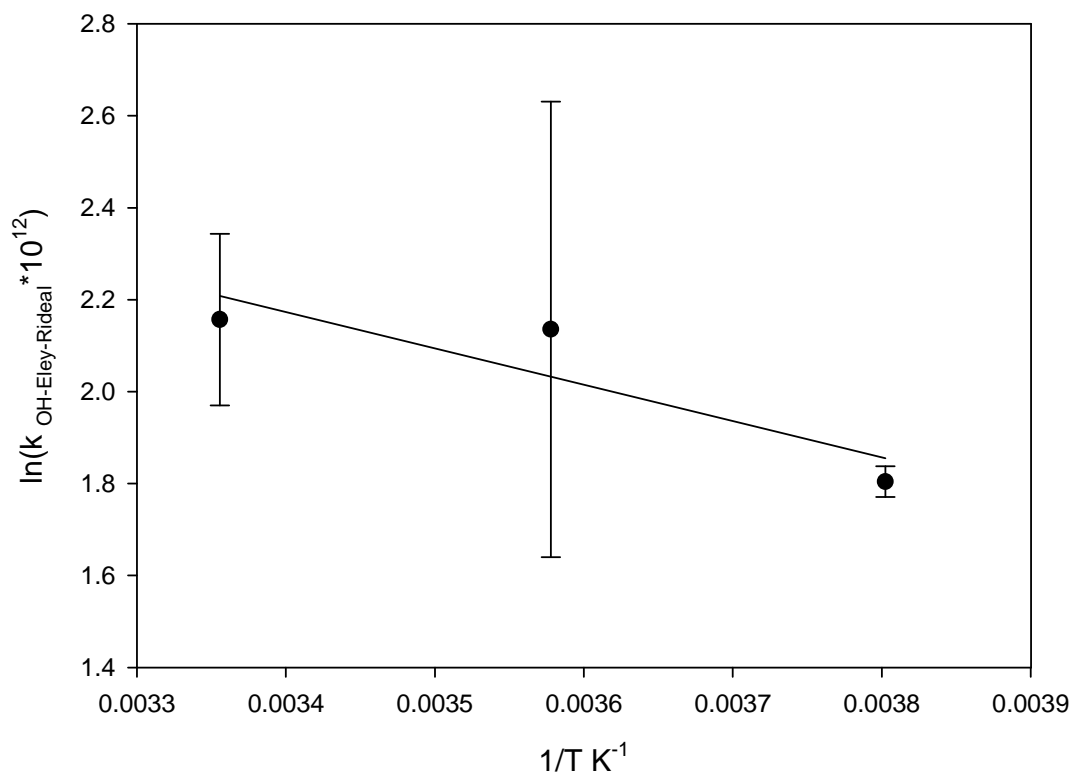


Figure 7.35 $\ln k_{\text{OH(Eley-Rideal)}}$ versus the reciprocal of temperature (T).

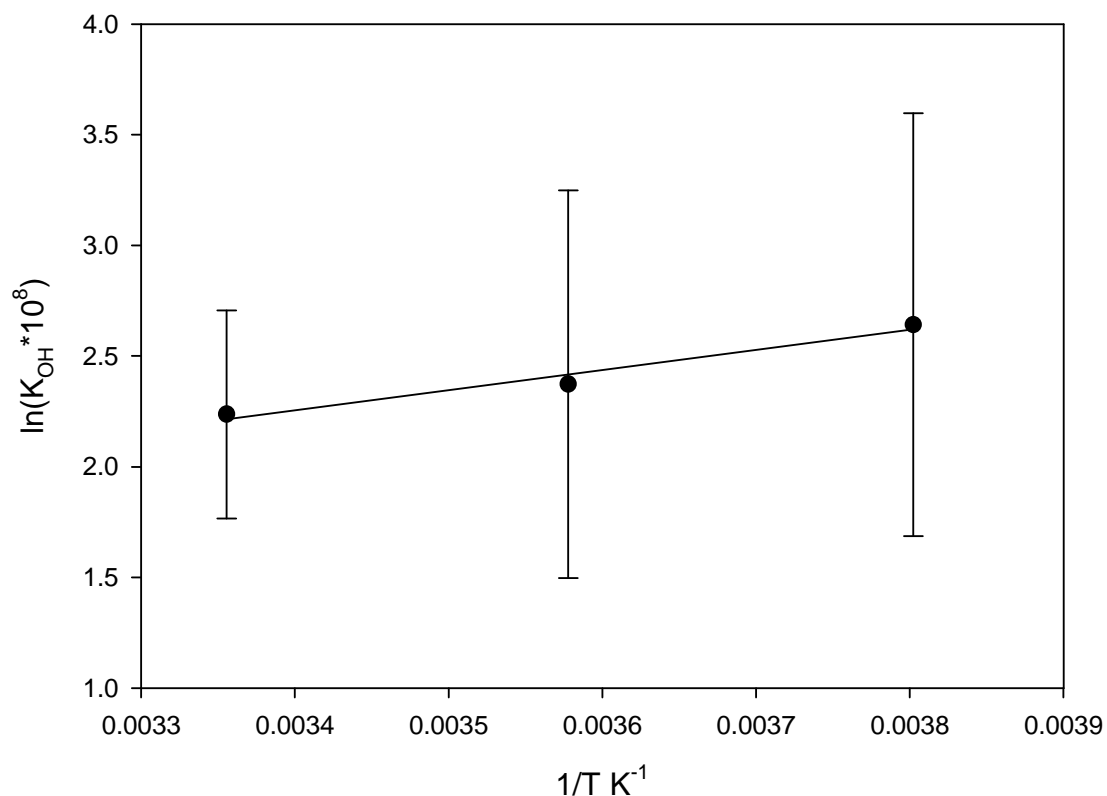


Figure 7.36 ln KOH versus the reciprocal of temperature (T).

7.8 Product analysis

The product peaks were identified with GC-FID (Siemens I, Sichromat, on column-injection) (Figure 7.37). The filter extraction was then analyzed by GC-MS (Varian Saturn GC/MS 2000, desethylterbutylazine was determined as one product (Figure 7.39). The 1,3,5-triazine-2,4-diamine,6-chloro-N,N'-bis (1-methylethyl)- (propazine) was also detected on the filter sample (Figure 7.41). However, it is also observed to be an impurity in the terbutylazine sample (see Figure 7.37).

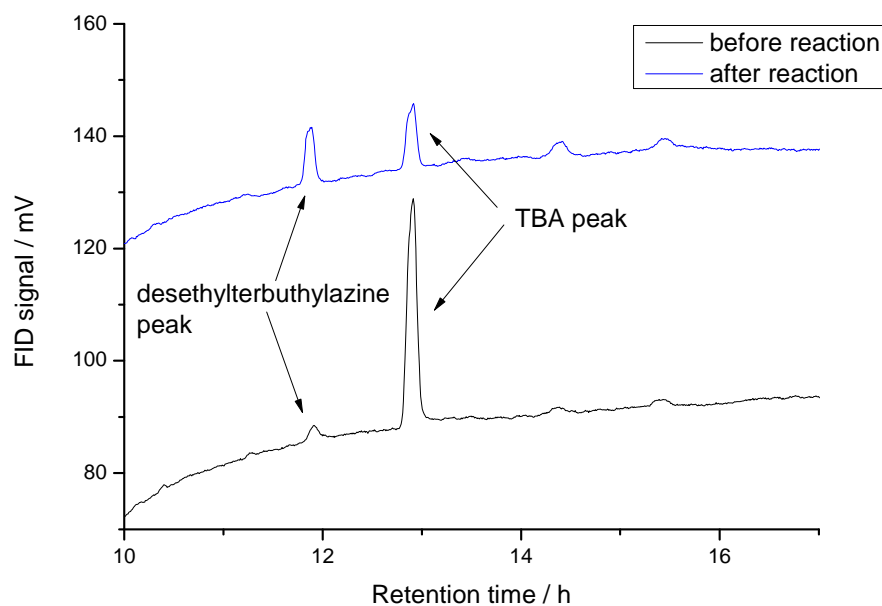


Figure 7.37 Chromatogram of filter sample extracts of GC-FID, showing the information of product peaks

Parameter of GC-MS for product analysis:

Column: Rxi-1ms (fused silica), 0.24 μm film, i.d. = 0.25 mm, column length 30 m;

Carrier gas: He

Table 7.8 Temperature program of the Varian Saturn GC/MS 2000

Temp ($^{\circ}\text{C}$)	Rate ($^{\circ}\text{C}/\text{min}$)	Hold (min)	Total (min)
60	0.0	5.00	5.00
320	20.0	2.00	20.00

Kinetics of product formation during the photochemical transformation

During the experimental run, the peak at around 11.9 min from the GC-FID chromatogram has been identified as desethylterbuthylazine. Figure 7.38 shows the kinetics of the observed product peak together with the concentration change of terbuthylazine.

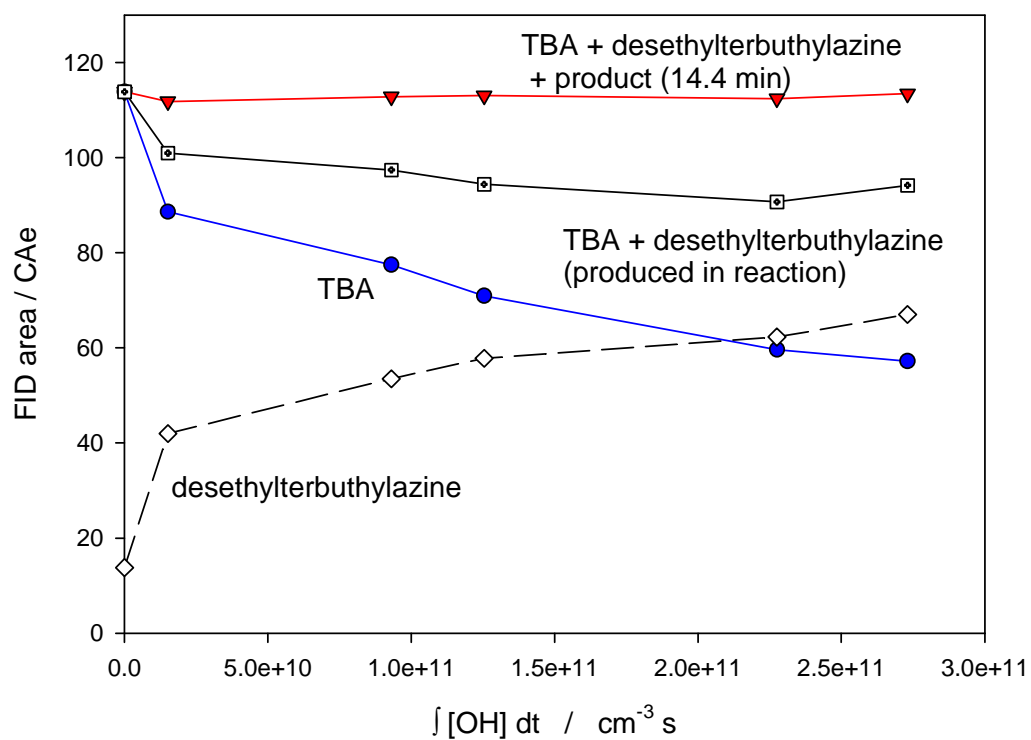
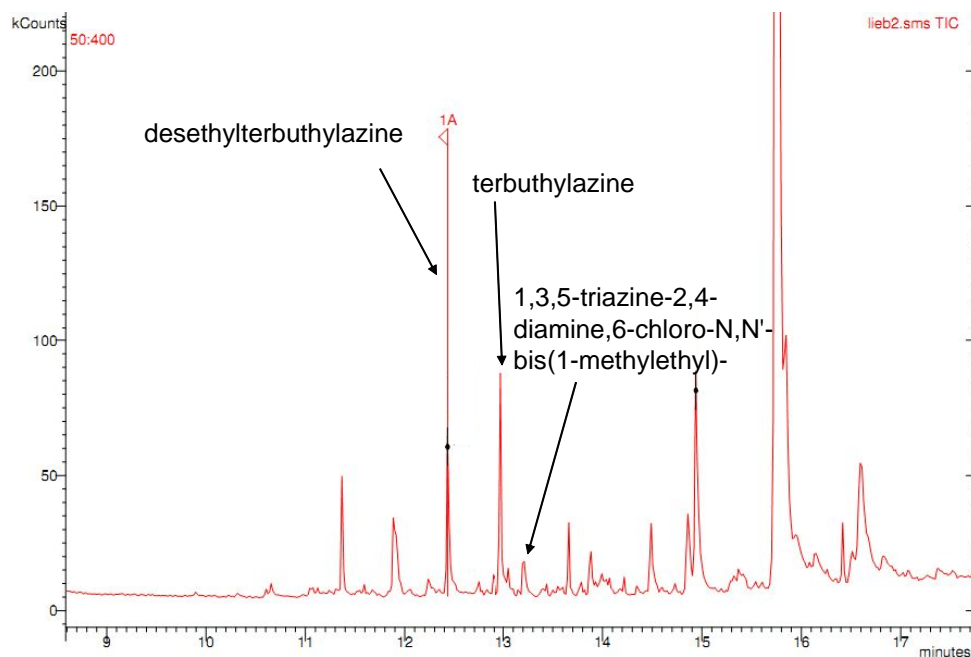


Figure 7.38 Relative concentrations of terbutylazine and one product at 11.9 min (D11115). The sum of TBA and product is also shown in the figure.



Hit 1 : Desethylterbutylazine
C7H12ClN5; MF: 827; RMF: 831; Prob 97.8%; CAS: 30125-63-4; Lib: mainlib; ID: 106085.

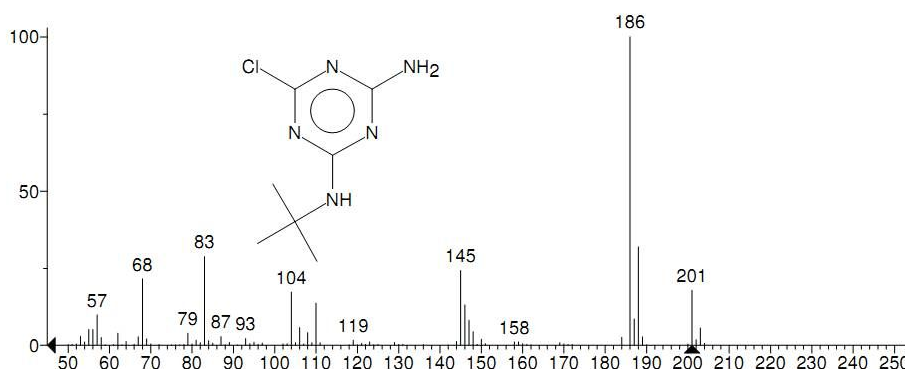


Figure 7.39 GC-MS spectrum of product information: desethylterbutylazine

Figure 7.39 shows the MS spectrum of product information. Desethylterbutylazine is observed as the main product. However, compared with previous Aerosil 200 experiments (Palm et al., 1997), 2-chloro-4-tert-butylamino-6-acetamido-s-triazine (TBA-ACE, Figure 7.40) was also identified as one product, which was not found in this work.

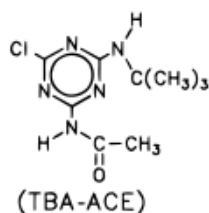


Figure 7.40 Structure of TBA-ACE

In this work, the product information shows that there is less oxidation level during the reaction. The explanation could be that on a spherical SiO₂ particle with small surface area, the gas phase OH radical has less reactivity with adsorbed semi-volatile compounds, in comparison to reactions happened on Aerosil 200 particles.

1,3,5-triazine-2,4-diamine, 6-chloro-N,N'-bis(1-methylethyl)- (propazine) was also observed (Figure 7.41). However, this compound is always regarded as impurity in the terbutylazine (European Food Safety Authority, 2011).

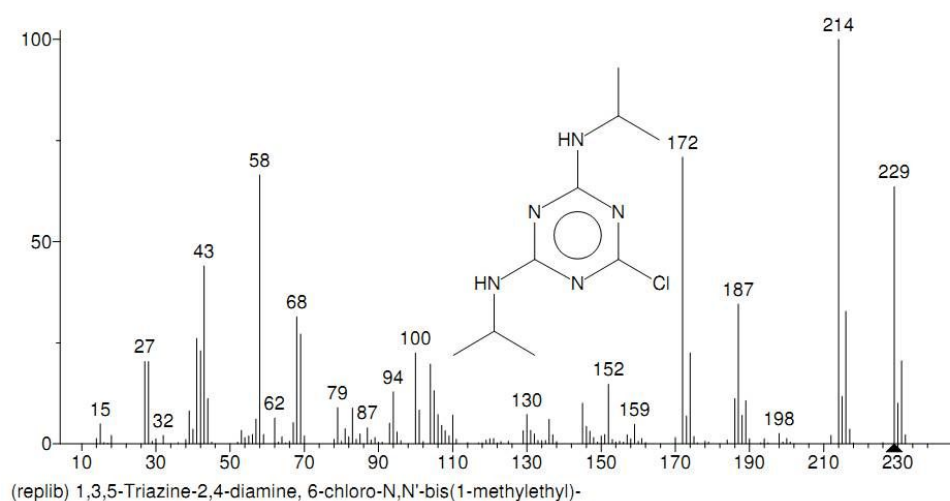


Figure 7.41 GC-MS spectrum 1,3,5 - triazine -2,4 - diamine, 6 - chloro - N,N' - bis (1-methylethyl)- (propazine)

7.9 Possible reaction pathway analysis

The reaction pathway to forming desethylterbutylazine is shown in Figure 7.42. The secondary C-H bond of the ethyl groups is attacked by OH radical, and after the following the reaction with oxygen and NO, desethylterbutylazine is finally formed, releasing acetyl radicals.

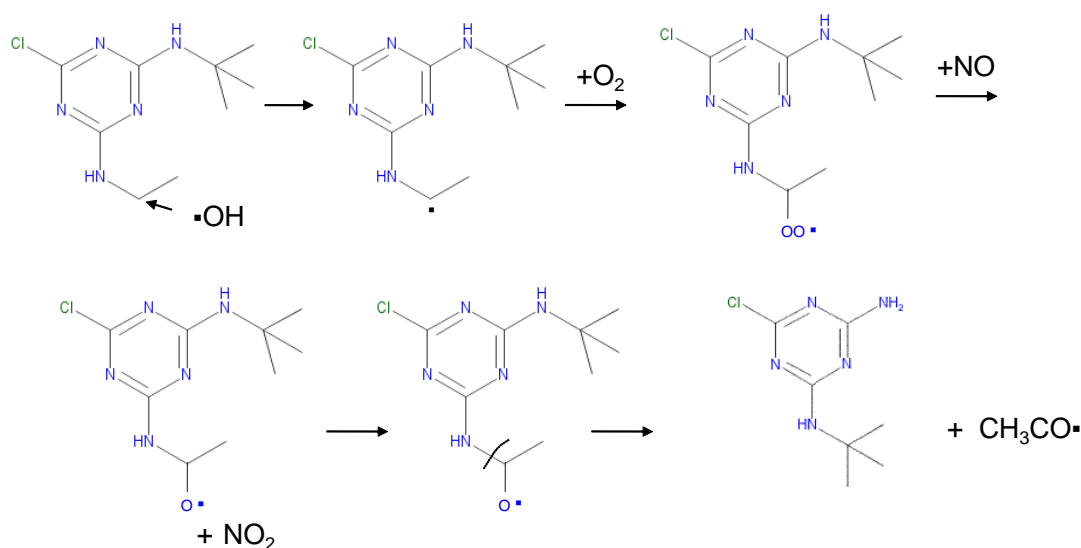


Figure 7.42 Possible reaction pathways to generate desethylterbutylazine from terbutylazine

7.10 Atmospheric implications

The rate constants obtained in this work were used to calculate the atmospheric lifetime towards reaction with OH radicals. Taking the OH concentration of $(9.4 \pm 1.3) \times 10^5$ molecule cm^{-3} (Prinn et al., 2001), and (as an over simplification) that the atmospheric lifetime towards OH radicals is given by: $\tau = 1/(k_{\text{OH}} \times C_{\text{OH}})$ of the Eley-Rideal theory, and by: $\tau = 1/k_{\text{obs}}^{\text{I}}$ according to the Langmuir-Hinshelwood mechanism (Finlayson-Pitts and Pitts Jr., 2000), the following half-lives at the three temperatures are obtained and summarized in table 7.7.

Table 7.7 Summary of parameters for the Langmuir-Hinshelwood and Eley-Rideal mechanism at different temperatures of the heterogeneous reaction of TBA with OH radical

Temperature (°C)	25	6.5	-10
$k_{\text{max}}^{\text{I}}$ (s^{-1})	$(9.24 \pm 0.84) \times 10^{-5}$	$(7.89 \pm 0.89) \times 10^{-5}$	$(4.33 \pm 0.38) \times 10^{-5}$
K_{OH} (cm^3)	$(9.4 \pm 1.6) \times 10^{-8}$	$(1.07 \pm 0.24) \times 10^{-7}$	$(1.40 \pm 0.26) \times 10^{-7}$
k_{OH} obtained from Eley-Rideal mechanism	$(8.6 \pm 1.2) \times 10^{-12}$	$(8.5 \pm 1.6) \times 10^{-12}$	$(6.08 \pm 0.97) \times 10^{-12}$
Half-life (h) (Eley-Rideal theory)	23.6	24.3	34.0
Half-life (h) (Langmuir-Hinshelwood theory)	25.6	26.3	38.1

In this study, the lifetimes calculated from the Langmuir-Hinshelwood and Eley-Rideal mechanisms have shown an agreement. Suppose the reaction with OH radicals is the main degradation pathway in the atmosphere, the average half-life of terbuthylazine is less than 2 days at room temperature. According to the Stockholm Convention, pesticides with a half-life of more than 2 days could be defined as POPs (Persistent Organic Pollutants). The modeling work also proves that terbuthylazine is not persistent in the atmosphere. The EUSES (Mackay-type) model gave a half-life of 41 hours of terbuthylazine in air (Beyer and Matthies, 2002). Results obtained from this study give the same conclusion as the gas phase reaction that TBA is not regarded as POP.

There are still discussions about the possibility of long-range transportation of

terbutylazine in the atmosphere. In field studies, Hüskes and Levsen (1997) have discovered higher concentrations of terbutylazine in rain water close to Hannover, and they concluded that there must be an additional local input from nearby application of the agent. Kreuger et al. (2006) also reported a detection of terbutylazine (0.061 µg/L in 2005) in Sweden, possibly from the application in Denmark.

Results at -10°C in this work have shown a half-life of more than 2 days, however, in the Stockholm Convention, the kinetic data are only considered at room temperature, so the results at -10°C are not relevant for the evaluation of long-range transport trend. Terbutylazine is not regarded as POP in the atmosphere.

8. Conclusions

The heterogeneous reaction of gas-phase OH radicals with aerosol-borne terbuthylazine has been investigated in a smog chamber at three different temperatures. Mixing of the aerosol and the OH-precursors is accelerated by a ventilator inside the chamber. When operating the chamber at 25 °C without cooling, the temperature change of air temperature inside the chamber was $\Delta T=7.8$ °C in the irradiated chamber. The temperature control of the cooling chamber minimizes this difference to 0.6 °C and 0.7 °C, at 6.5 °C and -10 °C, respectively, with the solar simulator switched on. The relative humidity is 22-28 % at 25 °C and saturated at 6.5 °C and -10 °C.

The concentrations of NO_x and ozone in the chamber are monitored during the experiments and establish a photostationary state (the Leighton ratio $[\text{NO}_2]/([\text{NO}][\text{O}_3])$) with a constant value at different temperatures: (0.64±0.28) at 25 °C, (0.56±0.10) at 6.5 °C and (0.10±0.04) at -10 °C.

Monodisperse SiO₂ particles were synthesized, which were used as carrier particles to be coated with terbuthylazine molecules. The particle structure was evaluated from scanning electron microscope images taken at the Bayreuther Institut für Makromolekülforschung at the Universität Bayreuth (BIMF), where the size and standard deviation of the particle diameter were determined to be 159.8 ± 5.0 nm. When the particles were injected into the chamber as a dilute aqueous suspension, a great portion of single particles existed in the smog chamber. This minimizes the impact of agglomeration and makes it easier to explain kinetic processes.

Using photolysis of methyl nitrite or the reaction of ozone with hydrazine as OH source, experiments on the reaction of gas-phase OH radicals with aerosol-borne terbuthylazine have been performed in the smog chamber. Results at 25 °C showed that the heterogeneous rate constant and OH concentration could be fitted to the Langmuir-Hinshelwood mechanism, which indicates that OH radicals have to be adsorbed to the particle surface before the chemical reaction with terbuthylazine can

take place. A fit to the Langmuir-Hinshelwood mechanism yields a gas-to-surface equilibrium constant K_{OH} for the OH radical of $(9.4 \pm 1.6) \times 10^{-7} \text{ cm}^3 \text{ molecule}^{-1}$ and a maximum rate constant k_{max}^1 of $(9.24 \pm 0.84) \times 10^{-5} \text{ s}^{-1}$. An estimate of the gas phase reactivity on self-synthesized SiO_2 particle, in which the Eley-Rideal mechanism is applicable, leads to $k_{\text{OH (Eley-Rideal)}} = (8.6 \pm 1.2) \times 10^{-12} \text{ cm}^3 \text{ molecule}^{-1} \text{ s}^{-1}$. This value is fairly close to the results from Palm et al. (1997) on Aerosil 200 ($k = (1.1 \pm 0.2) \times 10^{-11} \text{ cm}^3 \text{ molecule}^{-1} \text{ s}^{-1}$). Additional experimental results on Aerosil 200 from this work confirmed the trend of a kinetics following the Langmuir-Hinshelwood mechanism with Aerosil 200 particles at high OH concentrations. The results at 25 °C in this work have proved that the kinetics of heterogeneous reactions follows the Langmuir-Hinshelwood mechanism on self-synthesized SiO_2 particles and the Eley-Rideal mechanism on Aerosil 200 particles. The physical characteristics of the particles (e.g. surface area, state of aggregation) could have an impact on reaction mechanisms. In agreement with the previous study of Palm et al. (1997), desethylterbutylazine was identified by GC-MS.

Experiments were also performed at 6.5 °C and -10 °C. There is a slight temperature dependence of the kinetic parameters. By fitting an Arrhenius equation to the three data points, the activation energy E_a is calculated to be $(6.6 \pm 3.3) \text{ kJ mol}^{-1}$.

The half-life of terbutylazine in the atmosphere, based on results from this work, can be calculated to be less than 2 days at room temperature (both from Langmuir-Hinshelwood mechanism and Eley-Rideal mechanism). This result is consistent with the calculation results using kinetic data from the gas-phase. Terbutylazine is thus not defined as a POP (Persistent Organic Pollutants) in the sense of the Stockholm Convention.

References

- Alebić-Juretić, A., Cvitaš, T., Klasinc, L., 2000. Kinetics of heterogeneous ozone reactions. *Chemosphere* 41, 667–670.
- Alvarez, R.A., Moore, C.B., 1994. Quantum yield for production of CH₃NC in the photolysis of CH₃NCS. *Science* 263, 205–207.
- Ammann, M., Pöschl, U., Rudich, Y., 2003. Effects of reversible adsorption and Langmuir-Hinshelwood surface reactions on gas uptake by atmospheric particles. *Phys. Chem. Chem. Phys.* 5, 351–356.
- Anandan, S., Vinu, A., Sheeja Lovely, K.L.P., Gokulakrishnan, N., Srinivasu, P., Mori, T., Murugesan, V., Sivamarugan, V., Ariga, K., 2007. Photocatalytic activity of La-doped ZnO for the degradation of monocrotophos in aqueous suspension. *J. Mol. Catal. Chem.* 266, 149–157.
- Anderson, P.N., Hites, R.A., 1995. System to measure relative rate constants of semivolatile organic compounds with hydroxyl radicals. *Environ. Sci. Technol.* 30, 301–306.
- Anonymous, 2011. Conclusion on the peer review of the pesticide risk assessment of the active substance terbuthylazine. *Eur. Food Saf. Auth.* 9 (1); 1969.
- Atkinson, R., 1986. Kinetics and mechanisms of the gas-phase reactions of the hydroxyl radical with organic compounds under atmospheric conditions. *Chem. Rev.* 86, 69–201.
- Atkinson, R., 1989. Kinetics and mechanisms of the gas-phase reactions of the hydroxyl radical with organic compounds. *J. Phys. Chem. Ref. Data Monograph No. 1.*
- Atkinson, R., 1991. Kinetics of the gas-phase reactions of a series of organosilicon compounds with hydroxyl and nitrate (NO₃) radicals and ozone at 297±2 K. *Environ. Sci. Technol.* 25, 863–866.
- Atkinson, R., 1995. Gas phase tropospheric chemistry of organic compounds. In *Environmental Science and Technology*, Issue No. 4, R. E. Hester and R. M. Harrison (eds.). The Royal Society of Chemistry, Cambridge, UK.
- Atkinson, R., 2003. Kinetics of the gas-phase reactions of OH radicals with alkanes and cycloalkanes. *Atmos Chem Phys* 3, 2233–2307.
- Atkinson, R., Aschmann, S.M., 1985. Rate constants for the gas-phase reaction of hydroxyl radicals with biphenyl and the monochlorobiphenyls at 295±1 K. *Environ. Sci. Technol.* 19, 462–464.
- Atkinson, R., Baulch, D.L., Cox, R.A., Hampson Jr, R.F., Kerr, J.A., Rossi, M.J., Troe, J., 1997a. Evaluated kinetic and photochemical data for atmospheric chemistry: Supplement VI. *J. Phys. Chem. Ref. Data* 26, 1329–1499.
- Atkinson, R., Baulch, D.L., Cox, R.A., Hampson, R.F., Kerr, J.A., Rossi, M.J., Troe, J., 1997b. Evaluated kinetic, photochemical and heterogeneous data for atmospheric chemistry: supplement V. IUPAC Subcommittee on Gas Kinetic Data Evaluation for Atmospheric Chemistry. *J. Phys. Chem. Ref. Data* 26, 521–1011.
- Atkinson, R., Carter, W.P., 1984. Kinetics and mechanisms of the gas-phase reactions of ozone with organic compounds under atmospheric conditions. *Chem. Rev.* 84, 437–470.
- Atkinson, R., Guicherit, R., Hites, R. A., Palm, W.-U., Seiber, J. N. Seiber, de Voogt, P., 1999.

- Transformations of pesticides in the atmosphere: a state of the art. *Water. Air. Soil Pollut.* 115, 219–243.
- Barnet, P., Dommen, J., DeCarlo, P.F., Tritscher, T., Praplan, A.P., Platt, S.M., Prévôt, A.S.H., Donahue, N.M., Baltensperger, U., 2012. OH clock determination by proton transfer reaction mass spectrometry at an environmental chamber. *Atmospheric Meas. Tech.* 5, 647–656.
- Behnke, W., Nolting, F., Zetzsch, C., 1987a. A smog chamber study on the impact of aerosols on the photodegradation of chemicals in the troposphere. *J. Aerosol Sci.* 18, 65–71.
- Behnke, W., Nolting, F., Zetzsch, C., 1987b. The atmospheric fate of di (2-ethylhexyl-) phthalate, adsorbed on various metal oxide model aerosols and on coal fly ash. *J. Aerosol Sci.* 18, 849–852.
- Behnke, W., Holländer, W., Koch, W., Nolting, F., Zetzsch, C., 1988. A smog chamber for studies of the photochemical degradation of chemicals in the presence of aerosols. *Atmos. Environ.* 22, 1113–1120.
- Behnke, W., Zetzsch, C., 1989a. Über die Reaktivität von Lindan gegenüber OH-Radikalen (Forschungsvorhaben 93 3110/6). Umweltbundesamt, Berlin.
- Behnke, W., Zetzsch, C., 1989b. Heterogeneous photochemical formation of Cl atoms from NaCl aerosol, NO_x and ozone. *J. Aerosol Sci.* 20, 1167–1170.
- Bertram, A.K., Ivanov, A.V., Hunter, M., Molina, L.T., Molina, M.J., 2001. The reaction probability of OH on organic surfaces of tropospheric interest. *J. Phys. Chem. A* 105, 9415–9421.
- Beyer, A., Matthies, M., 2002. Criteria for atmospheric long-range transport potential and persistence of pesticides and industry chemicals. Erich Schmidt Verlag, Berlin.
- Bidleman, T.F., 1988. Atmospheric processes. *Environ. Sci. Technol.* 22, 361–367.
- Bidleman, T.F., 1999. Atmospheric transport and air-surface exchange of pesticides. *Water. Air. Soil Pollut.* 115, 115–166.
- Bidleman, T.F., Christensen, E.J., 1979. Atmospheric removal processes for high molecular weight organochlorines. *J. Geophys. Res. Oceans* 84, 7857–7862.
- Bidleman, T.F., Harner, T., 2000. Sorption to aerosols. In: D. Mackay and R. Boethling (eds.) *Estimating Chemical Properties for the Environmental and Health Sciences: A Handbook of Methods*. CRC Press, Florida.
- Bode, R., Ferch, H., Fratzscher, H., 1967. Basic characteristics of AEROSIL fumed silica, *Technical Bulletin Fine Particles* 11. *Kautsch.-Kunststoffe* 20, 578.
- Bongartz A., Kames J., Welter F., and Schurath U., 1991. Near-UV absorption cross sections and trans/cis equilibrium of nitrous acid, *J. Phys. Chem.* 95, 1076-1082.
- Borello, R., Pelizzetti, E., Serpone, N., Hidaka, H., 1989. Photocatalytic degradation of DDT mediated in aqueous semiconductor slurries by simulated sunlight. *Environ. Toxicol. Chem.* 8, 977–1002.
- Bossan, D., Wortham, H., Masclet, P., 1995. Atmospheric transport of pesticides adsorbed on aerosols I. Photodegradation in simulated atmosphere. *Chemosphere* 30, 21–29.
- Bowes, G.W., Jonkel, C.J., 1975. Presence and distribution of polychlorinated biphenyls (PCB) in arctic and subarctic marine food chains. *J. Fish. Res. Board Can.* 32, 2111–2123.
- Boyd-Boland, A.A., Magdic, S., Pawliszyn, J.B., 1996. Simultaneous determination of 60 pesticides in water using solid-phase microextraction and gas chromatography-mass

- spectrometry. *The Analyst* 121, 929.
- Brubaker, W.W., Hites, R.A., 1998. OH reaction kinetics of gas-phase α - and γ -hexachlorocyclohexane and hexachlorobenzene. *Environ. Sci. Technol.* 32, 766–769.
- Carter, W.P., Luo, D., Malkina, I.L., 1997. Investigation of the atmospheric reactions of chloropicrin. *Atmos. Environ.* 31, 1425–1439.
- Cherif, S., Wortham, H., 1997. A new laboratory protocol to monitor the volatilization of pesticides from soils. *Int. J. Environ. Anal. Chem.* 68, 199–212.
- Chernyak, S.M., Rice, C.P., McConnell, L.L., 1996. Evidence of currently-used pesticides in air, ice, fog, seawater and surface microlayer in the Bering and Chukchi Seas. *Mar. Pollut. Bull.* 32, 410–419.
- Cheskis, S., Derzy, I., Lozovsky, V.A., Kachanov, A., Romanini, D., 1998. Cavity ring-down spectroscopy of OH radicals in low pressure flame. *Appl. Phys. B* 66, 377–381.
- C.I.L. (Cluzeau Info Labo), 2005. Security Data of Pesticides, PCB, PBB, HPA. CD-Rom.
- Clough, P. N., Thrush, B. A., 1967. Mechanism of chemiluminescent reaction between nitric oxide and ozone, *Transactions of the Faraday Society*, 63, 915-925
- Cox, R.A., Fernandez, M.A., Symington, A., Ullerstam, M., Abbatt, J.P.D., 2005. A kinetic model for uptake of HNO₃ and HCl on ice in a coated wall flow system. *Phys. Chem. Chem. Phys.* 7, 3434.
- De Leeuw, F.A., 1993. Assessment of the atmospheric hazards and risks of new chemicals: Procedures to estimate “hazard potentials”. *Chemosphere* 27, 1313–1328.
- Eley, D.D., Rideal, E.K., 1941. The interchange of hydrogen in the adsorbed film on tungsten. *Proc. R. Soc.* 178, 452–464.
- Esteve, W., Budzinski, H., Villenave, E., 2006. Relative rate constants for the heterogeneous reactions of NO₂ and OH radicals with polycyclic aromatic hydrocarbons adsorbed on carbonaceous particles. Part 2: PAHs adsorbed on diesel particulate exhaust SRM 1650a. *Atmos. Environ.* 40, 201–21.
- European Food Safety Authority, 2011. Conclusion on the peer review of the pesticide risk assessment of the active substance terbuthylazine. *Efsa J.* 9, 133.
- Feigenbrugel, V., Person, A.L., Calvé, S.L., Mellouki, A., Muñoz, A., Wirtz, K., 2006. Atmospheric fate of dichlorvos: Photolysis and OH-initiated oxidation studies. *Environ. Sci. Technol.* 40, 850–857.
- Finlayson-Pitts, B.J., Pitts Jr., J.N., 2000. *Chemistry of the Upper and Lower Atmosphere*. Academic Press.
- Frank R., Klöpffer W., 1988. Spectral solar photon irradiance in Central Europe and the adjacent North Sea. *Chemosphere*, 17, 985-994
- Fritz, B., Lorenz, K., Steinert, W., Zellner, R., 1982. Laboratory kinetic investigations of the tropospheric oxidation of selected industrial emissions. In editors Versino B. & Ott H. *Phys.-Chem. Behav. Atmospheric Pollut. Dordr. edit, Reidel* 192–202.
- Fuchs, H., Dorn, H.-P., Bachner, M., Bohn, B., Brauers, T., Gomm, S., Hofzumahaus, A., Holland, F., Nehr, S., Rohrer, F., Tillmann, R., Wahner, A., 2012. Comparison of OH concentration measurements by DOAS and LIF during SAPHIR chamber experiments at high OH reactivity and low NO concentration. *Atmospheric Meas. Tech.* 5, 1611–1626.
- Gavrilov, R., 2007. Experimental and theoretical examination of the chemical kinetics of a pollutant coating on porous particles, PhD dissertation.

- Glotfelty, D.E., Leech, M.M., Jersey, J., Taylor, A.W., 1989. Volatilization and wind erosion of soil surface applied atrazine, simazine, alachlor, and toxaphene. *J. Agric. Food Chem.* 37, 546–551.
- Gregor, D.J., Gummer, W.D., 1989. Evidence of atmospheric transport and deposition of organochlorine pesticides and polychlorinated biphenyls in Canadian Arctic snow. *Environ. Sci. Technol.* 23, 561–565.
- Guicherit, R., Bakker, D.J., de Voogt, P., van den Berg, F., van Dijk, H.F.G., van Pul, W.A.J., 1999. Environmental risk assessment for pesticides in the atmosphere; the results of an international workshop. *Water. Air. Soil Pollut.* 115, 5–19.
- Guo, Y., Li, D., Hu, C., Wang, Y., Wang, E., Zhou, Y., Feng, S., 2001. Photocatalytic degradation of aqueous organochlorine pesticide on the layered double hydroxide pillared by Paratungstate A ion. *Appl. Catal. B Environ.* 30, 337–349.
- Hargrave, B.T., Vass, W.P., Erickson, P.E., Fowler, B.R., 1988. Atmospheric transport of organochlorines to the Arctic Ocean. *Tellus B* 40, 480–493.
- Harner, T., Kylin, H., Bidleman, T.F., Strachan, W.M.J., 1999. Removal of α - and γ -hexachlorocyclohexane and enantiomers of α -hexachlorocyclohexane in the Eastern Arctic Ocean. *Environ. Sci. Technol.* 33, 1157–1164.
- Hausmann, M., Brandenburger, U., Brauers, T., Dorn, H.-P., 1997. Detection of tropospheric OH radicals by long-path differential-optical-absorption spectroscopy: Experimental setup, accuracy, and precision. *J. Geophys. Res. Atmospheres* 102, 16011–16022.
- Hebert, V.R., Geddes, J.D., Mendosa, J., Miller, G.C., 1998. Gas-phase photolysis of phorate, a phosphorothioate insecticide. *Chemosphere* 36, 2057–2066.
- Herrmann, J.M., Guillard, C., Arguello, M., Agüera, A., Tejedor, A., Piedra, L., Fernandez-Alba, A., 1999. Photocatalytic degradation of pesticide pirimiphos-methyl: Determination of the reaction pathway and identification of intermediate products by various analytical methods. *Catal. Today* 54, 353–367.
- Hinshelwood, C.N., 1940. *The Kinetics of Chemical Change*, 1st edition. ed. Oxford Clarendon Press.
- Hoferkamp, L., Hermanson, M.H., Muir, D.C.G., 2010. Current use pesticides in Arctic media; 2000–2007. *Sci. Total Environ.* 408, 2985–2994.
- Howard, P.H., 1991. *Handbook of Environmental Degradation Rates*. Lewis Publishers.
- Hung, H., Blanchard, P., Halsall, C.J., Bidleman, T.F., Stern, G.A., Fellin, P., Muir, D.C.G., Barrie, L.A., Jantunen, L.M., Helm, P.A., Ma, J., Konoplev, A., 2005. Temporal and spatial variabilities of atmospheric polychlorinated biphenyls (PCBs), organochlorine (OC) pesticides and polycyclic aromatic hydrocarbons (PAHs) in the Canadian Arctic: Results from a decade of monitoring. *Sci. Total Environ.* 342, 119–144.
- Iwata, H., Tanabe, S., Sakai, N., Tatsukawa, R., 1993. Distribution of persistent organochlorines in the oceanic air and surface seawater and the role of ocean on their global transport and fate. *Environ. Sci. Technol.* 27, 1080–1098.
- Jeffries, H., Fox, D., Kamens, R., 1976. Outdoor smog chamber studies: light effects relative to indoor chambers. *Environ. Sci. Technol.* 10, 1006–1011.
- Jenny, B., Pichat, P., 1991. Determination of the actual photocatalytic rate of hydrogen peroxide decomposition over suspended titania. Fitting to the Langmuir-Hinshelwood form. *Langmuir* 7, 947–954.

- Junge, C.F., 1977. Fate of pollutants in the air and water environment. In: Suffet, I.H. (Ed.), *Basic Considerations about Trace Constituents in the Atmosphere as Related to the Fate of Global Pollutants*. Wiley, New York.
- Junkermann, W., Platt, U., and Volz-Thomas, A., 1998. A photoelectric detector for the measurement of photolysis frequencies of ozone and other atmospheric molecules, *J. Atmos. Chem.* 8, 203–22
- of photolysis frequencies of ozone and other atmospheric molecules, *J. Atmos. Chem.* 8, 203–227.
- Kahan, T.F., Kwamena, N.-O.A., Donaldson, D.J., 2006. Heterogeneous ozonation kinetics of polycyclic aromatic hydrocarbons on organic films. *Atmos. Environ.* 40, 3448–3459.
- Klöppel, H., Kördel, W., 1997. Pesticide volatilization and exposure of terrestrial ecosystems. *Chemosphere* 35, 1271–1289.
- Konstantinou, I.K., Albanis, T.A., 2004. TiO₂-assisted photocatalytic degradation of azo dyes in aqueous solution: kinetic and mechanistic investigations: A review. *Appl. Catal. B Environ.* 49, 1–14.
- Kreuger, J., Adielsson, S., Kylin, H., 2006. Monitoring of pesticides in atmospheric deposition in Sweden 2002–2005. Rep. Swed. Environ. Prot. Agency Contract No 211 0543 Uppsala.
- Krüger, H.-U., 2001. Unpublished data of results for filter experiments of terbuthylazine with OH radicals.
- Kwamena, N.-O.A., Earp, M.E., Young, C.J., Abbatt, J.P.D., 2006. Kinetic and product yield study of the heterogeneous gas-surface reaction of anthracene and ozone. *J. Phys. Chem. A* 110, 3638–3646.
- Kwamena, N.-O.A., Thornton, J.A., Abbatt, J.P.D., 2004. Kinetics of surface-bound benzo[*a*]pyrene and ozone on solid organic and salt aerosols. *J. Phys. Chem. A* 108, 11626–11634.
- Kwok, E.S., Atkinson, R., Arey, J., 1992. Gas-phase atmospheric chemistry of selected thiocarbamates. *Environ. Sci. Technol.* 26, 1798–1807.
- Kwok, E.S., Atkinson, R., Arey, J., 1995. Rate constants for the gas-phase reactions of the OH radical with dichlorobiphenyls, 1-chlorodibenzo-*p*-dioxin, 1, 2-dimethoxybenzene, and diphenyl ether: estimation of OH radical reaction rate constants for PCBs, PCDDs, and PCDFs. *Environ. Sci. Technol.* 29, 1591–1598.
- Kwok, E.S.C., Atkinson, R., 1995. Estimation of hydroxyl radical reaction rate constants for gas-phase organic compounds using a structure-reactivity relationship: an update. *Atmos. Environ.* 29, 1685–1695.
- Lammel, G., Cape, J. N., 1996. Nitrous acid and nitrite in the atmosphere. *Chem. Soc. Rev.* 25, 361–369.
- Langmuir, I., 1918. The adsorption of gases on plane surfaces of glass, mica and platinum. *J. Am. Chem. Soc.* 40, 1361–1403.
- Le Person, A., Mellouki, A., Muñoz, A., Borrás, E., Martín-Reviejo, M., Wirtz, K., 2007. Trifluralin: Photolysis under sunlight conditions and reaction with HO· radicals. *Chemosphere* 67, 376–383.
- Leighton, P.A., 1961. *Photochemistry of air pollution*. Academic Press, New York.
- Leu, M.-T., 1988. Heterogeneous reactions of N₂O₅ with H₂O and HCl on ice surfaces: Implications for Antarctic ozone depletion. *Geophys. Res. Lett.* 15, 851–854.
- Li, J., Zhu, T., Wang, F., Qiu, X.H., Lin, W.L., 2006. Observation of organochlorine pesticides in

- the air of the Mt. Everest region. *Ecotoxicol. Environ. Saf.* 63, 33–41.
- Lin, S.-S., Gurol, M.D., 1998. Catalytic decomposition of hydrogen peroxide on iron oxide: kinetics, mechanism, and implications. *Environ. Sci. Technol.* 32, 1417–1423.
- Majewski, M.S., Foreman, W.T., Goolsby, D.A., Nakagaki, N., 1998. Airborne pesticide residues along the Mississippi River. *Environ. Sci. Technol.* 32, 3689–3698.
- Marinas, A., Guillard, C., Marinas, J.M., Fernández-Alba, A., Aguëra, A., Herrmann, J.-M., 2001. Photocatalytic degradation of pesticide–acaricide formetanate in aqueous suspension of TiO₂. *Appl. Catal. B Environ.* 34, 241–252.
- Meylan W (1999) EPIWIN x3.04 [computer program: US EPA Version for Windows], Syracuse Research Corporation, Syracuse, NY, US. <http://esc.syrres.com/interkow/epi.htm>. (June 22, 2002)
- Meijer, G., Boogaarts, M.G., Jongma, R.T., Parker, D.H., Wodtke, A.M., 1994. Coherent cavity ring down spectroscopy. *Chem. Phys. Lett.* 217, 112–116.
- Miet, K., Le Menach, K., Flaud, P.M., Budzinski, H., Villenave, E., 2009. Heterogeneous reactions of ozone with pyrene, 1-hydroxypyrene and 1-nitropyrene adsorbed on particles. *Atmos. Environ.* 43, 3699–3707.
- Mills, G., Hoffmann, M.R., 1993. Photocatalytic degradation of pentachlorophenol on titanium dioxide particles: identification of intermediates and mechanism of reaction. *Environ. Sci. Technol.* 27, 1682–1689.
- Mmerek, B.T., Donaldson, D.J., Gilman, J.B., Eliason, T.L., Vaida, V., 2004. Kinetics and products of the reaction of gas-phase ozone with anthracene adsorbed at the air–aqueous interface. *Atmos. Environ.* 38, 6091–6103.
- Mongar, K., Miller, G.C., 1988. Vapor phase photolysis of trifluralin in an outdoor chamber. *Chemosphere* 17, 2183–2188.
- Munthe, J., Palm, A., 2003. *Towards Cleaner Air for Europe - Science, Tools and Applications, Part 2: Overviews from the Final Reports of the EUROTRAC-2 Subprojects*, P. Midgley & M. Reuther (Eds.). Margraf Publishers.
- Nash, R.G., Gish, T.J., 1989. Halogenated pesticide volatilization and dissipation from soil under controlled conditions. *Chemosphere* 18, 2353–2362.
- Net, S., Nieto-Gligorovski, L., Gligorovski, S., Wortham, H., 2010. Heterogeneous ozonation kinetics of 4-phenoxyphenol in the presence of photosensitizer. *Atmos Chem Phys* 10, 1545–1554.
- Nolting, F., Behnke, W., Zetzsch, C., 1988. A smog chamber for studies of the reactions of terpenes and alkanes with ozone and OH. *J. Atmospheric Chem.* 6, 47–59.
- Norstrom, R.J., Simon, M., Muir, D.C., Schweinsburg, R.E., 1988. Organochlorine contaminants in Arctic marine food chains: identification, geographical distribution and temporal trends in polar bears. *Environ. Sci. Technol.* 22, 1063–1071.
- Oehme, M., Haugen, J.-E., Schlabach, M., 1996. Seasonal changes and relations between levels of organochlorines in Arctic ambient air: first results of an all-year-round monitoring program at Ny-Ålesund, Svalbard, Norway. *Environ. Sci. Technol.* 30, 2294–2304.
- Okitsu, K., Iwasaki, K., Yobiko, Y., Bandow, H., Nishimura, R., Maeda, Y., 2005. Sonochemical degradation of azo dyes in aqueous solution: a new heterogeneous kinetics model taking into account the local concentration of OH radicals and azo dyes. *Ultrason. Sonochem.* 12, 255–262.

- Orzechowska, G.E., Paulson, S.E., 2005. Photochemical sources of organic acids. 1. reaction of ozone with isoprene, propene, and 2-butenes under dry and humid conditions using SPME. *J. Phys. Chem. A* 109, 5358–5365.
- Palm, W.-U., Elend, M., Krueger, H.-U., Zetzsch, C., 1997. OH radical reactivity of airborne terbuthylazine adsorbed on inert aerosol. *Environ. Sci. Technol.* 31, 3389–3396.
- Palm, W.-U., Elend, M., Krüger, H.-U., Zetzsch, C., 1999. Atmospheric degradation of a semivolatile aerosol-borne pesticide: Reaction of OH with pyrifenoxy (an oxime-ether), adsorbed on SiO₂. *Chemosphere* 38, 1241–1252.
- Palm, W.-U., Millet, M., Zetzsch, C., 1998. OH radical reactivity of pesticides adsorbed on aerosol materials: first results of experiments with filter samples. *Ecotoxicol. Environ. Saf.* 41, 36–43.
- Pankow, J.F., 1987. Review and comparative analysis of the theories on partitioning between the gas and aerosol particulate phases in the atmosphere. *Atmospheric Environ.* 1967 21, 2275–2283.
- Pankow, J.F., Storey, J.M., Yamasaki, H., 1993. Effects of relative humidity on gas/particle partitioning of semivolatile organic compounds to urban particulate matter. *Environ. Sci. Technol.* 27, 2220–2226.
- Payne, N.J., Thompson, D.G., 1992. Off-target glyphosate deposits from aerial silvicultural applications under various meteorological conditions. *Pestic. Sci.* 34, 53–59.
- Perraudin, E., Budzinski, H., Villenave, E., 2006. Kinetic study of the reactions of ozone with polycyclic aromatic hydrocarbons adsorbed on atmospheric model particles. *J. Atmospheric Chem.* 56, 57–82.
- Peterle, T.J., 1969. DDT in antarctic snow. *Nature* 224, 620.
- Pflieger, M., Monod, A., Wortham, H., 2009. Kinetic study of heterogeneous ozonolysis of alachlor, trifluralin and terbuthylazine adsorbed on silica particles under atmospheric conditions. *Atmos. Environ.* 43, 5597–5603.
- Pflieger, M., Grgić, I., Kitanovski, Z., Nieto, L., Wortham, H., 2011. The heterogeneous ozonation of pesticides adsorbed on mineral particles: Validation of the experimental setup with trifluralin. *Atmos. Environ.* 45, 7127–7134.
- Pflieger, M., Grgić, I., Kitanovski, Z., 2012. Ozonation of isoproturon adsorbed on silica particles under atmospheric conditions. *Atmos. Environ.* 61, 40–47.
- Pflieger, M., Monod, A., Wortham, H., 2013. Heterogeneous oxidation of terbuthylazine by “dark” OH radicals under simulated atmospheric conditions in a flow tube. *Environ. Sci. Technol.*, 47, 6239–6246.
- Pitts Jr., J.N., Paur, H.-R., Zielinska, B., Arey, J., Winer, A.M., Ramdahl, T., Mejia, V., 1986. Factors influencing the reactivity of polycyclic aromatic hydrocarbons adsorbed on filters and ambient POM with ozone. *Chemosphere* 15, 675–685.
- Pöschl, U., Letzel, T., Schauer, C., Niessner, R., 2001. Interaction of ozone and water vapor with spark discharge soot aerosol particles coated with benzo[a]pyrene: O₃ and H₂O adsorption, benzo[a]pyrene degradation, and atmospheric implications. *J Phys Chem* 105, 4029–4041.
- Prinn, R.G., Huang, J., Weiss, R.F., Cunnold, D.M., Fraser, P.J., Simmonds, P.G., McCulloch, A., Harth, C., Salameh, P., O’Doherty, S., Wang, R.H.J., Porter, L., Miller, B.R., 2001. Evidence for substantial variations of atmospheric hydroxyl radicals in the past two

- decades. *Science* 292, 1882–1888.
- Quan, X., Niu, J., Chen, S., Chen, J., Zhao, Y., Yang, F., 2003. Effects of Fe₂O₃, organic matter and carbonate on photocatalytic degradation of lindane in the sediment from the Liao River, China. *Chemosphere* 52, 1749–1755.
- Rice, C.P., Chernyak, S.M., 1997. Marine Arctic fog: an accumulator of currently used pesticide. *Chemosphere* 35, 867–878.
- Rohrer, F., Brüning, D., Grobler, E.S., Weber, M., Ehhalt, D.H., Neubert, R., Schüßler, W., Levin, I., 1998. Mixing ratios and photostationary state of NO and NO₂ observed during the POPCORN field campaign at a rural site in Germany. *J. Atmospheric Chem.* 31, 119–137.
- Sander S.P., Friedl R.R., Golden D.M., Kurylo M.J., Huie R.E., Orkin V.L., Moortgat G.K., Ravishankara A.R., Kolb C.E., Molina M.J., and Finlayson-Pitts B.J., 2002. Chemical Kinetics and Photochemical Data for Use in Atmospheric Studies. Evaluation Number 14, JPL Publication 02-25, Jet Propulsion Laboratory, Pasadena.
- Sanusi, A., Millet, M., Mirabel, P., Wortham, H., 1999. Gas–particle partitioning of pesticides in atmospheric samples. *Atmos. Environ.* 33, 4941–4951.
- Sanusi, A., Millet, M., Mirabel, P., Wortham, H., 2000. Comparison of atmospheric pesticide concentrations measured at three sampling sites: local, regional and long-range transport. *Sci. Total Environ.* 263, 263–277.
- Sauer, T., Cesconeto Neto, G., Jose, H.J., Moreira, R., 2002. Kinetics of photocatalytic degradation of reactive dyes in a TiO₂ slurry reactor. *J. Photochem. Photobiol. Chem.* 149, 147–154.
- Sauret, N., Wortham, H., Putaud, J.-P., Mirabel, P., 2008. Study of the effects of environmental parameters on the gas/particle partitioning of current-use pesticides in urban air. *Atmos. Environ.* 42, 544–553.
- Scheringer, M., Salzmann, M., Stroebe, M., Wegmann, F., Fenner, K., Hungerbühler, K., 2004. Long-range transport and global fractionation of POPs: insights from multimedia modeling studies. *Environ. Pollut.* 128, 177–188.
- Schlosser, E., Brauers, T., Dorn, H.-P., Fuchs, H., Häsel, R., Hofzumahaus, A., Holland, F., Wahner, A., Kanaya, Y., Kajii, Y., 2009. Technical Note: Formal blind intercomparison of OH measurements: results from the international campaign HOxComp. *Atmospheric Chem. Phys.* 9, 7923–7948.
- Segal-Rosenheimer, M., Dubowski, Y., 2007. Heterogeneous ozonolysis of cypermethrin using real-time monitoring FTIR techniques. *J. Phys. Chem. C* 111, 11682–11691.
- Sladen, W.J.L., Menzie, C.M., Reichel, W.L., 1966. DDT residues in adelic penguins and a crabeater seal from Antarctica. *Nature* 210, 670–671.
- Sobczyński, A., Duczmal, Ł., Zmudziński, W., 2004. Phenol destruction by photocatalysis on TiO₂: an attempt to solve the reaction mechanism. *J. Mol. Catal. Chem.* 213, 225–230.
- Sørensen, M., Hurley, M., Wallington, T., Dibble, T., Nielsen, O., 2002. Do aerosols act as catalysts in the OH radical initiated atmospheric oxidation of volatile organic compounds? *Atmos. Environ.* 36, 5947–5952.
- Stöber, W., Fink, A., 1968. Controlled growth of monodisperse silica spheres in the micron size range. *J. Colloid Interface Sci.* 26, 62–69.
- Sun, F., Zhu, T., Shang, J., Han, L., 2005. Gas-phase reaction of dichlorvos, carbaryl, chlordimeform, and 2, 4-D butyl ester with OH radicals. *Int. J. Chem. Kinet.* 37, 755–762.

- Sun, Y., Pignatello, J.J., 1995. Evidence for a surface dual hole-radical mechanism in the titanium dioxide photocatalytic oxidation of 2, 4-D. *Environ. Sci. Technol.* 29, 2065–2072.
- Tatton, J.O., Ruzicka, J.H.A., 1967. Organochlorine pesticides in Antarctica. *Nature* 215, 346–348.
- Taylor W.D., Allston T.D., Moscato M.J., Fazekas G.B., Koslowski R., and Takacs G.A., 1980. Atmospheric photodissociation lifetimes for nitromethane, methyl nitrite, and methyl nitrate, *Int. J. Chem. Kinet.* 12, 231-240.
- Tolbert, M.A., Rossi, M.J., Golden, D.M., 1988. Antarctic ozone depletion chemistry: Reactions of N₂O₅ with H₂O and HCl on ice surfaces. *Science* 240, 1018–1021.
- Tuazon, E.C., Atkinson, R., Aschmann, S.M., Arey, J., Winer, A.M., Pitts, J.N., 1986. Atmospheric loss processes of 1, 2-dibromo-3-chloropropane and trimethyl phosphate. *Environ. Sci. Technol.* 20, 1043–1046.
- Tuazon, E.C., Atkinson, R., Aschmann, S.M., Goodman, M.A., Winer, A.M., 1988. Atmospheric reactions of chloroethenes with the OH radical. *Int. J. Chem. Kinet.* 20, 241–265.
- Tuazon, E.C., Carter, W.P., Atkinson, R., Pitts, J.N., 1983. The gas-phase reaction of hydrazine and ozone: A nonphotolytic source of OH radicals for measurement of relative OH radical rate constants. *Int. J. Chem. Kinet.* 15, 619–629.
- Tuazon, E.C., Carter, W.P., Winer, A.M., Pitts Jr., J.N., 1981. Reactions of hydrazines with ozone under simulated atmospheric conditions. *Environ. Sci. Technol.* 15, 823–828.
- Turchi, C.S., Ollis, D.F., 1990. Photocatalytic degradation of organic water contaminants: mechanisms involving hydroxyl radical attack. *J. Catal.* 122, 178–192.
- Ung, A.-M., 1974. The photolysis of water vapor at 1470 Å. H₂ production in the primary process. *Chem. Phys. Lett.* 28, 603–607.
- Van den Berg, F., Kubiak, R., Benjey, W.G., Majewski, M.S., Yates, S.R., Reeves, G.L., Smelt, J.H., van der Linden, A.M.A., 1999. Emission of pesticides into the air. *Water. Air. Soil Pollut.* 115, 195–218.
- Van Pul, W.A.J., Bidleman, T.F., Brorström-Lundén, E., Builtjes, P.J.H., Dutchak, S., Duyzer, J.H., Gryning, S.-E., Jones, K.C., van Dijk, H.F.G., van Jaarsveld, J. H. A., 1999. Atmospheric transport and deposition of pesticides: an assessment of current knowledge. *Water. Air. Soil Pollut.* 115, 245–256.
- Vlasenko, A., George, I.J., Abbatt, J.P.D., 2008. Formation of volatile organic compounds in the heterogeneous oxidation of condensed-phase organic films by gas-phase OH. *J. Phys. Chem. A* 112, 1552–1560.
- Voigt, S., Orphal J., Bogumil, K. and Burrows J.P., 2001. The temperature dependence (203-293 K) of the absorption cross sections of O₃ in the 230-850 nm region measured by Fourier-transform spectroscopy, *J. Photochem. Photobiol. A: Chem.* 143, 1-9
- Wania, F., Mackay, D., 1996. Tracking the distribution of persistent organic pollutants. *Environ. Sci. Technol.* 30, 390–396.
- Welch, H.E., Muir, D.C., Billeck, B.N., Lockhart, W.L., Brunskill, G.J., Kling, H.J., Olson, M.P., Lemoine, R.M., 1991. Brown snow: a long-range transport event in the Canadian Arctic. *Environ. Sci. Technol.* 25, 280–286.
- Woodrow, J.E., Crosby, D.G., Mast, T., Moilanen, K.W., Seiber, J.N., 1978. Rates of transformation of trifluralin and parathion vapors in air. *J. Agric. Food Chem.* 26, 1312–1316.

- Yamasaki, H., Kuwata, K., Miyamoto, H., 1982. Effects of ambient temperature on aspects of airborne polycyclic aromatic hydrocarbons. *Environ. Sci. Technol.* 16, 189–194.
- Yang, B., Zhang, Y., Meng, J., Gan, J., Shu, J., 2010. Heterogeneous reactivity of suspended pirimiphos-methyl particles with ozone. *Environ. Sci. Technol.* 44, 3311–3316.

Appendix 1

LIST OF ABBREVIATIONS AND SYMBOLS

Latin Symbols

Symbol	Meaning	Unit
A	concentration of SOC in particle phase	ng.m^{-3}
C	concentration	mol L^{-1}
C_{Ae}	aerosol concentration in smog chamber	mg cm^{-3}
C_{AS}	surface concentrations of sites occupied by A	m^{-2}
C_{BS}	surface concentrations of sites occupied by B	m^{-2}
C_{HC}	concentration of hydrocarbon at different time	molecule cm^{-3}
C_{p}	accumulative particle concentration at time t	cm^{-3}
C_{OH}	gas-phase OH radical concentration	molecule cm^{-3}
C_{s}	total number of sites on particle surface	molecule m^{-2}
$C_{\text{TBA(ads)}}$	adsorption state concentration of terbuthylazine	molecule m^{-2}
D	diameter of a particle	nm
D_{SiO_2}	diameter of SiO_2 particle	nm
d_{V}	dilution factor of the smog chamber	/
F	concentration of SOC in gas phase	ng m^{-3}
F_{TBA}	mass fraction of TBA on the aerosol	/
[HC]	hydrocarbon peak area	mV s
J_{NO_2}	photolysis frequency of NO_2	s^{-1}
k	reaction rate constant on surface	$\text{m}^2 \text{s}^{-1}$
k_{A}	adsorption rate of A	$\text{m}^2 \text{s}^{-1}$
$k_{\text{A}'}$	desorption rate of A	$\text{m}^2 \text{s}^{-1}$
k_{dilution}	the loss rate by dilution	s^{-1}
$k_{(\text{NO}+\text{O}_3)}$	temperature-dependent rate constant for the reaction between NO and O_3	$\text{ppb}^{-1} \text{s}^{-1}$
k_{NO_3}	NO_3 rate constant	$\text{cm}^3 \text{molecule}^{-1} \text{s}^{-1}$
k_{OH}	second order reaction rate constant for the reaction with OH radicals	$\text{cm}^3 \text{molecule}^{-1} \text{s}^{-1}$
k_{other}	loss of hydrocarbons caused by other processes	s^{-1}

k_{O_3}	O ₃ rate constant	cm ³ molecule ⁻¹ s ⁻¹
K_{O_3}	ozone gas-to-surface equilibrium constant	cm ³ molecule ⁻¹
k_{\max}^I	maximum rate constant	s ⁻¹
k_{obs}^I	experimental pseudo-first-order rate constant	s ⁻¹
k_{OH}	OH rate constant	cm ³ molecule ⁻¹ s ⁻¹
k_{OH} (Eley-Rideal)	second order rate constant with OH radical according to the Eley-Rideal mechanism	cm ³ molecule ⁻¹ s ⁻¹
K_{OH}	OH radical gas-to-surface equilibrium constant	cm ³ molecule ⁻¹
K_p	gas/particle partitioning coefficient	m ³ μg ⁻¹
k_{photo}	photolysis rate	s ⁻¹
k_{sedi}	sedimentation rate of particles	s ⁻¹
m	mass of the particle	g
m_f	aerosol mass collected on the filter	mg
$m_{\text{HC, solid}}$	measured mass for solid hydrocarbon	mg
M_{HC}	molar mass of hydrocarbon	g mol ⁻¹
N	number of molecules	molecule
N_A	the Avogadro constant	6.02×10 ²³ mol ⁻¹
[OH]	concentration of OH radicals	cm ⁻³
[Ozone]	ozone concentration	cm ⁻³
P	pressure	Pa
[PFH]	perfluorohexane peak area	mV s
r	reaction rate on surface	m ⁻² s ⁻¹
R_{TBA}	radius of plane circle of TBA molecule	nm
SA	surface area of a particle	m ² g ⁻¹
$S_{\text{SiO}_2\text{particle}}$	spherical area of SiO ₂ particle	nm ²
t	time	h
T	temperature	K
TSP	total concentration of suspended particles	μg m ⁻³
τ	half-life	h
V	volume	L
V_{dil}	the sampling volume which caused the dilution	L
V_f	the volume of air which was taken for the filter sampling	cm ⁻³
$V_{\text{HC, liquid}}$	liquid volume for the gas storage container	μL
X	the fraction of available sites	/

Greek symbols

Symbol	Meaning	Unit
Δ	difference	/
θ	surface coverage	/
$\rho_{\text{HC, liquid}}$	density of liquid hydrocarbon	g cm^{-3}
τ	half-life	hour
Φ	diameter of SiO_2 particle	nm

Superscripts

'	interpolated value
---	--------------------

Subscripts

Ae	aerosol
i	time point
norm	normalized value
particle	particles in the smog chamber
0	value at initial time the experiment started

Appendix 2

● GC-FID calibration process

The GC-FID for gas phase compound detection should be calibrated when the glass-lined tube is changed. Gases from the storage container were added into the smog chamber at volumes of 5mL, 5 mL, 10 mL, 10 mL, 10 mL, 10 mL. The peak areas at different concentrations were plotted versus concentration and the linear regression line gives the information of the sensitivity of FID.

Table I. Parameter for GC-FID calibration

Parameter		Comment
Oven temperature	190 °C	isothermal
Detector temperature	220 °C	
Injector temperature	-	important only when liquid sample is added directly
Column	Al ₂ O ₃ -PLOT Chrompack, 50m length; inner diameter 0.32mm	H ₂ 1.4 bar, air 2 bar, pump: 335, capillary flow: 9.30 mL/min
Carrier gas	He 3.0 bar	

Table II. Retention time of hydrocarbon

Species	Retention time / min
PFH	3.828
2,2-Dimethylbutane	4.171
2,2,4-Trimethylpentane	13.001
Tetramethylbutane	14.438
Toluene	22.691

Table III. Preparation of gas storage container

Gas storage container	
PFH	45 µl
2,2-Dimethylbutane	24.5 µl
2,2,4-Trimethylpentane	37.0 µl
Tetramethylbutane	24.60 mg
Toluene	30 µl

Table IV. Amount in the Smog chamber

Volume from the gas storage container	Concentration in the smog chamber	Species
50 mL	60 ppb	PFH
50 mL	60 ppb	2,2-Dimethylbutane
50 mL	60 ppb	2,2,4-Trimethylpentane
50 mL	76 ppb	Tetramethylbutane
50 mL	58 ppb	Toluene

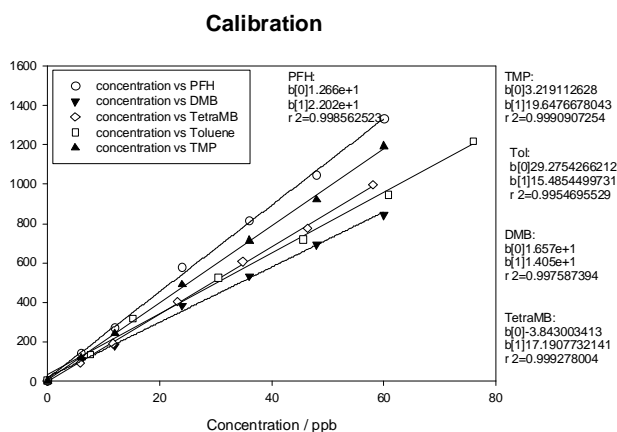


Figure I. FID peak area versus concentration for hydrocarbons

● **Program for the cold trap injector:**

0-1 minutes: pump chamber air to flush the glass-lined tube

1-2 minutes: pump stops, liquid nitrogen cooling starts

2-3.9 minutes: pump chamber air through the glass lined tube and the hydrocarbons are collected inside the glass-line tube during the cooling procedure by liquid nitrogen

3.9-4.5 minutes: pump stops, cooling is continued to maintain the collected hydrocarbons

4.5-4.55 minutes: electronic heating of the glass-lined tube starts, the magnetic valves turn on and the carrier gas (He) flush the previously condensed hydrocarbons into the GC column.

Parameters and results for EFTEM:

TEM was performed in bright-field mode with a Zeiss CEM902 EFTEM (energy filtering transmission electron microscope) operated at 80kV. The samples were prepared by placing one drop of a chloroform / particle mixture onto a carbon-coated copper grid. The solvent was allowed to evaporate. All micrographs were recorded with a CCD camera (Megaview III and iTEM software, Olympus-SiS, Münster).

The particle size were measured using Olympus MeasureIT software and labeled directly in the image. The average diameter of the self-synthesized particles is 159.8 ± 5.0 nm.

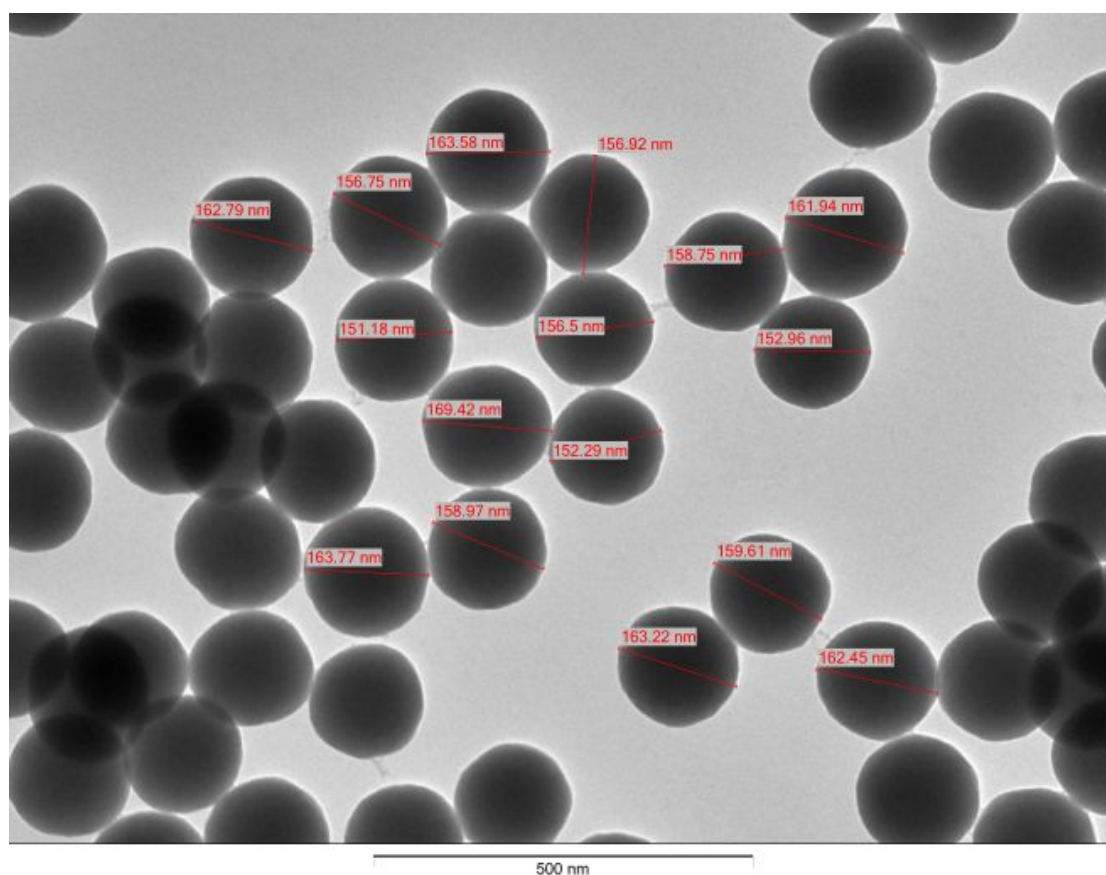
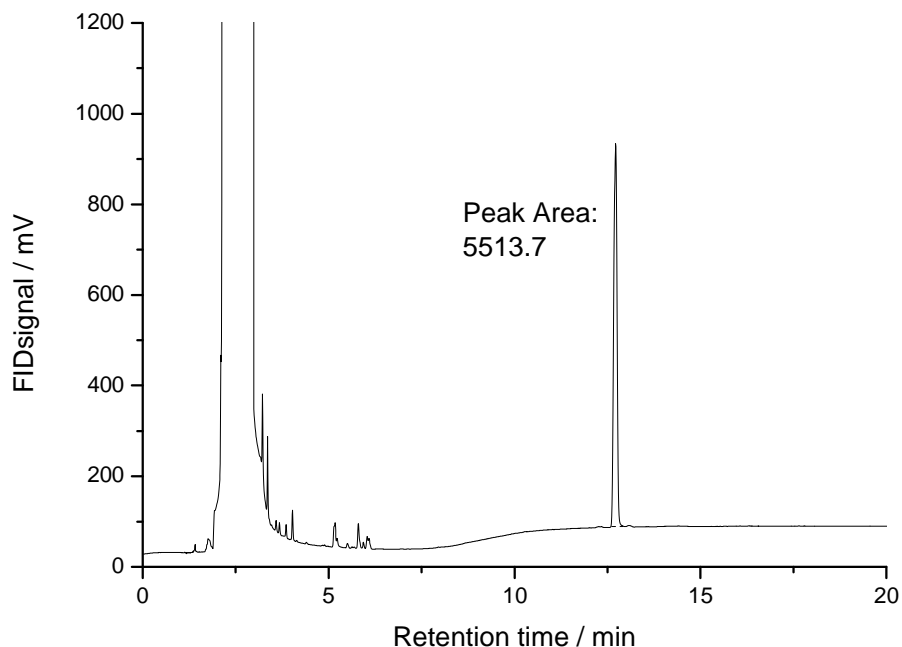


Figure II. EFTEM image of the self-synthesized SiO₂ particles

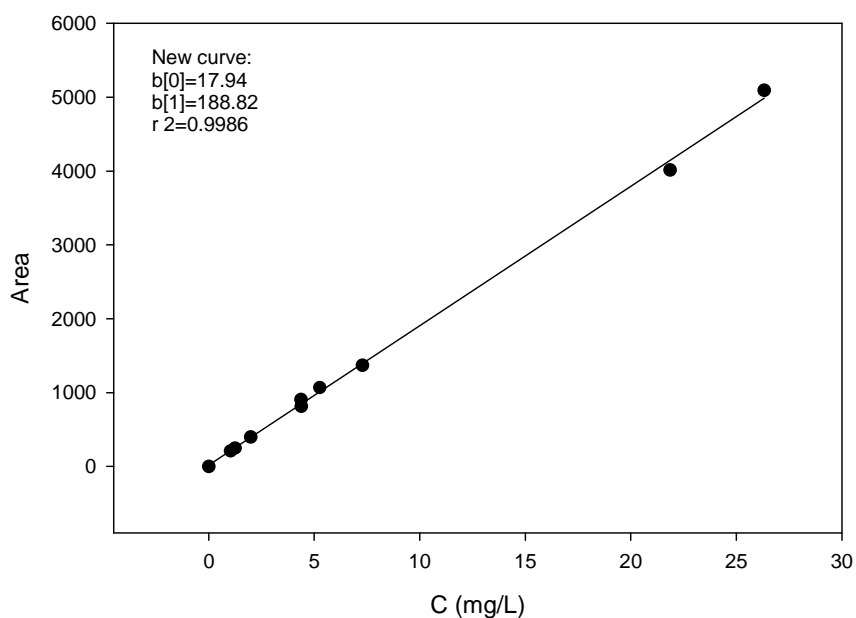
● Calculation of coating efficiency during the aerosol coating

process:



Chromatogram of GC-FID for filter sample test on D111212

Standard Curve of TBA/CH₂Cl₂



Based on the standard curve above: $\text{Area} = 17.94 + 188.82 \times C$, C is then calculated as 29.11 mg/L.

The mass fraction of terbuthylazine is calculated as below:

$$F = \frac{m_{\text{TBA}}}{m_{\text{aerosol}}} = \frac{29.11 \text{ mg/L} \times 1 \text{ mL}}{0.6742 \text{ mg} - 29.11 \text{ mg/L} \times 1 \text{ mL}} = 0.045$$

- **Experimental raw data:**

The experimental raw data have been uploaded to the data base of Eurochamp2

http://eurochamp-database.es/Eurocha_data/index.php?table_name=data_records&function=search&where_clause=&page=19&order=EXP_date&order_type=ASC

Erklärung

Hiermit erkläre ich, dass ich die vorliegende Arbeit selbstständig und ohne unerlaubte fremde Hilfe angefertigt habe. Ich habe keine anderen als die angeführten Quellen benutzt. Sämtliche Textstellen, die wörtlich oder sinngemäß aus veröffentlichten oder unveröffentlichten Schriften entnommen wurden, habe ich als solche kenntlich gemacht. Ich erkläre außerdem, dass dies der erste Versuch ist, eine Dissertation einzureichen. Ich habe keine gleichartige Doktorprüfung an einer anderen Hochschule nicht bestanden.

Bayreuth

Lei Han